Spring 2017

# Conformational Studies of a Domain of the Influenza A M2 Protein Involved in Viral Budding and Morphology

Alice L. Herneisen , '17

# Conformational Studies of a Domain of the Influenza A M2 Protein Involved in Viral Budding and Morphology

Presented as a Senior Honors Thesis in Chemistry

**Alice Lydia Herneisen**

Department of Chemistry and Biochemistry

Swarthmore College

17 May 2017

**Advisor: Kathleen P. Howard, PhD**

# Forward

In my two years working in the Howard lab, I have cycled through a number of projects. These projects fall under the broad context of studying of how the cytoplasmic tail of a particular membrane protein of the influenza A virus, the Matrix protein 2 (M2), is involved in viral budding. I have chosen to present each project in the form of an independent manuscript, with separate Introduction, Experimental, Results, and Discussion sections. Some broader background and theory is briefly provided in Chapters 1 and 2, but Chapters 3-5 are designed to be largely self-contained. Potential future directions pertaining to all three projects are collected in Chapter 6.

Science is a collaborative enterprise, and this thesis has benefited from intellectual and experimental contributions from a number of talented collaborators. For the chapters where data is presented (Chapters 3-5), an explanation of the contributions of others is described in a statement at the end of the chapter.

# Table of Contents

# List of Figures and Tables

# Chapter 1: The Influenza A Virus and M2 Protein

### The Flu: A Major Public Health Concern.

"Influence of the stars", the Italians called the illness, until shifting scientific thought in the mid-fourteenth century amended its name to *influenza del freddo,* "influence of the cold". By the time English medical scholars adopted the word *Influenza* in the eighteenth century, the virus had demonstrated its powerful influence over human history via several pandemics.[1]

The influenza A virus is a persistent source of morbidity and mortality worldwide. The 1918 "Spanish Flu" killed an estimated 50 million people, exceeding the number of casualties during the coincident First World War.[1] While medical advances have given rise to effective but narrow-range influenza vaccines, the highly mutable viral genome and resultant antigenic drift necessitate seasonal pharmaceutical reformulation, placing considerable strain on the vaccine manufacturing process.[2] Furthermore, vaccines and antiviral drugs are often powerless against emergent, highly virulent pandemic strains, such as the 2009 H1N1 "swine flu", which sickened over 22 million Americans alone.[3] Developing a broadly protective or universal anti-influenza drug is a global health priority and serves as the motivation of our research.

### Influenza A Virus Ultrastructure and Replication Cycle.

The enveloped influenza virion harbors eight negative-sense RNA segments that encode four major structural proteins (HA, NA, M1, and M2) and several non-structural proteins involved in replication. Structural modules of the influenza virion consist of *1)* an external lipid envelope containing the spike glycoproteins hemagglutinin (HA),

neuraminidase (NA), and the ion channel protein M2 and *2)* a core of packaged ribonucleoproteins (RNP). These modules are linked through interactions with the envelope protein cytoplasmic tails and an internal peripheral matrix layer consisting of the M1 protein.[4] The HA and NA proteins are the major antigenic determinants of the influenza virus subtypes and serve as the basis for seasonal vaccines. The matrix proteins M1 and M2 exhibit a higher degree of sequence conservation and are therefore targets for drug development.[2]

The influenza virus life cycle consists of entry, uncoating, replication, assembly, and budding stages.[5] Viral entry follows HA-mediated endocytosis of the envelope. Uncoating occurs as the low-pH environment of the endosome activates the M2 ion channel function, which triggers acidification of the virus interior and causes dissociation of M1 and RNP. The liberated RNPs enter the nucleus to direct the replication of new virus particles. The newly synthesized viral envelope proteins are trafficked through the Golgi apparatus to reach the plasma membrane,[5] where they assemble in or around lipid raft domains enriched in cholesterol and sphingomyelin at the apical side of epithelial cells.[6,7] In current models,[8–10] HA, NA, and M1 remodel the membrane to initiate budding. The M2 protein clusters around the budding virus neck and completes scission (Figure 1.1).[11,12]

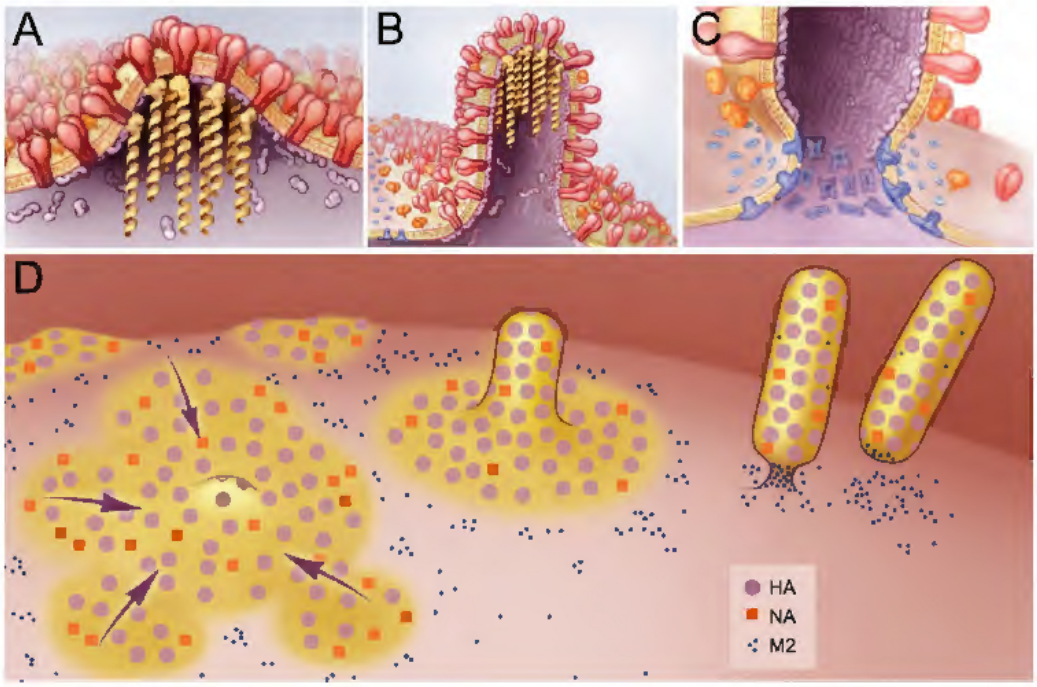


**Figure 1.1. A model for influenza virus budding.**
(A) HA (red) and NA (orange) cluster in the vicinity of lipid raft domains, where they interact with M1 protein (purple) to dock vRNP (yellow). (B) Polymerization of the M1 protein elongates the budding virus. (C) M2 protein clusters at viral neck, where it causes scission. (D) Influenza virus budding requires the coalescence of lipid rafts, mediated by HA and NA. Polymerization of M1 on the other side of the membrane (not shown) elongates the budding virus, and clustering of the M2 protein results in scission and egress. From [10].

### The M2 Protein: Multiple Functions, Many Conformations.

M2 is a multifunctional protein that plays essential roles in viral entry, assembly, and release[13], and is the focus of this work. The functional plasticity of the M2 protein is encoded within 97 amino acids that comprise an extracellular N-terminal domain (residues 1-24), a transmembrane domain (25-46), and a long cytoplasmic domain (47-97). Upon association with a membrane, M2 assembles into a homotetramer capable of conducting protons throngh a single-pore channel.[14]

Research on the M2 protein has historically centered on its ion channel function. Because the proton conductance mechanism is encoded within the transmembrane

domain[15], the majority of structural studies have utilized truncated constructs consisting of only the transmembrane helices (M2TM, residues ~22-46) or the transmembrane helices and a short C-terminal extension (M2TMC, residues ~22-60). Adamantane drugs were found to be potent inhibitors of ion channel activity[14]; however, following the widespread development of resistance to these drugs[16], investigation shifted to expanding the structural understanding of the cytoplasmic tail of the protein. Our group and others have demonstrated that residues 50-60 form a membrane-proximal amphipathic helix.[17–19] We have found that the conformation of the amphipathic helices are sensitive to pH[17], the composition of the membrane[20], and presence of adamantane drugs.[21]

For the past few years, our research has been motivated by the need to improve our understanding of how the M2 cytoplasmic tail is involved in viral budding. Background information for three projects investigated under this broader work is summarized below. Data from these three projects is presented in Chapters 3-5.

**M2 as a Shape-Shifter: Membrane Sensing and Membrane Remodeling.**

Biophysical investigations of the M2 protein in several different membrane environments have lead to the conclusion that the M2 protein functions as a "shape shifter" that is highly sensitive to the hydrophobic environment of the membrane (Figure 1.2).[20,22,23] Previous work from our group has measured the proximity of the M2 transmembrane and amphipathic helices to infer the helix tilt with respect to the membrane normal. In one study, increasing bilayer thickness from 19.5 Å to 27 Å caused the M2 transmembrane helices to decrease their tilt (Figure 1.2A).[22] This observation was attributed to hydrophobic matching of the helix tilt and the membrane thickness. One

intriguing finding from this work was the difference between M2 behavior in DOPC (1,2-dioleoyl-sn-glycero-3-phosphocholine) and POPC (1-palmitoyl-2-oleoyl-sn-glycero-3-phosphocholine) membranes (Figure 1.3): despite the similar hydrophobic thickness of these two lipids (27 and 26.5 Å, respectively), the M2 protein only reached the "limiting conformation" with minimal helical tilt in POPC membranes.[22] Due to this unexplained effect, later studies of the M2 protein used POPC bilayers.[17,18,21]

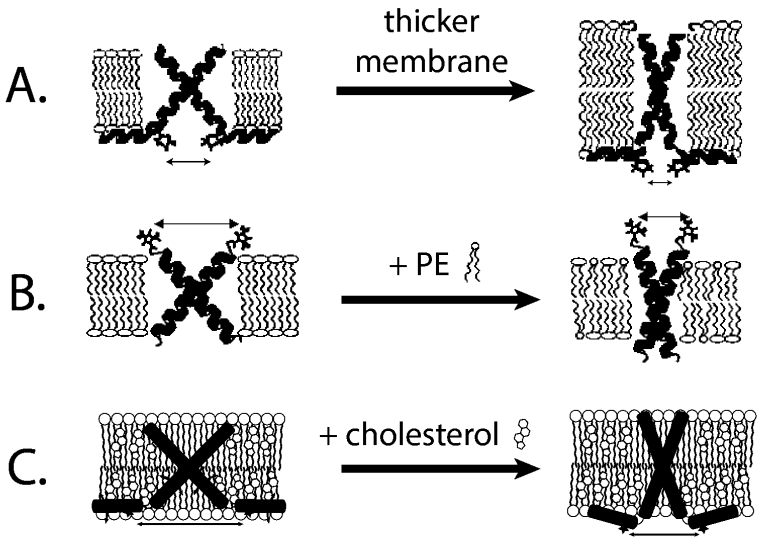


**Figure 1.2. The M2 protein is sensitive to membrane thickness, lateral pressure, and cholesterol content.**
(A) The M2 helices tilt to match their length to the thickness of the bilayer.[22,23] (B) Increasing the lateral pressure of the membrane by adding PE lipids results in a tilt of the transmembrane helices.[23] (C) The presence of cholesterol in the membrane stabilizes an M2 conformation with tighter packing of the amphipathic helices.[20] Arrows denote the relative distance between spin labels (Chapter 2).

Additional investigations revealed that the M2 "limiting conformation" was coupled to the lateral pressure profile of the membrane environment. Adding phosphoethanolamine (PE) lipids to the membrane pushed the M2 transmembrane helices towards the conformation with a smaller helix tilt (Figure 1.2B). Phosphatidylcholine

(PC) lipids consist of a zwitterionic head group of a similar size to the acyl tails (Figure 1.3); such lipids are characterized as "cylindrical" and have little intrinsic curvature. In contrast, PE lipids consist of a small amine head group linked to bulky acyl tails, producing a "cone" shape with high intrinsic curvature (Figure 1.3).[24] As a result of their conical shape, PE lipids increase the lateral pressure profile of the acyl chain region and cause a decrease in the lateral pressure profile in the head group region.[25]

Because DOPC membranes required the addition of PE lipids to achieve the same limiting conformation observed in the absence of PE in POPC membranes, it was reasoned that DOPC membranes lack the lateral pressure profile to support the minimal tilt of the transmembrane helices.[23] The effects of DOPC and DOPE lipids on the conformational properties of the M2 protein are revisited in the context of intrinsic membrane curvature rather than lateral pressure in Chapter 5.

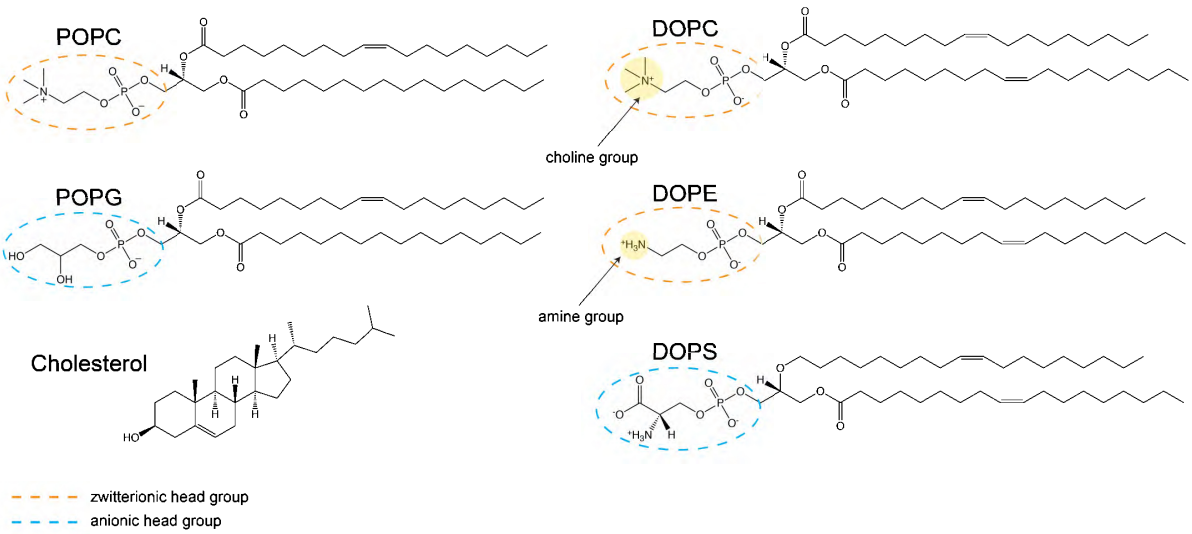


**Figure 1.3. Structures of the lipids used to study the conformational properties of the M2 protein.**
1-palmitoyl-2-oleyl-*sn*-glycero-phosphocholine (POPC) and 1-palmitoyl-2-oleyl-*sn*-glycero-3-[phospho-*rac*-(1-glycerol)] (POPG) have a saturated (C16:0) and an unsaturated (C18:1) acyl chain. 1,2-dioleoyl-sn-glycero-3-phosphocholine (DOPC), 1,2-dioleoyl-sn-glycero-3-phosphoethanolamine (DOPE), and 1,2-dioleoyl-sn-glycero-3-phospho-L-serine (DOPS) have two unsaturated (C18:1) acyl chains.

### Is M2 a Cholesterol-Binding Protein?

The influenza virus buds from cholesterol- and sphingomyelin-enriched lipid rafts domains termed the "budozone".[4] *Rossman et al*. demonstrated that the M2 protein alone can bud from membrane mimetic systems in a cholesterol-dependent manner.[11] Since then, elucidating the possible interactions between M2 and cholesterol has been an area of intense interest. *In vivo* studies provide evidence that M2 may directly bind cholesterol and undergo cholesterol-dependent scission. M2 extracted from virus-infected cells coimmunoprecipitates with a significant amount of cholesterol.[12] Furthermore, when cholesterol was excised from the membrane with methyl-β-cyclodextrin, viral filament formation was abolished.[12] Similarly, M2-dependent cytotoxicity is lost in cholesterol-free insect cell lines.[26] While these studies provide evidence for the cholesterol-dependent function of M2, *in vivo* investigations of the interplay between cholesterol and M2 can be highly dependent on the expression system used.[27,28]

*In vitro* studies have also proved inconclusive. On one hand, purified full-length M2 and a truncation consisting of just the cytoplasmic tail directly associated with cholesterol[27,29]. Our own group has demonstrated that the addition of cholesterol to the membrane favors the limiting conformation of M2 discussed earlier (Figure 1.2C).[20] However, thermodynamic and structural studies of possible M2-cholesterol interactions face challenges distinguishing between conformational change due to direct protein-cholesterol binding or conformational change due to cholesterol-dependent alterations to membrane properties.[20,30] It has been demonstrated that the addition of cholesterol to the membrane shifts the monomer-tetramer equilibrium of M2TMC constructs towards the tetramer species, but not in a way that implicates stoichiometric cholesterol binding.[31] A

recent solid state NMR study identified strong crosspeaks between $^{3}C$ Phe-labeled M2FL and $^{13}C_{2,3,4}$-labeled cholesterol, suggesting that F47, F48, F54, or F55 may be in close proximity to cholesterol in the membrane.[32] Attempts to characterize cholesterol-dependent structural change in the M2 protein are still ongoing[20,30,32–34] and are the topic of Chapter 4.

### The Distal Cytoplasmic Tail: the "Wild West" of the M2 Protein.

While the transmembrane and membrane-proximal amphipathic helix domains of M2 have been structurally characterized in detail, relatively little is known about the structure of the remaining residues of the cytoplasmic tail, although virological methods have identified their functional significance. Scanning alanine mutagenesis, in which a series of amino acids are mutated to alanine in order to alter the unique properties of residues while preserving overall secondary structure, has revealed that mutating cytoplasmic tail residues 70-77 results in ineffective viral genome packaging.[35–38] It remains an open question if M2 facilitates genome packaging via a direct viral ribonucleoproteins (vRNP) binding domain, or indirectly, by binding to an M1-vRNP complex.

The M2 cytoplasmic tail interacts with the M1 protein, perhaps through several mechanisms. Truncations of the M2 protein at residue 70 co-precipitate with M1, indicating that an M1-binding site exists before this residue.[36,37] Initial findings suggested that an M2 fragment consisting of cytoplasmic tail residues 70-97 alone did not pull down M1[36]; however, a co-immunoprecipitation assay of full-length M2 with triplet alanine substitutions demonstrated that mutations at residues 71-76 result in decreased

M1 incorporation.[37] Taken together, these findings suggest that cytoplasmic tail residues 45-69 harbor a general M1 binding site, while residues 71-76 may interact with specific M1-vRNP complexes that represent a smaller proportion of the overall M1 population.

As a part of Chapter 3, we investigate the dynamic properties of the cytoplasmic tail residues 50-70 and characterize their topology with respect to the membrane. A significant amount of the preparation for this thesis was spent attempting to set up a system for the study of M2 residues 71-80. That work, ultimately, was set aside and is presented as a part of the Future Directions in Chapter 6.

### The Scission-Defective PentaAla Mutant.

The pentaAla mutant consists of five mutations to one face of the M2 amphipathic helix: F47A, F48A, I51A, Y52A, and F55A. This mutant was originally studied in the context of its ion channel activity. The pentaAla mutant does not exhibit impaired proton conductance[15], a finding that has since been replicated[39,40], and was initially used as evidence that the amphiphilic helices are expendable for ion channel function.[15]

Ironically, the same mutant was used to demonstrate that the M2 amphipathic helices are necessary for viral budding. The same *in vitro* budding assay that demonstrated cholesterol-dependent scission activity in the M2 protein also revealed that the pentaAla mutant was scission-defective.[11]

Virological and cell biology studies have replicated these pentaAla deficiencies *in vivo*, and the major findings are summarized as follows: Cells infected with a recombinant influenza virus expressing the pentaAla M2 mutant exhibited severely impaired viral filament formation.[12] This phenotype resembled the phenotype of cells

infected with viruses that expressed no M2. The ability of pentaAla M2 to localize to viral buds was not impaired by the alanine substitutions[12], although this finding was later challenged.[40] PentaAla protein isolated from virus-infected cells co-precipitated with significantly lower amounts of cholesterol than the wild type protein.[12] PentaAla viruses exhibit reduced plaque-forming kinetics and a scission-defective "beads-on-a-string" morphology[40], although different studies disagree about the infectivity of pentaAla viruses once released.[39,40] Follow-up studies demonstrated that mutations to any two of the five hydrophobic amino acids selected for substitution in the original pentaAla mutant are sufficient to disrupt viral filament formation and greatly attenuate growth kinetics.[40]

To our knowledge, only two biophysical studies of the pentaAla mutant have been published. The earlier study used a small-angle X-ray scattering (SAXS) to demonstrate that the pentaAla mutant has attenuated ability to generate the type of curvature necessary for scission at the neck of a budding virus over the range of lipid compositions and concentrations studied.[41] The second recent study investigated the ability of short peptides with the sequence of the M2 or pentaAla amphipathic helices to insert intro the membrane and showed that the pentaAla helix inserts less deeply into the membrane than M2 amphipathic helix peptide.[42] This same study also identified the maximum membrane-interacting side chains in the wild-type protein to be I51 and F55, followed by F47, F48, and Y52, thereby rationalizing why mutations to these residues significantly perturb the insertion depth of the helix.[42]

As a part of Chapters 4 and 5, we seek a structural understanding of this mutant protein with the goal of understanding how the wild-type protein functions. The reported loss of function in the pentaAla construct may result from a disruption in the local

secondary structure, changes in packing within the homotetramer, alteration of amphipathic helix topology with respect to the membrane, or impaired ability to interact with cholesterol. We attempt to distinguish between these possibilities using site-directed spin-labeling electron paramagnetic resonance spectroscopy (SDSL-EPR).

# Chapter 2: Site-Directed Electron Paramagnetic Resonance Spectroscopy

## INTRODUCTION

This chapter provides a brief overview of the fundamentals of electron paramagnetic resonance (EPR) spectroscopy, with special attention to the biomolecular applications of site-directed spin labeling (SDSL). The theory of the method is presented first and is followed by a synopsis of SDSL-EPR techniques used in later chapters. For a more comprehensive overview of SDSL-EPR techniques beyond those covered in this thesis, the reader is directed to several excellent classic and recent reviews.[43–48]

Site-directed spin labeling EPR is a powerful method for studying membrane proteins in native-like membrane environments, both of which are refractory to other well-established methods such as NMR and X-ray crystallography. The approach requires attachment of stable radical to a unique side chain, typically cysteine. These studies employ (1-Oxyl-2,2,5,5-tetramethyl-Δ3-pyrroline-3-methyl) Methanethiosulfonate (MTSL), a commonly used nitroxide spin label that forms a disulfide linkage to an existing cysteine residue (Figure 2.1). The resulting side chain is commonly referred to as "R1".[43,44]

The power of SDSL-EPR arises from the exquisite sensitivity of the R1 side chain to the surrounding microenvironment, as described below.

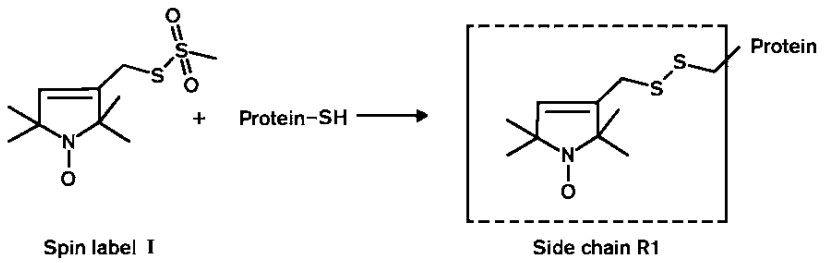


**Figure 2.1. The structure of the MTSL probe and R1 side chain.**
The spin label attaches to a rednced cysteine side chain via a disnlfide linkage, forming the R1 side chain. From [45].

## THEORY: THE BASIS OF THE NITROXIDE LINE SHAPE

### Origin of the Signal: The Zeeman Effect.

A spinning charge snch as an electron possesses a magnetic dipole moment, $\mu$, as well as an intrinsic spin angular momentum. For an electron, the spin angular momentum (often referred to simply as 'spin') is characterized by the quantum number $m_s = \pm ½$.[49] In the presence of an external magnetic field, the degeneracy of non-zero spin states is lifted, resulting in a phenomenon known as the *Zeeman effect* (Figure 2.2). The difference between the Zeeman energy levels is proportional to the strength of the magnetic field:[50]

$$\Delta E = g_e \mu_B H_0 \qquad (1)$$

where $g_e$ is the electron g-factor, which is approximately 2 for a free electron, $\mu_B$ is the Bohr magneton, and $H_0$ is the strength of the magnetic field. When the frequency of external electromagnetic radiation matches the energy separation of the two electron spin states, a transition between spin states occurs (known as *resonance*), and an absorbance peak is detected:[50]

$$\Delta E = h\nu = g_e \mu_B H_0 \qquad (2)$$

In the tradition of continuous wave (CW) EPR, a fixed radiofrequency is applied to the paramagnetic sample while the magnetic field is swept to detect resonance.[50] The magnetic field is modulated to enhance signal-to-noise. The amplitude of the EPR signal is sensitive to the modulation frequency, and the resulting output of the phase-sensitive detector is the slope op the absorption curve, i.e. the first derivative.[43]

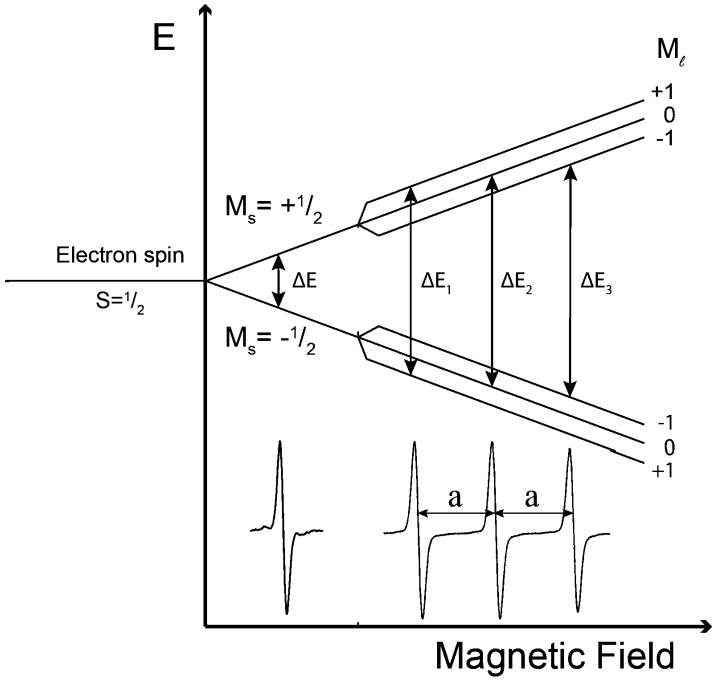


**Figure 2.2. Transitions between electron spin states give rise to resonance.**
In the presence of an external magnetic field, the degeneracy of the spin states of an unpaired electron is lifted, resulting in Zeeman splitting. Interactions between the unpaired electron and surrounding nuclei with non-zero nuclear spin angular momenta give rise to the hyperfine splitting. Resonance is detected when the energy of the applied electromagnetic field matches the energy separation of the spin states.

### Multi-Line Spectra: The Nuclear Hyperfine Interaction.

While the Zeeman effect is the predominant source of the spin energy level splitting, interactions with surrounding nuclei with non-zero nuclear spin angular momenta produce additional splittings and, consequently, additional absorbance peaks. This effect is known as the *hyperfine interaction*. Each nucleus *N* with spin angular momentum *I* splits the electron spin energy levels into (*2NI+1*) sublevels corresponding to the nuclear angular momentum numbers $m_I$.[49] For nitroxide spin labels, one $^{14}N$ nucleus (N=1) with intrinsic $I = 1$ splits the electron spin energy levels into three sublevels[43], $m_I =$

$-1, 0, +1$ (Figure 2.2). Transitions between the energy levels are dictated by the quantum mechanical selection rules $\Delta S = 1$ and $\Delta M_L = 0$.[49] The resulting transitions are separated by the hyperfine coupling constant $a$, which is sensitive to the polarity of the surrounding chemical environment.[43]

## BIOMOLECULAR APPLICATIONS: METHODS IN SITE-DIRECTED SPIN LABELING EPR SPECTROSCOPY

The information obtained from SDSL-EPR provides valuable insight into the motional properties of the spin label, the accessibility of the spin label probe to surrounding paramagnetic reagents, and distances between multiple spin labels.[43] The remainder of this chapter will focus on the first two pieces of information. Determining the distance between multiple spin labels, even qualitatively, presents unique challenges for the cell-expressed, full-length M2 protein, and so this approach was not pursued as a part of this thesis. The interested reader is directed to earlier work out of the Howard lab for previous experimental work with EPR-derived distances.[17,20–23]

### The EPR Line Shape Reveals Motional Properties of the Side Chain.

Mobility information is readily obtained from the CW EPR line shape. X-band EPR spectroscopy detects rotational motion in the range of 0.1 to 100 nsec.[43] Three main types of motions contribute to the nitroxide rotational correlation time ($\tau$): the protein rotational diffusion (i.e. tumbling), backbone fluctuations, and internal motions of the side chain.[44] Under our sample conditions, the proteoliposome tumbling rate is too slow to significantly affect the EPR line shape. The rotational correlation time of the R1 side chain predominantly reflects side chain internal motion.[44]

The internal motion of R1 can report on backbone dynamics, secondary and tertiary structure, and conformational equilibria.[44] Although the R1 side chain is attached to the protein backbone by five rotatable bonds, for most sites rotation is restricted to the X4 and X5 dihedrals due to the presence of an intra-residue hydrogen bond between the side chain H-Cα and Sδ (Figure 2.3A). Rotations around the X4 and X5 bonds produce an anisotropic, averaged motion of the nitroxide p-orbital that is modeled as a cone (Figure 2.3B). The angle of the opening of the cone defines the order parameter and corresponding correlation time. Higher order parameters and correlation times correspond to more anisotropic motion, and often lower mobility. Interactions of the R1 side chain with local protein structure may increase the order parameter and correlation time (e.g. due to rapid backbone fluctuations) or decrease the order parameter and correlation time (e.g. due to the presence of tertiary structure).[44]

While simulating the order parameter and correlation time of the spin label provides insight into side chain internal motion, often the mobility of the label can be immediately inferred from the spectral line shape (Figure 2.3C).[43] At the fast motional limit, a spin label spectrum consists of three sharp peaks of equal height. Attaching the spin label to a peptide results in motional restriction that depends on the position of the spin label within the biological molecule. For example, spin label located within secondary structural element experiences a greater degree of motional restriction than a spin label attached to a solvent-exposed, unstructured protein segment. At the other end of the spectrum, a "rigid-limit" or frozen spectrum may be produced when a spin label is tightly packed within the core of a protein.[43]

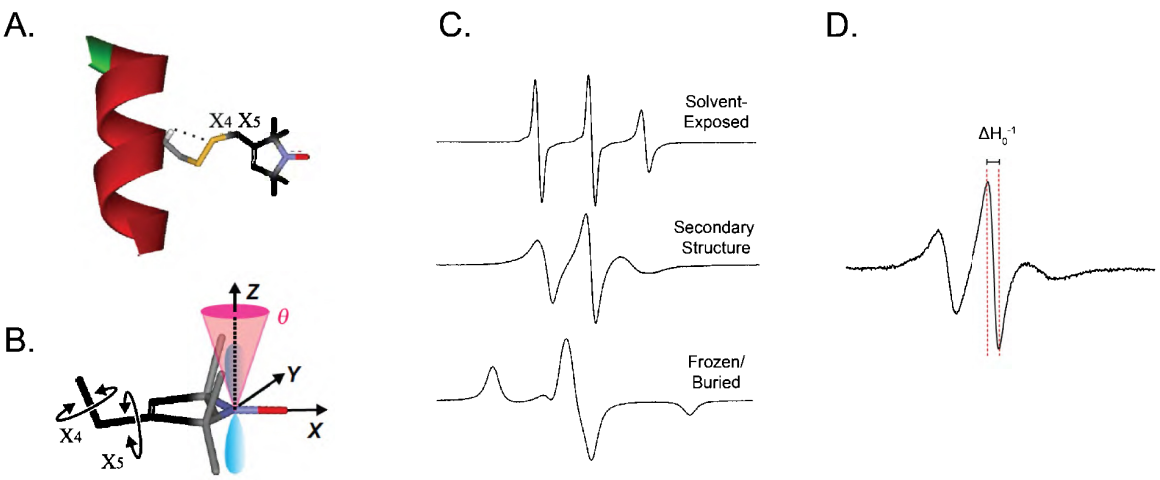


**Figure 2.3. The EPR spectrum of R1 is sensitive to local protein dynamics.** (A) R1 rotameric flexibility reflects primarily internal motions around the X4 and X5 dihedrals due to an intra-residue hydrogen bond between the Sδ and H-Cα atoms. From [44]. (B) The nitroxide orbital undergoes motion in a cone. From [44]. (C) The degree of internal motion of the R1 side chain reflects the surrounding protein environment. Spectra are shown in order of increasing correlation time. (D) The semi-empirical relative mobility factor is the inverse peak-to-peak width of the central line ($\Delta H_0^{-1}$).

A simple, semi-empirical relative mobility factor can be calculated from the inverse peak-to-peak width of the central line ($\Delta H_0^{-1}$) of the EPR line shapes (Figure 2.3D).[43,44] A smaller central line width corresponds to a higher relative mobility factor. The work done here relies on using $\Delta H_0^{-1}$ to characterize side chain mobility. However, some caution is required in interpreting the relative mobility factor. For spectra with a two-component nature, discussed further below, the central line width will be dominated by the fast motional component.[51,52]

### Multicomponent Line Shapes Arise when R1 Experiences Multiple Environments.

In some instances, an R1 side chain may give rise to a complex spectrum with multiple resolvable components. Such multicomponent spectra arise from populations of

the spin labels with different motional states. The corresponding spectral components are often classified as "mobile" or "immobile". It is important to note, however, than the X-band EPR used here lacks the spectral resolution to resolve distinct components in the slow-motional, "immobile" regime.[44]

A two-component spectrum can arise from A) two rotameric states of the R1 side chain or B) an equilibrium between two protein conformational states with distinct local environments surrounding the R1 side chain (Figure 2.4).[44] It is important to distinguish between these possibilities before interpreting two-component spectra in terms of conformational exchange. In practice, methods such as osmolyte perturbation[53] and saturation recovery EPR[47] can be used to identify if the two-component spectrum originates from an equilibrium between distinct conformational states. Previous work out of the Howard lab has demonstrated that two-component spectra in the C-terminal amphipathic helices of M2 arise from a conformational equilibrium rather than spin label rotamers.[20]

Once it has been established that a complex line shape arises from multiple conformational states, the separate components can be isolated via spectral simulation.[52] While Chapter 5 benefits from fit parameters extracted from simulations of multicomponent CW spectra, spectral simulation is not the focus of this work. The interested reader is directed instead to the thesis of D. Stuart Arbuckle '17.[54]

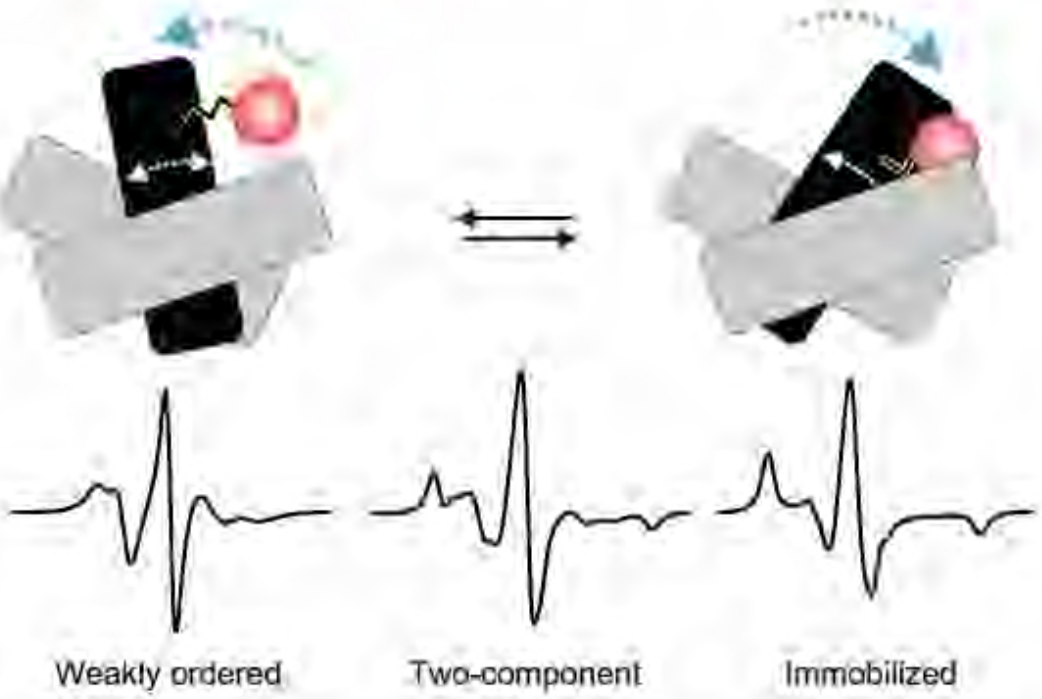


**Figure 2.4. Conformational exchange can give rise to a multicomponent CW EPR spectrum.**
The spin label is attached to a region of the protein (black helix) that exists in conformational equilibrium between two different states. The mobility of the spin label differs in the two states, giving rise to a two component spectrum that is a weighted sum of the two motional components. From [44]

**Power Saturation EPR Provides Information About R1 Side Chain Accessibility.**

Power saturation EPR provides valuable insight into the accessibility of a spin label to a paramagnetic reagent. Paramagnetic reagents increase the relaxation rate of the spin label. Under nonsaturating conditions, the EPR signal intensity is proportional to square root of the incident power, $P^{1/2}$. At sufficiently high power, the rate of electron excitation equals the rate of relaxation, such that the number of *net* transitions from the lower energy to the higher energy spin state declines. Under these conditions, the EPR signal becomes saturated, and the intensity of the central peak decreases.[43]

Paramagnetic reagents can interact with the spin label to enhance the relaxation rate, with the consequence that the signal requires a higher power level to reach saturation. The utility of the power saturation method comes from the fact that two commonly used paramagnetic relaxation agents, oxygen and nickel (II) ethylenediaminediacetate (NiEDDA) partition into different environments. Oxygen is a small hydrophobic species that localizes to the interior of the membrane and hydrophobic pockets of proteins, whereas NiEDDA is water-soluble and localizes to the solution phase.[43] NiEDDA is not commercially available and typically is synthesized in-house (Appendix A). This thesis uses the additional paramagnetic reagent 1,2-dioleoyl-sn-glycero-3-[(N-(5-amino-1-carboxypentyl)iminodiacetic acid)succinyl] nickel salt (DOGS-NTA[Ni(II]), which consists of Ni(II) chelated to a lipid. This Ni-chelate lipid has been used to measure the accessibility of protein side chains to the membrane-aqueous interface.[55]

Power saturation experiments are performed in the presence of diamagnetic nitrogen gas in order to determine the intrinsic relaxation rate of the spin label. The intensity of the center line is measured in a series of microwave powers and is fit to the following equation[43]:

$$A = I \cdot P^{\frac{1}{2}} \left[ \frac{1 + \left(2^{\frac{1}{\varepsilon}} - 1\right) P}{P_{1/2}} \right]^{-\varepsilon} \tag{3}$$

where A is the intensity, or amplitude of the central peak, I is a scaling factor, P is the incident power, and ε is a measure line homogeneity that is varied between 0.5 and 1.5.[17] The power saturation parameter, $P_{1/2}$, is the power at which the signal intensity is half of the unsaturated intensity.[43]

The power saturation experiment is repeated in the presence of a paramagnetic relaxation agent, e.g. oxygen or NiEDDA (Figure 2.5A), and the "baseline" $P_{1/2}$ of the spin label in the presence of nitrogen is subtracted in order to calculate the increase in relaxation caused by the paramagnetic reagent $(R_x)$[43]:

$$\Delta P_{\frac{1}{2}}(R_x) = P_{\frac{1}{2}}(R_x) - P_{\frac{1}{2}}(N_2) \tag{4}$$

The $\Delta P_{1/2}$ value can provide site-specific information about the proximity of a spin label to a particular relaxation agent. This value can be normalized using a standard sample of diphenylpicrylhydrazyl (DPPH) to provide a universal accessibility parameter, Π.[43] For the purposes of this thesis, the relative $\Delta P_{1/2}$ value suffices.

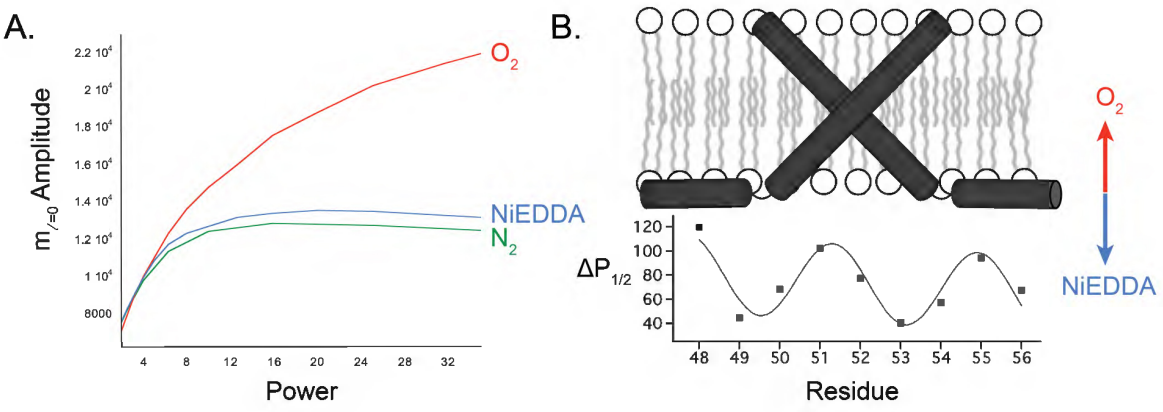


**Figure 2.6. Spin label accessibility profiles as a blueprint for protein topology.** (A) Power saturation curves of an R1 side chain in the presence of the indicated paramagnetic relaxation agents. NiEDDA is water soluble, whereas $O_2$ partitions into the bilayer. This particular R1 is in a hydrophobic environment, as the label exhibits higher accessibility to oxygen than to NiEDDA. (B) Trends in accessibility profiles reveal features of protein topology with respect to the membrane. The accessibility of spin labels at M2 sites 48-56 to oxygen and NiEDDA vary sinusoidally, indicating that this region forms a juxtamembrane amphipathic helix.

Accessibility information is especially informative for membrane proteins. Oxygen exists as a gradient within the membrane, and therefore oxygen accessibility tracks well with membrane depth. Trends in spin label oxygen and NiEDDA accessibility should be complementary and self-consistent, e.g. a membrane-buried site is expected to have a high oxygen accessibility and low NiEDDA accessibility.[43] Accessibility information provides immediate insight into whether specific site is solvent- or membrane-exposed. Alternatively, the accessibility profiles of a series of consecutive labeled sites can be determined in order to produce a topological map of a region with respect to a hydrophobic environment, e.g. the membrane. Both approaches were used in the context of this thesis.

# Chapter 3: Structural Features of the C-Terminal Domain of the Full-Length M2 Protein in Lipid Bilayers

## INTRODUCTION

The influenza A M2 protein is a 97-amino acid, homotetrameric membrane protein that plays critical roles during viral uncoating[14] and budding.[10] The structural properties of the M2 protein have been heavily studied in the context of its ion channel activity, which is mediated by the transmembrane domain.[14] Adamantine drugs were found to be potent inhibitors of proton conductance[3]; however, due to widespread resistance to these drugs[56], investigation has shifted to elucidating the structure and dynamics of the relatively uncharacterized M2 cytoplasmic tail.[57]

Deletion and mutagenesis studies identified the role of the C-terminal cytoplasmic tail in mediating influenza virus infectivity and morphology.[35–38,40,58–60] Despite the functional importance of this domain, the majority of biophysical studies of the M2 protein have utilized chemically synthesized, truncated constructs consisting of the transmembrane domain (M2TM, residues ~22-46) or the transmembrane domain with a short C-terminal extension (M2TMC, residues ~22-62). These studies have revealed that M2 exhibits remarkable structural plasticity in response to the membrane environment.[20,22,23,61] Identifying the membrane mimetic and protein:lipid ratio most physiologically relevant for the protein's separate ion channel and scission functions has been a source of considerable debate.[33,61]

In this study, we focus on elucidating the structure and dynamics of the full-length M2 protein between residues 50-70. We use site-directed spin-labeling electron

paramagnetic resonance spectroscopy (SDSL-EPR), a technique exquisitely suited to detecting the dynamics of membrane proteins reconstituted into physiologically relevant bilayers. This approach provides us with site-specific information about this region's mobility and topology with respect to anionic, cholesterol-depleted lipid membranes that have been used in previous functional[11] and biophysical studies performed by our group[17,18,20,21,23] and others.[34,62] Our findings indicate the cytoplasmic domain consists of a membrane-proximal α-helix followed by a highly dynamic region with no stable secondary structure under our environmental conditions. We hypothesize that the dynamic properties of this region may be functionally important for regulating viral assembly and budding.

## MATERIALS AND METHODS

### Mutagenesis, Expression, Spin Labeling, and Purification of M2 Protein Constructs.

Single cysteine substitutions were introduced into sites 61-70 of the A/Udorn/M2 SGC plasmid[63] containing the mutations W15F, C17S, C19S, and C50S and a C-terminal $His_6$-tag using a PCR-based QuikChange Lightning Site-Directed Mutagenesis Kit according to the manufacturer's protocol (Agilent Technologies, Santa Clara, CA). All plasmids were verified using fluorescence-based automated sequencing services (Genewiz Inc., South Plainfield, NJ). Recombinant plasmids were transformed into BL21 *E. coli* cells and expressed according to published protocols.[18,63]

For each cysteine construct, a cell pellet from ¼ L of growth was resuspended in 9.5 mL lysis buffer (50 mM Tris pH 8, 40 mM octyl β-D-glucopyranoside (OG), 150 mM NaCl, 0.2 mg/mL DNase I, 0.25 mg/mL lysozyme, and 50 mM AEBSF). The resuspended pellet was then sonicated on ice at 20% amplitude, 20 minutes 1 sec on / 1

sec off. The lysate was centrifuged at 16,000 rpm for 30 minutes at 4°C. The clarified supernatant was incubated with 0.5 mL Ni-IDA resin (GoldBio), 20 mM imidazole, and 7 mM β-mercaptoethanol for 30 minutes with nutation. The column was washed successively with 10 column-volumes of Wash I (50 mM Tris pH 8, 150 mM NaCl, 40 mM OG, 20% v/v glycerol), Wash II (50 mM Tris pH 8, 20 mM OG, 20% v/v glycerol), and Wash III (50 mM Tris pH 8, 4 mM OG, 20% v/v glycerol, 20 mM imidazole). Tenfold molar excess of (1-Oxyl-2,2,5,5-tetramethyl-Δ3-pyrroline-3-methyl) methanethiosulfonate (MTSL) spin label was dissolved in 16 $\mu$L acetonitrile and diluted in 1 mL Wash III. The MTSL solution was applied to the column and was incubated for 24-48 hours at room temperature with nutation. The MTSL solution was allowed to elute, and the column was nutated for 20 minutes with Column Labeling Buffer (50 mM Tris pH 8, 4 mM OG, 20% v/v glycerol) to facilitate the removal of free spin label. The column was washed an additional 20 column-volumes of Column Labeling Buffer, followed by elution of the protein with 10 column volumes of Elution Buffer (50 mM Tris, 300 mM imidazole, 4 mM OG, and 20% v/v glycerol buffer). The protein solution was buffer-swapped into 50 mM Tris pH 8, 4 mM OG buffer using PD-10 desalting columns (GE Healthcare, UK). The purity of protein was verified using Sodium dodecyl sulfate polyacrylamide gel electrophoresis (Figure S1.1).

**Reconstitution of the M2 Protein into Liposomes.**

Full-length M2 protein was reconstituted into 1-palmitoyl-2-oleoyl-sn-glycero-3-phosphocholine and1-palmitoyl-2-oleoyl-sn-glycero-3-phospho-1-rac-glycerol

(POPC:POPG) 4:1 bilayers at a 1:500 protein to lipid ratio. This membrane system has been used in published structural[17,18,20,21,23,34,62] and functional[11] studies of the M2 protein. The reconstitution protocol has been described previously and is described in detail in the *SI Materials and Methods* in Chapter S1. The buffer used for sample collection was 50 mM Tris pH 7.8, 100 mM KCl, and 1 mM EDTA.

Lipid films used for NiEDDA accessibility studies were prepared according to the same reconstitution protocol but were rehydrated in 50 mM NiEDDA, 50 mM Tris pH 7.8, and 100 mM KCl buffer. NiEDDA synthesis is described further in Appendix A. The nickel-chelated lipid used in accessibility studies was 1,2-dioleoyl-sn-glycero-3-[(N-(5-amino-1-carboxypentyl)iminodiacetic acid)succinyl] nickel salt (DOGS-NTA[Ni(II]). Accessibility studies were carried out on proteins reconstituted into bilayers with a molar ratio of 4:1:1.25 POPC:POPG:DOGS-NTA[Ni(II)].[21]

**EPR Spectroscopy and Data Analysis.**

CW EPR spectra were recorded on an X-band Bruker EMX spectrometer equipped with an ER4123S resonator at room temperature. Samples were placed in a gas-permeable TPX tube and CW EPR spectra were acquired using 2 mW incident microwave power, 1 G field modulation amplitude at 100 kHz, and 150 G sweep width.

Power saturation experiments were collected under four conditions: equilibrated with nitrogen gas, equilibrated with ambient air, equilibrated with nitrogen in the presence of NiEDDA, and equilibrated with nitrogen in the presence of DOGS-NTA[Ni(II)]. Nitrogen power saturation experiments were collected over eight power

levels. All other power saturation experiments were measured over 16 power levels. Data were fit to obtain $\Delta P_{1/2}$ parameters as described previously.[17]

## RESULTS

### Sequence Analysis of the Full-Length M2 Protein.

Each M2 monomer consists of an N-terminal ectodomain, a transmembrane domain, and a cytoplasmic domain (Figure 3.1A). Although the distal C-terminal domain of the M2 protein has been implicated in viral assembly[35–38,58], morphology[36,38,40,59], and budding[11,36,40,59], the region beyond the membrane-parallel amphipathic helix[17,18] has remained refractory to atomic-level studies.[34,62] Protein sequence analysis algorithms predict that residues 58-69 comprise a coil between two helical regions spanning residues 24-57 and 70-80 (Figure S1.2A).[64] However, even regions exhibiting a low propensity for ordered secondary structure in intrinsically disordered proteins have been known to adopt helical conformations when exposed to membrane environments.[65–67]Additional sequence analysis does not predict disorder for the M2 residues 58-70 beyond the confidence interval threshold (Figure S1.2B).[68] In order to elucidate the possible structure and dynamics of the distal cytoplasmic tail, we employed SDSL-EPR to scan sites 61-70 for mobility and accessibility information. Unique cysteine residues were introduced into a functional cysteine-less background[63] and were labeled with the sulfhydryl-specific MTSL spin probe.[43] Hereafter mention of specific sites in the protein refers to spin-labeled cysteine residues. Circular dichroism studies of the cysteineless protein and one representative spin-labeled construct were collected to ensure that the attachment of a spin label does not perturb the secondary structure of the amphipathic helix (Figure S1.3).

**Sites in the Amphipathic Helix and Flanking C-Terminal Region Exhibit Different Line Shapes.**

The spectral line shape of spin-labeled residues can provide insight into secondary and tertiary contacts, conformational dynamics, and relative mobility.[43] Stack plots of the CW-EPR spectra for sites 61-70 are shown in Figure 3.1B with previously published data[18] collected for sites 50-60, as well as site 43, which serves as a reference for a residue on the C-terminus of the transmembrane domain. The spectra shown in Figure 3.1B illustrate a diversity of structural dynamics. As a general trend, spin labels at positions 43 and 50-60 exhibit slightly broadened spectra, which may arise from partial motional restriction caused by tertiary contacts or the surrounding membrane environment.[43] In contrast, the spectra of spin labels at positions 62-70 consist of three sharp and narrowly spaced peaks, indicative of low motional restriction of the nitroxide spin label. Such line shapes are consistent with a lack of a stable secondary structure[67,69] and may arise from reduced contacts with the membrane.

A notable feature of this region of the protein is the presence of complex EPR spectra. All of the spectra in the 50-61 region appear to consist of at least two spectral components, highlighted in gray for the low-field resonance ($m_I = 1$), suggesting that the nitroxide spin labels at these positions occupy distinct microenvironments with differing motional states.[44] The darker gray box marks the immobile component (I), whereas the light gray box marks the mobile component (M). Two-component spectra may arise from different rotamers of the spin label or conformational exchange between different states of the M2 protein.[47] A combination of microscopic order macroscopic disorder (MOMD) modeling[48], saturation-recovery EPR[47], and pulsed EPR[46] methods have identified that the two-component spectra exhibited by sites in the amphipathic helix in truncated M2

constructs correspond to two distinct states undergoing conformational exchange[20], and we postulate that a similar conformational equilibrium exists for this region in the full-length protein.

Several of the spectra between positions 61-70 reveal a two-component nature, but the contribution from the immobile population does not appear to be as prominent as for sites 50-60. Some spectra, such as G62R1 and E70R1, appear to almost lack the two-component nature entirely. Because limited structural information exists for this region, we hesitate to attribute the complex EPR spectra exhibited by some spin label residues to distinct protein conformations. Saturation recovery EPR[47] is required to assess whether the fast and slow motional components observed for some sites corresponds to different rotamers of the MTSL label or two protein populations with different local environments. While the nature of the conformational equilibrium in this region is uncertain, the presence of two motional components may indicate that these residues are not uniformly unstructured.

**Figure 3.1. Features of the M2 cytoplasmic tail domain.**
(A) The domain structure of the full-length M2 protein indicating the 20 sites (50-70) that were the focus of this study, including previously published[18] sites 50-60. (B) CW X-band EPR spectra of full-length M2 protein for the indicated sites. Spectra were double integrated and normalized to the same number of spins. Some spectra were scaled in amplitude, as indicated by the scaling factor on the right-hand side of each spectrum. (C) The relative mobility (inverse central line width, $\Delta H_0^{-1}$) as a function of sequence position. Relative mobility values were extracted from the spectra shown in 1B. Error bars represent the uncertainty in the position of the peak maxima and minima.

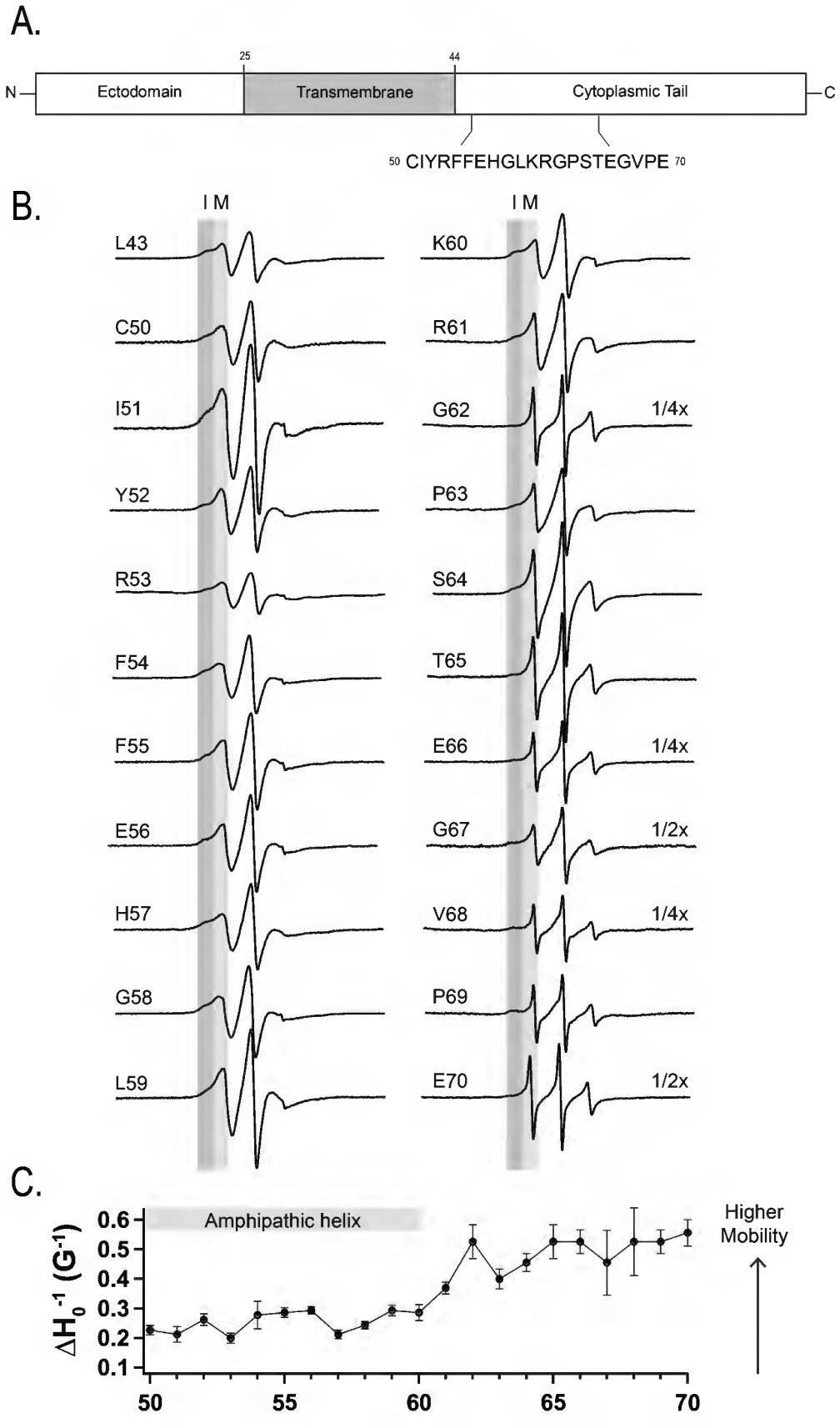
A.
25
44
N
Ectodomain
Transmembrane
Cytoplasmic Tail
C
50 CIYRFFEHGLKRGPSTEGVPE 70
B.
I M
I M
L43
C50
I51
Y52
R53
F54
F55
E56
H57
G58
L59
K60
R61
G62
1/4x
P63
S64
T65
E66
1/4x
G67
1/2x
V68
1/4x
P69
E70
1/2x
C.
Amphipathic helix
ΔH0-1 (G-1)
0.6
0.5
0.4
0.3
0.2
0.1
50
55
60
65
70
Higher
Mobility

**Analysis of Mobility Parameters Indicates That Sites C-Terminal to the Amphipathic Helix are Highly Dynamic.**

The relative rate of the motion of the spin label can be qualitatively assessed using the relative mobility factor. The semi-empirical mobility factor is calculated from the inverse peak-to-peak width of the central line ($\Delta H_0^{-1}$) of the EPR line shapes.[43,44] The utility of this method for identifying patterns that correlate to secondary structure has been demonstrated with helical hairpin and loop regions in Annexin.[51] The relative mobility as a function of M2 sequence position is shown in Figure 3.1C. The relative mobility of sites 50-60 is low, consistent with restrictions in backbone motion arising from an ordered, surface-absorbed secondary structural element in this region. In contrast, spin labels at positions 61-70 exhibit a steep gradient of increasing mobility, consistent with the sharp spectral features of the CW line shapes. The mobility site 62, a glycine in the native structure, is especially high, suggesting that backbone motions favor a break in this region of the sequence, possibly arising from termination of the amphipathic helix.

For spectra with a two-component nature, such as those produced by several sites investigated here, the central line width will be dominated by the fast motional component. In contrast, the second moment mobility parameter, which was not collected in this study, is dominated by the slower motional component.[51,70] These simple measurements of mobility have limited ability to report on the presence of different side chain conformations. Nonetheless, it is clear from both the line shape and relative mobility that residues 50-60 and 61-70 possess different motional properties.

**Accessibility Studies Show That Sites 50-60 Penetrate More Deeply into the Lipid Bilayer than Sites 61-70.**

To determine the structural topology of this region with respect to the bilayer, we conducted power saturation experiments to measure the accessibility of sites 50-70 to the membrane-soluble paramagnetic relaxation agent $O_2$, as described in the Materials and Methods. Oxygen accessibility as a function of spin-label position is presented in Figure 3.2A. Residue-by-residue patterns in accessibility to $O_2$ provide a topological map of secondary structure with respect to the membrane.[43] Previous analysis of positions 50-60 identified a sinusoidal variation in oxygen accessibility with a periodicity of 3.6, characteristic of a surface-absorbed α-helix.[17,18] Residues 62-70 exhibit a break in this pattern, suggesting that α-helical character does not extend into this region. The overall trend is one of decreasing oxygen accessibility towards the C-terminus of the amphipathic helix and beyond, revealing that this region is not as deeply buried in the lipid bilayer. These observations suggest that residues 63-70 adopt an extended, nonhelical conformation that may exit the membrane interface.

While $O_2$ accessibility provides information about the depth of a particular site in the membrane environment, these data can be difficult to interpret for residues positioned in the lipid head groups or aqueous environment. To gain additional insight about where specific sites lie along the membrane-aqueous interface, we employed two additional paramagnetic relaxation agents, NiEDDA and DOGS-NTA[Ni(II)], for select sites in the cytoplasmic domain.

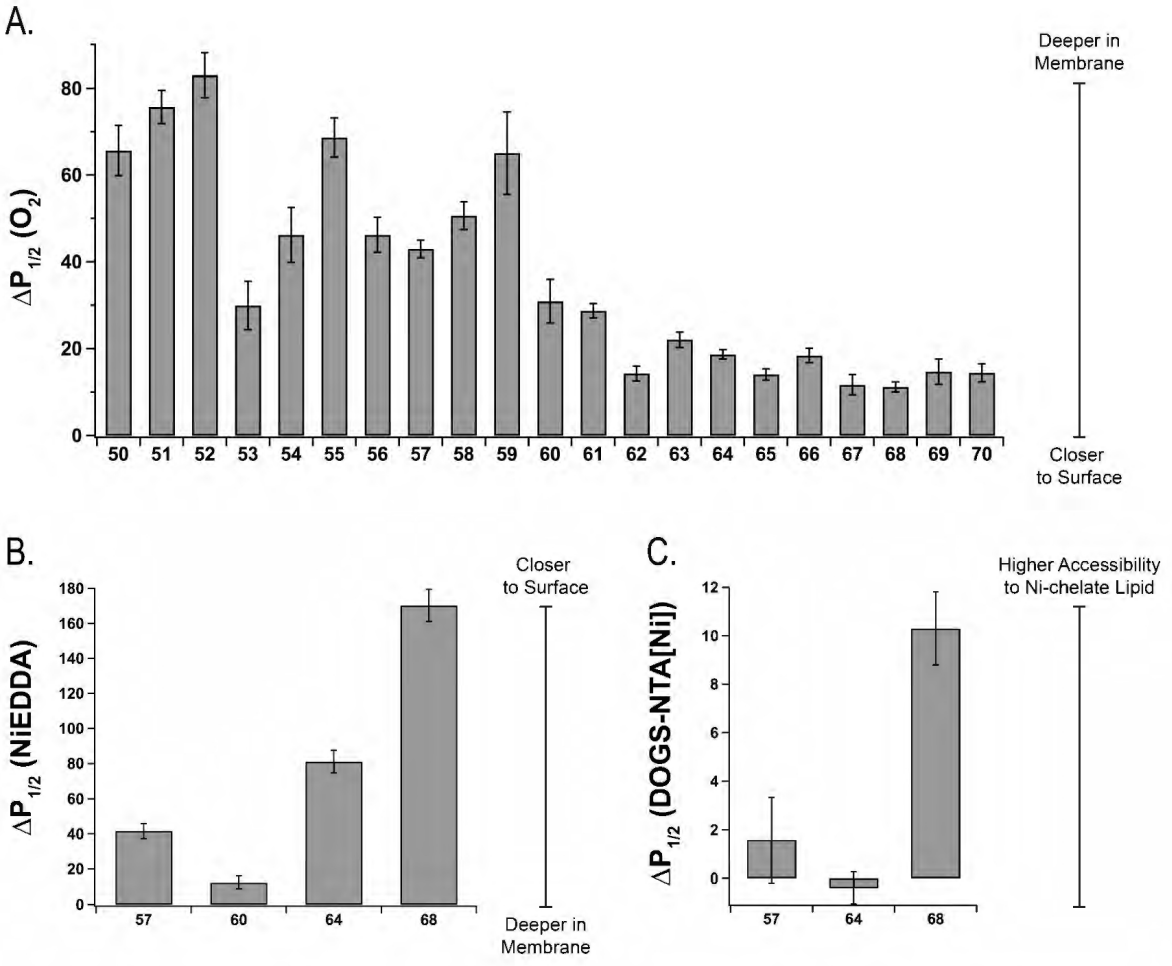


**Figure 3.2. The topology of the M2 cytoplasmic tail with respect to the membrane.** The accessibility of each spin-labeled residue to (A) membrane-soluble oxygen, (B) water-soluble NiEDDA, and (C) lipid-chelate DOGS-NTA[Ni(II)] is shown as a function of position. Error bars represent the 95% confidence intervals from the fits to the power saturation curves.

NiEDDA is a water-soluble paramagnetic relaxation agent commonly used to measure the accessibility of spin-labeled sites to the aqueous phase.[43] DOGS-NTA[Ni(II)] consists of a neutral lipid chelated to paramagnetic Ni(II) and has been used to measure the accessibility of protein side chains to the membrane-aqueous interface.[55] We measured the NiEDDA and Nickel-lipid accessibility of four sites in the cytoplasmic domain: H57, K60, S64, and V68. Sites 57 and 60, which lie at the C-terminal end of the

amphipathic helix, were included as references. Site 64 immediately follows the terminus of the amphipathic helix, which is likely disrupted by G62 and P63, and site 68 is near the end of the region investigated in these studies.

The NiEDDA accessibilities of select sites are shown in Figure 3.2B. As a general trend, spin label accessibility to NiEDDA increases with residue position, suggesting that the cytoplasmic tail becomes more solvent exposed towards the C-terminus. Because oxygen and NiEDDA are hydrophobic and hydrophilic species with opposite partitioning tendencies, a site's accessibility to these relaxation agents should complementary and self-consistent. We observe this trend with all residues except K60R1, which has both a low oxygen and NiEDDA accessibility. Such accessibility profiles are consistent with sites buried in a proteinous region[71]; however, given the expected position of this residue on the solvent-exposed face of the amphipathic helix, the low NiEDDA accessibility may arise from an experimental artifact.

The accessibility profiles of select sites to Ni-chelate lipid are shown in Figure 3.2C. Sites 57 and 64, expected to be located on the amphipathic helix and beyond the helix terminus, respectively, exhibit no significant collision frequency to the nickel chelate. Site 68 exhibits a moderate collision frequency with the Ni-lipid probe, suggesting that this residue resides within proximity of the lipid head groups. It is noted that previous studies utilizing the Ni-chelate lipid revealed that M2 amphipathic helix sites had higher accessibilities to the lipid head group than reported here[21], suggesting that the low accessibilities observed here may stem from differences in reconstitution protocols.

## DISCUSSION

A combination of EPR line shape, mobility, and accessibility analysis reveals that the M2 cytoplasmic tail consists of at least two distinct subdomains with different structural and dynamic features. Sites 50-60 of the proximal C-terminal domain form an amphipathic helix that lies on the surface of the membrane[18] and serve as an important point of comparison. Several large, bulky hydrophobic residues within the amphipathic helix appear to anchor this region in the lipid bilayer, as indicated by trends in oxygen accessibility and mobility data.

In contract, sites 61-70 appear to be a part of a dynamic region with no stable secondary structure in our model membrane system. As a general trend, the gradient in increasing backbone mobility towards the C-terminus mirrors decreasing membrane accessibility and increasing solvent accessibility for sites in this region, as measured by collision frequencies to oxygen and NiEDDA, respectively. Of the sites investigated for proximity to the lipid head groups, only the most distal residue exhibits significant accessibility to a nickel-chelate probe. Together, these observations suggest that this region does not make a sharp turn away from the membrane and towards the cytosolic space, but rather continues to extend along the membrane surface.

Sites 61-70 likely act as the C-cap of the amphipathic helix. Lysine and arginine residues exhibit preferences for the final turn of α-helices, and glycine and proline frequently occur at secondary structure termini.[72] Analysis of the spectral features of sites 60-63 reveals a sharp increase in mobility, suggesting that the end of the helix is encompassed within these residues. Although significant differences exist between the physiochemical properties of the nitroxide and native structure side chains, the high spin

label mobility at these sites like arises from several redundant mechanisms that instill flexibility in the backbone structure in this region.

The results presented here are generally consistent with previously NMR studies that attributed random coil chemical shifts to residues in the 61-70 region, although these signals could not be definitively resolved.[34]

**The Cytoplasmic Domain May Facilitate The Ion Channel and Scission Functions of M2.**

Dynamic and unstructured regions play critical roles in ion channel gating and protein-protein interactions.[73] In addition to the dynamic properties reported here, the M2 post-amphipathic helix cytoplasmic tail contains several highly conserved acidic residues (E66, E74, E75, E79, D85, D87, D88, E95, and E97[74]) in addition to the conserved residue S64, which is known to be phosphorylated *in vivo*.[75–77] The distal residues of the cytoplasmic domain therefore exhibit a striking reversal in physicochemical properties compared to the amphipathic helix, which contains several bulky, hydrophobic and basic residues.

It has recently been postulated that the full C-terminal domain facilitates M2 ion channel conductance by increasing the tilt angle of the transmembrane helices due to electrostatic repulsions between the cytoplasmic tails of each monomer.[78] The C-terminal domain also plays a critical role in influenza virus and morphology and budding.[35–38,40,58–60] Recent studies have investigated the regulatory function of disordered, highly acidic regions flanking curvature-inducing amphipathic helices such as α-synuclein and CTP:phosphocholine cytidylyltransferase.[79] Repulsion between these acidic moieties and the anionic lipid head-groups was hypothesized to augment curvature sensitivity of the

upstream amphipathic helix by decreasing electrostatic-dependent membrane binding. In support of this hypothesis, charge-abolishing mutations to these acidic residues decreased the curvature-dependent binding of the amphipathic helix.[79] It is tempting to speculate that the charged residues downstream of the M2 amphipathic helix function in a similar manner to regulate the curvature sensitivity of both the transmembrane and membrane-proximal domains. In accordance with this hypothesis, the full-length M2 protein has reduced ability to generate the negative Gaussian curvature necessary for viral scission relative to the M2 TMC construct, which comprises only the transmembrane and amphipathic helices.[41] This model requires additional experimental validation but opens up a new direction in understanding the structural, dynamic, and functional properties of the M2 cytoplasmic tail.

## SUMMARY AND CONCLUSIONS

The influenza A M2 cytoplasmic tail is necessary for proper viral infectivity and morphology, but only a limited number of biophysical studies have investigated the structure and dynamics of the full-length protein. We used SDSL-EPR to generate valuable new structural and membrane topology data for the C-terminal domain beyond the amphipathic helix. This region appears to be a part of a highly mobile unstructured segment under our model membrane conditions. We hypothesize that the flexibility and dynamic nature of the cytoplasmic tail may be functionally important for the many roles of the M2 protein in viral assembly and budding.

## CHAPTER 3 CONTRIBUTIONS

Alice Herneisen '17 designed primers for all single-cysteine constructs, generated the plasmids for sites 63-65 and took these constructs through the complete expression,

purification, spin labeling, and reconstitution, and data collection protocol. Alice Herneisen also performed all reconstitutions that used nickel paramagnetic relaxation agents and collected and analyzed the data. Grace Kim '17 generated the single-cysteine plasmids for sites 61, 62, and 66-70 and took these constructs through the complete expression, purification, spin labeling, and reconstitution, and data collection protocol. Shenstone Huang '16 and Bryan Green '16 performed the purification, spin labeling, reconstitution, and data collection protocols for the single-cysteine 50-60 constructs. Alice Herneisen prepared proteoliposomes for circular dichroism and Dr. Kathleen Howard (Swarthmore College, Swarthmore, PA) collected spectra.

## SUPPORTING INFORMATION

The Supporting Information for this Chapter 3 is located in Chapter S1.

# Chapter 4: Cholesterol-Dependent Conformational Exchange of the Full-Length Influenza A M2 Protein and a Mutant Exhibiting Impaired Viral Scission

## INTRODUCTION

Enveloped viruses, including influenza, Ebola, and HIV, commonly hijack host membrane lipid rafts enriched in cholesterol to facilitate viral fusion and budding. It has been proposed that viral fusion and scission machinery, such as the HIV fusion peptide gp41[80] and the influenza A M2 protein[11,29,81], preferentially associate with the edge of cholesterol-rich domains to promote membrane deformation. However, molecular-level details of the roles cholesterol plays in protein-mediated viral fusion and fission are not well-understood. Here, we investigate the impact of cholesterol on the conformation and dynamics of the cytoplasmic tail of the influenza A M2 protein as well as a mutant that is defective in viral budding.

The M2 protein is a 97-amino acid homotetrameric ion channel.[14] Although the proton-conducting transmembrane domain has been characterized in detail using a variety of biophysical techniques, less is known about the structure of the cytoplasmic tail.[10] Like many other proteins involved in membrane remodeling, the M2 protein contains a membrane-associated amphipathic helix.[17,18] Functional assays have demonstrated that this amphipathic helix is necessary and sufficient to induce cholesterol-dependent budding.[11]

Mutagenesis studies identified the importance of key hydrophobic residues in the amphipathic helix. Alanine substitutions to residues facing the membrane interior (F47A, F48A, I51A, Y52A, and F55A) abolished viral filament formation and resulted in virus

particles with the scission-defective beads-on-a-string morphology.[12,40] Functional studies of this same penta-alanine substitution construct, henceforth referred to as M2 pentaAla, were complemented by *in vitro* assays showing that these mutations reduce the ability of the M2 protein to induce budding in membrane mimetic systems[11], presumably through a reduced ability to restructure membrane curvature.[41]

Here, we seek a structural understanding of this mutant protein with the goal of understanding how the wild-type protein functions. The reported loss of function in the pentaAla construct may result from a disruption in the local secondary structure, changes in packing within the homotetramer, alteration of amphipathic helix topology with respect to the membrane, or impaired ability to respond to the presence of cholesterol, which is essential for viral budding.[12] We attempt to distinguish between these possibilities using site-directed spin-labeling electron paramagnetic resonance spectroscopy (SDSL-EPR). SDSL-EPR is a powerful technique for studying membrane proteins in lipid bilayers and is especially well-suited for detecting conformational dynamics. Our group has previously used this method to demonstrate the sensitivity of truncated M2 constructs to the surrounding membrane environment.[17,20,22,23]

This study represents the first efforts to probe the structure and conformation of the full-length penta-alanine mutant in atomic-level detail. First, we show that the amphipathic helix of the full-length wild-type protein exists in at least two different conformations that differ in backbone mobility and membrane depth. The presence of cholesterol shifts the relative populations of these two conformational states. The conformational equilibrium of the pentaAla mutant differs significantly from that of the

wild-type protein, indicating that the ability to undergo cholesterol-dependent conformational exchange is necessary for the scission activity of the M2 protein.

## MATERIALS AND METHODS

Detailed materials and methods are provided in *SI Materials and Methods* in Chapter S2.

### M2 and pentaAla Purification and Spin Labeling.

Alanine and cysteine mutations were introduced into a cysteineless plasmid background using QuikChange Multi and Lightning Site-Directed Mutagenesis kits, respectively. Amino acid sequences are available in Appendix C. All DNA constructs were verified using fluorescence-based automated sequencing services (Genewiz Inc., NJ, USA). The M2 L43C and pentaAla cysteine constructs were expressed in C43 cells (Lucigen, WI, USA). All other M2 constructs were expressed as previously described (Chapter 3). Proteins were purified and spin labeled using previously established protocols, and the purity was assessed using SDS-PAGE (Figure S2.1).[18] Hereafter, the single-cysteine M2 variants are referred to as "wild-type" or simply "M2", and alanine M2 variants are referred to as "pentaAla"

### Reconstitution of M2 Protein into Liposomes.

Full-length M2 protein was reconstituted into liposomes consisting of 4:1 POPC:POPG, 4:1 POPC:POPG with 30 mol% cholesterol, 4:1:1.25 DOGS-NTA[Ni(II)] and 4:1:1.25 DOGS-NTA[Ni(II)] with 30 mol% cholesterol. The lipids were prepared by combining chloroform lipid solutions in the designated molar ratios and dissolving the chloroform under a gentle stream of nitrogen gas followed by lyophilization overnight. The lipid films were rehydrated in the following buffers: for CW and oxygen power

saturation samples, 50 mM Tris pH 8, 100 mM KCl, 1 mM EDTA; for NiEDDA power saturation, 50 mM Tris pH 8, 100 mM KCl, 50 mM NiEDDA; for DOGS-NTA[Ni(II)] power saturation, 50 mM Tris pH 8, 100 mM KCl. The remainder of the reconstitution protocol followed previously published protocols.[18] The proteoliposome solution was concentrated by two rounds of ultracentrifugation at 90,000 rpm for 60 minutes at 4°C. The samples were frozen at -20°C and thawed prior to data collection.

### EPR Continuous Wave and Power Saturation Measurements.

EPR data collection has been described previously (Chapter 3).

## RESULTS

### M2 Conformation and Dynamics Are Sensitive to Cholesterol.

Choice of membrane mimic can have a profound effect on the conformation and structure of membrane proteins. Here, we study the structure and dynamics of M2 in POPC:POPG bilayers. These bilayers have been used in SDSL-EPR[17,18,21–23] and NMR[34] studies as well as *in vitro* budding assays that demonstrated the cholesterol-dependence of M2 budding activity.[11] Previous experiments indicated that the addition of 30 mol% cholesterol is sufficient to induce conformational exchange in a truncated version of the M2 construct and provide valuable context for this study.[20]

We chose to investigate eight sites spanning the C-terminal end of the transmembrane domain to the distal cytoplasmic tail (Figure 4.1A). The EPR line shape produced by a nitroxide side chain, R1, provides information on the effects of the surrounding chemical environment on the mobility of the spin label probe.[43] CW X-band EPR spectra for the eight spin-labeled M2 sites are shown in Figure 4.1B. Site 43 exhibits

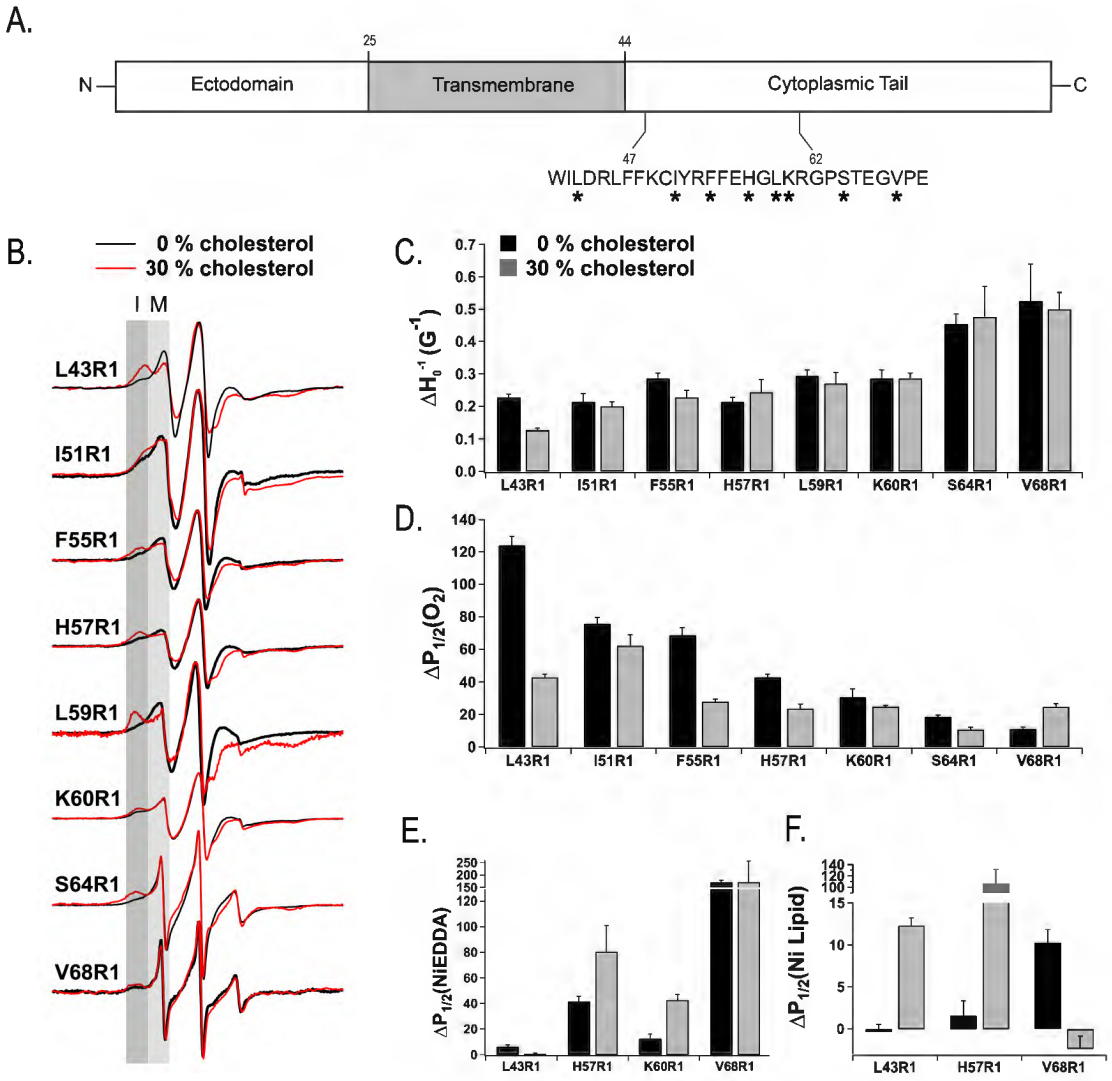


**Figure 4.1. M2 populates two conformations in the presence of cholesterol.** (A) Domain structure of the full-length M2 construct used in these studies. The identity of sites 43-70 is shown. Spin-labeled sites are marked with an asterisk (*). (B) Continuous wave X-band EPR spectra of the indicated spin-labeled sites in 4:1 POPC:POPC bilayers with 0% (black) and 30% (red) cholesterol. Spectra of V68R1 were of much higher amplitude than other sites and are shown at reduced intensity. The light gray (M) and dark gray (I) boxes highlight the mobile and immobile peaks, respectively. The scan width is 150 G. (C) The inverse central line width (relative mobility) of the indicated sites obtained from the spectra of spin labeled protein reconstituted into membrane with 0% (black) or 30% (gray) cholesterol. Accessibility data to (D) oxygen, (E) NiEDDA, and (F) Ni-chelate lipid for M2 at the indicated sites in POPC:POPG bilayers with 0% (black) or 30% (gray) cholesterol.

broad peaks characteristic of a membrane-buried R1, consistent with the position of this residue on a transmembrane helix. Sites 51, 55, 57, 59, and 60 also exhibit broadened peaks, likely due to contacts with the membrane. Sites 64 and 68 display sharper, narrower peaks, suggesting that low motional restriction of the spin label exists at sites distal to the amphipathic helix. The high mobility of these sites is consistent with NMR studies that attributed random coil chemical shifts to residues S64 and V68.[34,62]

As shown in Figure 4.1B, spectra of all sites except V68R1 exhibit a notable two-component nature that is sensitive to the addition of cholesterol. The two spectral components are indicated as mobile (M) or immobile (I). Both components exist in 4:1 POPC:POPG membranes, indicating that an equilibrium exists between the two conformations. Increasing the cholesterol concentration increases the relative intensity of the broader, more immobilized peak, demonstrating that this conformation is preferentially stabilized by cholesterol. This trend is observed for sites at the end of the transmembrane helix (L43), on both faces of the amphipathic helix (I51, F55, H57, L59), and residues flanking the amphipathic helix terminus (S64), suggesting that the shift in spectral components results from a concerted cholesterol-dependent conformational change rather than a localized effects for any one site.

The distal cytoplasmic tail site, V68R1, exhibits only a small amount of the immobile component, but the addition of cholesterol does not shift the relative weights of the mobile and immobile peaks. This observation is consistent with the absence of cholesterol-induced conformational change in the region of the C-terminal tail beyond the amphipathic helix. Alternatively, the motion of the R1 side chain may be similar in both

conformations, and conformational exchange may not be detectible using line shape analysis.

The inverse central line width ($\Delta H_0^{-1}$) of an EPR spectrum serves as a semi-empirical mobility parameter that is proportional to the correlation time of the nitroxide probe.[44] A plot of the mobility parameter in membranes with differing cholesterol content is shown in Figure 4.1C. Sites 43 and 55 exhibit a measurable reduction in mobility parameter when the cholesterol concentration of the membrane increases. In contrast, the mobility parameters of the remaining sites do not detectibly change within experimental error upon the addition of cholesterol to the membrane. However, for spectra with a multi-component nature, such as M2[82], the central line width will be dominated by the mobile component.[44] Spectral simulation can resolve these ambiguities and is discussed in the Supporting Information Discussion (Chapter S2).

### Saturation Recovery Data Indicate Conformational Exchange of the C-Terminal Amphipathic Helix.

Two-component line shapes in Figure 4.1B may arise from two different rotamers of the spin label or a conformational equilibrium between two different states of the M2 C-terminal domain.[47] Saturation recovery (SR) EPR distinguishes between these two possibilities through the method of delivering an intense pulse at the frequency of the central line width and monitoring the return to spectral intensity, which occurs with a relaxation rate and $T_1$ time constant.[47] A spin label in rotameric exchange gives rise to a single-exponential recovery, whereas a spin label in a system undergoing conformational exchange experiences a bi-exponential recovery resulting from two unique spin-lattice relaxation rates. Furthermore, R1 rotameric exchange occurs on the 0.1-1 $\mu$s timescale,

whereas conformational exchange is much slower.[47] Previous SR-EPR studies of truncated M2 constructs in 4:1 POPC:POPG bilayers indicated that the M2 spin labels on the amphipathic helix undergo conformational exchange rather than rotameric exchange.[20]

To extend these findings to the full-length protein, we collected SR data for site 57 in POPC:POPG membranes with 0% and 30% cholesterol (Table 4.1). Figures for these results are in preparation. Saturation recovery curves for H57R1 in both membrane systems are characterized by double-exponential recoveries, consistent with conformational exchange at this site. Furthermore, the T1 values for this site too slow for rotameric exchange (Table 4.1).

**Table 4.1. Saturation recovery data identify two components in conformational exchange.**
Data were collected on M2 and pentaAla H57R1 reconstituted into 4:1 POPC:POPG proteoliposomes with 0% and 30% cholesterol. "Fast" and "slow" refer to the relative relaxation times of the spin label in the two different conformations.

| Construct | Lipid composition | $T_1$ fast (μsec)[a] | $T_1$ slow (μsec)[a] | $W_x$ fast (MHz/mM $O_2$)[b] | $W_x$ slow (MHz/mM $O_2$)[b] |
|---|---|---|---|---|---|
| M2 H57R1 | 4:1 POPC:POPG | 3.23 | 7.6 | 4.09 | 0.85 |
| M2 H57R1 | + 30% cholesterol | 3.47 | 6.94 | 2.17 | 0.46 |
| 5Ala H57R1 | 4:1 POPC:POPG | 2.42 | 7.53 | 2.73 | 0.53 |
| 5Ala H57R1 | + 30% cholesterol | 2.84 | 7.64 | 2.38 | 0.5 |

[a]spin-latice relaxation times were determined in 0% oxygen, i.e. in nitrogen
[b]slopes of $O_2$ collision rates obtained by collecting data at five different oxygen concentrations

The spin-lattice relaxation rate can be modulated by the presence of paramagnetic relaxation agents like oxygen. The relaxation rate of the nitroxide spin label is proportional to the collision rate of the label with the relaxation agent. When the R1 collision rate with oxygen is measured as a function of oxygen concentration, spin labels

with higher oxygen accessibility will exhibit a steeper slope.[47] Table 4.1 reports the slopes of the R1 collision rates obtained by collecting data in 0, 20, 40, 60, and 100% air. The slow component exhibits a lower dependency on oxygen than the fast component in both 0% and 30% membranes. Because oxygen preferentially partitions into membranes, these findings are consistent with the slow component being less deep in the membrane. The saturation recovery profiles of additional sites will need to be recorded in order to show that the double-exponential recovery and differing oxygen accessibilities of the two conformations are not localized to a single site. Nonetheless, complementary EPR techniques can be used to probe the membrane accessibility of additional sites in different conformations, as discussed below.

**The Conformational State Stabilized by Cholesterol Is Less Deep in the Membrane.**

In order to investigate the properties of the two conformations populated by the C-terminal region, we performed power saturation experiments using three different paramagnetic reagents. Power saturation is a collision gradient method that reports on the relative accessibility of R1 to oxygen and nickel relaxing agents.[43,44,55] Briefly, sites buried more deeply in the membrane have higher oxygen accessibilities. Conversely, solvent-exposed sites have higher soluble NiEDDA accessibilities. Trends in spin label oxygen and NiEDDA accessibilities can reveal a protein's topology with respect to the membrane. Accessibility to an additional relaxation agent, DOGS-NTA[Ni], provides informational about the proximity of the spin label to the lipid head groups.[55] Previous SDSL-EPR studies of the M2 protein have revealed changes in the oxygen and nickel

accessibilities of spin-labeled sites on the amphipathic helix in response to changes in the pH[17], composition of the membrane[20], and presence of adamantane drugs.[21]

The oxygen accessibility of each spin labeled site is shown in Figure 4.1D. All sites in the transmembrane domain (L43) and amphipathic helix (I51, F55, H57, and K60) exhibit decreased accessibility to oxygen with the addition of cholesterol to the membrane, consistent with the amphipathic helix becoming less buried in the membrane. Site 64, which is C-terminal to the amphipathic helix, exhibits a similar decrease in oxygen accessibility in the presence of cholesterol; however, the more distal cytoplasmic tail residue (V68) does not exhibit the same trends.

Caution must be used in interpreting changes in nitroxide oxygen accessibilities upon altering the membrane composition. The addition of cholesterol to membrane mimetics alters the partitioning of oxygen into the bilayer.[83] Previous studies of the permeability of oxygen in the membranes used here indicated that cholesterol-dependent restrictions in oxygen diffusion are greatest in the glycerol backbone region where the amphipathic helix resides.[84] The apparent decrease in the R1 oxygen accessibilities upon the addition of cholesterol to the membrane could therefore partially represent a decrease in the partitioning of oxygen into the bilayer.

To verify that the cholesterol-dependent decrease in the oxygen accessibilities of M2 nitroxide derivatives was not a result of altered membrane oxygen permeability, we measured the accessibility of select spin labeled protein sites to the aqueous paramagnetic agent NiEDDA in POPC:POPG and POPC:POPG membranes with 30% cholesterol (Figure 4.1E). As oxygen and NiEDDA partition into different phases, the trends in accessibility data should be complementary. Sites 57 and 60 show increased accessibility

to NiEDDA when M2 is reconstituted into membranes containing cholesterol, consistent with the amphipathic helix becoming less buried in the membrane. Site 68 has a large accessibility to NiEDDA in bilayers with and without cholesterol, indicating that this site is highly exposed to the aqueous phase. The trends in the NiEDDA and oxygen accessibility profiles for these four sites are thus self-consistent, supporting the interpretation of the oxygen accessibility data provided above. Only one site located on the transmembrane domain, L43R1, failed to produce complementary data from the accessibility studies and is discussed further below.

Non-self-consistent trends in oxygen and NiEDDA accessibilities have been previously observed in an adjacent site in the transmembrane helix[82] and may reflect the topographical features of this region of the protein. In the less tightly packed conformation of the protein that is predominant in 4:1 POPC:POPG membranes, NiEDDA may penetrate into the C-terminal base of the transmembrane pore.[44] In contrast, tight packing of the transmembrane helices in the conformation that is stabilized by cholesterol may result in the exclusion of NiEDDA from the base of the pore. The decrease in NiEDDA accessibility of this site may therefore be rationalized in light of the predicted conformational change occurring in this region.[20]

In a final effort to distinguish between the topography of the two conformations, we measured the accessibility of a subset of sites to paramagnetic Ni(II) chelated to a lipid head group, which has been used previously to identify R1 sites proximal to the membrane surface.[55] The accessibilities of sites 43, 57, and 68 to the Ni-chelate lipid is shown in Figure 4.1F. The Ni-chelate lipid accessibility of site 43 in 4:1 POPC:POPG membranes is lower than previously reported for the corresponding site in the truncated

M2 construct.[21] This difference may reflect altered conformational properties in the full-length M2 construct or could result from variations in the reconstitution protocol. In the absence of cholesterol, only site 68 exhibits a small accessibility to the Ni head group, consistent with the localization of this residue beyond the phospholipid head groups (Chapter 3).

With the addition of cholesterol, the accessibility of site 57 to Ni-chelate lipid increases dramatically, consistent with the movement of the amphipathic helix away from the membrane. The Ni-chelate lipid accessibility of site 43 also increases with the addition of cholesterol, consistent with oxygen accessibility data indicating that this site is not as buried in the membrane in the less mobile conformation. Site 68 no longer exhibits accessibility to the Ni-chelate lipid, suggesting that this site occupies a region removed from the head groups when cholesterol is present in the membrane. Taken together, these accessibility data demonstrate that the two conformations observed in CW EPR line shapes exhibit different topologies with respect to the membrane.

### The PentaAla Mutant Exhibits Altered Conformational Dynamics.

Previously, we postulated that the conformation of M2 with amphipathic helices less mobile and less deep in the membrane is predominant in the neck of a budding virus, where cholesterol is concentrated.[20] *In vitro* budding assays revealed that alanine substitutions to five bulky, hydrophobic residues facing the membrane interior (pentaAla: F47A, F48A, I51A, Y52A, and F55A; see Figure 4.2A and B) abolished the ability of M2 to spontaneously induce vesicle budding from giant and large unilamellar vesicles.[11] To correlate the cholesterol-dependent conformational exchange of the wild-type M2 protein

with scission activity, we reproduced the pentaAla construct in the full-length cysteineless background and characterized its conformational dynamics using SDSL-EPR. In order to minimize further disruptions to the hydrophobic face of the helix, a labeling site located on the solvent-facing side of the helix was selected to report on the properties of this region (Figure 4.2A and B).[18,19] An additional site on the transmembrane helix was labeled to measure the effect that amphipathic helix mutations have on other domains of the protein. We discuss the results first in the context of the amphipathic helix site (H57) followed by possible implications for the transmembrane site (L43).

Side-by-side comparisons of the line shapes of M2 and pentaAla with spin labels at sites 43 and 57 are shown in Figure 4.2C and D. A striking feature of the pentaAla H57R1 spectrum is the increased intensity of the mobile component. This observation suggests that in the mutant the conformational equilibrium between the two amphipathic helix conformations is heavily shifted towards the more mobile conformation. The intensity of the immobile peak increases with the addition of cholesterol, demonstrating that a population of the mutant maintains the ability to undergo conformational exchange, though not to the same extent as the corresponding site in the wild-type protein.

One unexpected feature of the mutant L43R1 spectrum is the higher relative weight of the immobile component in comparison to the corresponding M2 site in POPC:POPG bilayers lacking cholesterol. Furthermore, the addition of cholesterol fails to appreciably alter the intensities of the two components, suggesting that the mutant transmembrane helices no longer undergo conformational exchange or that the chemical

environment surrounding the spin label is similar in both conformations, in contrast to the wild-type protein.

Consistent with the observed variations in line shape, the pentaAla nitroxide variants exhibit altered motional properties in comparison to the same sites in M2. A comparison of the relative mobility ($\Delta H_0^{-1}$) of spin-labeled sites in membranes with and without cholesterol is provided in Figure 4.2E. The mobility of the spin label on the pentaAla amphipathic helix is much higher than the corresponding M2 site in membranes with and without cholesterol. The addition of cholesterol slightly decreases the relative mobility of pentaAla H57R1 but does not appear to affect the mobility of the same site in M2. In contrast, the mobility of pentaAla L43R1 in 4:1 POPC:POPG bilayers is lower than the mobility of the corresponding site in M2. Whereas the addition of cholesterol causes the mobility of L43R1 to decrease in M2, no change in mobility is observed the corresponding site in pentaAla.

In order to resolve the ambiguities of mobility analysis that arise from multi-component spectra and to gain more quantitative information about the motion experienced by the spin label in the two conformations, we performed spectral simulation for sites 43 and 57 using MultiComponent, a LabVIEW program based on the MOMD approach.[48] Spectra were simulated with two motional components to produce a reasonable fit (Figure S2.2). Because of the preliminary nature of these fits, additional interpretation and analysis is provided in the Supporting Information Discussion. These spectral simulations were performed with the assumption that the pentaAla mutant continues to sample a two-conformational equilibrium and require further experimental validation.

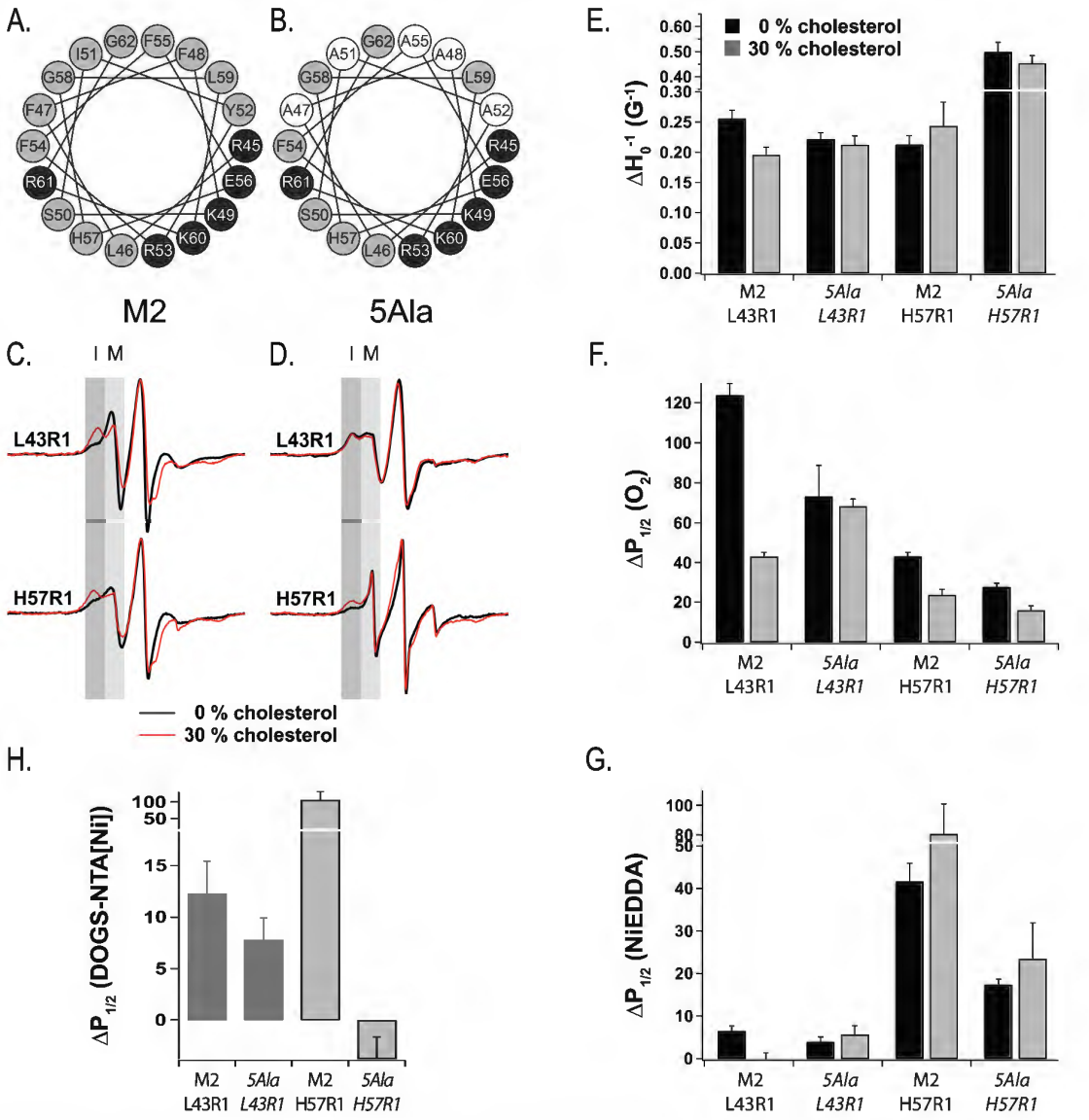


**Figure 4.2. Mutation to five hydrophobic residues in the M2 amphipathic helix alters the conformational dynamics of M2.**

Helical wheel representation of the amphipathic helix of (A) wild-type M2 and (B) pentaAla. Charged and neutral residues are shown in black and gray, respectively. The five alanine substitutions are denoted by white circles. Continuous wave X-band EPR spectra of the indicated spin-labeled sites in 4:1 POPC:POPC bilayers with 0% (black) and 30% (red) cholesterol for the indicated sites in wild-type M2 (C) and pentaAla (D). The light gray (M) and dark gray (I) boxes highlight the low-field mobile and immobile peaks, respectively. For site 43, dilute-labeled spectra are shown to eliminate the effect of static dipolar broadening. Because the spectral line shape is biased towards the mobile component, the spectra shown here were normalized to the height of the central peak to facilitate comparison of the immobile component. (C) The inverse central line width (relative mobility) of the indicated M2 and pentaAla sites obtained from the spectra of spin labeled protein reconstituted into membrane with 0% (black) or 30% (gray) cholesterol. Accessibility data to (E) oxygen, (F) NiEDDA, and (G) Ni-chelate lipid for M2 and pentaAla in 4:1 POPC:POPG bilayers with 0% (black) or 30% (gray) cholesterol.

### Saturation Recovery Data Indicate PentaAla Still Undergoes Conformational Exchange of the C-Terminal Amphipathic Helix.

To assess whether the pentaAla amphipathic helix continues to occupy a two-state equilibrium, we collected saturation recovery data for site 57 in 4:1 POPC:POPG membranes with 0% and 30% cholesterol (Table 4.1). As with the corresponding site in M2, the pentaAla H57R1 SR curve is characterized by a bi-exponential recovery and $T_1$ indicative of conformational exchange. Similarly, the relaxation rate of the slow component exhibits a lower dependency on oxygen than the fast component in both 0% and 30% membranes. Currently, saturation recovery experiments can report the differing relaxation times and oxygen-dependent relaxation rates of the two conformations, but not the relative population of the two conformations (Dr. Jim Feix, personal communication). Saturation recovery data for site pentaAla 57 are therefore consistent with two conformations with different oxygen accessibilities in equilibrium. We refrain from comparing the magnitudes of the spin-lattice relaxation times and rates of M2 and pentaAla until the experiment has been repeated.

### Accessibility Studies Show That the PentaAla Mutant Has Altered Topology with Respect to the Membrane.

An important property of curvature-sensing and curvature-inducing amphipathic helices is their ability to insert into the membrane.[85] Sites F47, F48, I51, Y52, and F55 in the wild-type protein are known to be buried in the membrane in our biomimetic system.[17] The loss of function observed in the penta-Ala mutant has been proposed to result from a reduction in the ability of the amphipathic helix to insert in the membrane.[12,42] In order to measure the topology of the selected sites with respect to the

membrane and to characterize the conformations of the pentaAla transmembrane and amphipathic helices, we performed accessibility analysis using the same paramagnetic relaxation agents discussed previously.

Accessibility profiles of spin labels at sites 43 and 57 in the wild-type and pentaAla mutant are shown in Figure 4.2F-H. The pentaAla amphipathic helix site has decreased accessibility to oxygen and increased accessibility to NiEDDA upon the addition of cholesterol to the membrane. Qualitatively, these differences are similar to those seen for the same site in the wild-type protein. One interesting observation is that pentaAla H57R1 has both lower oxygen and NiEDDA accessibility than the corresponding site in M2 in membranes with and without cholesterol. This observation is explored further in the Supporting Information Discussion. Because few sites investigated here exhibited strong accessibility to the nickel-chelate lipid in 4:1 POPC:POPG bilayers, we only explored the accessibilities of the mutant protein in 30% cholesterol membranes (Figure 4.2H). The pentaAla H57R1 has no accessibility to the nickel-chelate lipid, indicating that this site in the pentaAla mutant no longer stably resides at the level of the lipid head groups in the presence of cholesterol.

In contrast to site 43 in the M2 construct, which experiences a pronounced reduction in oxygen accessibility upon the addition of cholesterol to the membrane, the oxygen accessibility of pentaAla L43R1 is similar in both bilayer systems. Likewise, the NiEDDA accessibility of this site in the mutant does not detectibly change in response to cholesterol. The spin-labeled sites on the C-terminal transmembrane domain of both M2 and pentaAla appear to exhibit similar accessibilities to this relaxation agent in membranes with cholesterol. Taken together, these data suggest that the conformational

equilibrium of the pentaAla transmembrane domain is unaffected by the addition of cholesterol to the membrane, and this equilibrium favors a conformation that is more similar to the conformation of M2 that becomes more populated in the presence of cholesterol.

### Assessing Global Secondary Structure of the M2 and PentaAla Constructs.

One possible explanation for the increased mobility of the pentaAla amphipathic helix spin label is that mutations to the helix cause the region to become disordered. Alanine residues possess neutral secondary structure preferences and tend to adopt the backbone conformation of the native residue[86], and protein sequence analysis algorithms[64] predict that pentaAla residues 24-57 adopt a helical structure (Figure S2.3). However, membrane binding studies have shown that a 21-residue peptide corresponding to the M2 amphipathic helix is disordered in solution only only folds into a helix upon membrane binding.[42,87] Significantly perturbing the hydrophobic face of the helix by mutating residues F47, F48, I51, Y52, and F55 may disrupt the amphipathicity of the helix and decrease insertion depth and, consequently, membrane interaction. Therefore, alanine substitutions on the hydrophobic face of the amphipathic helix may reduce the propensity of this region to adopt an α-helical structure.

To determine if the pentaAla mutant has less global α-helical structure than the wild-type construct, we performed circular dichroism experiments on cysteineless M2 and pentaAla in 4:1 POPC:POPG liposomes with and without cholesterol. The CD signal of these constructs is shown in Figure S2.4. Collecting and analyzing the CD spectra of membrane proteins presents unique challenges and requires careful interpretation.[88] Due

to the large scattering effects of proteoliposomes and the low peptide:lipid ratio used in these experiments, quantitative information cannot be extracted from these spectra. Nonetheless, the CD spectra exhibit the characteristic alpha-helical CD signatures with negative bands at approximately 222 and 208 nm and a strong positive peak at 190 nm. Preliminary CD evidence suggests that the cysteineless M2 and pentaAla constructs exhibit similar global secondary structure characteristics (Supporting Information Discussion, Chapter S2).

## DISCUSSION

Data from line shape analysis, accessibility parameters, and spectral simulation suggest that the transmembrane and amphipathic helix regions of the M2 undergo concerted conformational exchange in response to the presence of cholesterol in the membrane. The conformation that is more highly populated in the presence of cholesterol is less dynamic and less membrane-buried than the other state. These observations are generalizable for sites on the amphipathic helix; however, the magnitude of the effect is not as large for sites distal to the amphipathic helix and may reflect the conformational heterogeneity of this region (Chapter 3).

To further dissect the effect of cholesterol on M2 conformational exchange, we recreated a mutant that has demonstrated impaired association with cholesterol[12] and deficiencies in budding both *in vitro*[11] and *in vivo*[12,40] and adapted it for atomic-level biophysical studies. Substitutions to several large hydrophobic amino acids on one face of the amphipathic helix severely shift the conformational equilibrium of this region towards the more mobile conformation that has amphipathic helices more deeply buried in the membrane. As an unanticipated result, a site near the end of the transmembrane

helix adopts a conformation that is less mobile and less membrane-buried. The five alanine substitutions in the amphipathic helix abolish the ability of the transmembrane domain to undergo detectable cholesterol-dependent conformational exchange. Collectively, these observations serve as strong evidence that the conformation of the wild-type M2 amphipathic helices that is more populated as the presence of cholesterol is the scission-relevant conformation.

### Properties of the Amphipathic and Transmembrane Helices Required for Cholesterol-Dependent Conformational Exchange.

Numerous studies have demonstrated that the scission activity of the M2 protein is encoded within the amphipathic helix, and mutations to five key hydrophobic residues is sufficient to abolish this activity.[11,12,40,42] Although the mechanisms by which the M2 amphipathic helices may modulate budding have been the subject of intense speculation[27,29], atomic-level studies of this scission function have been limited.

It has alternatively been proposed that the loss of scission activity observed in the pentaAla mutant may arise from the inability of the mutant amphipathic helices to insert as deeply into the membrane[11] or bind cholesterol.[12] In support of the first hypothesis, a lipid-binding assay revealed that a peptide corresponding to the pentaAla amphipathic helix did not insert as deeply into the membrane as the corresponding M2 sequence.[42] Consistent with these recent findings, oxygen accessibility data reported here suggest that pentaAla H57R1 is not as deeply buried in the membrane as the corresponding M2 site.

Several functional assays have provided evidence that the M2 protein is capable of binding cholesterol[12,27,29]; however, biophysical studies have been unable to distinguish between conformational change induced by direct cholesterol binding[32,89] or cholesterol-

dependent changes in the properties of the membrane.[20] Cholesterol has a condensing effect on liquid-disordered phases[25], such as those studied here, and consequently increases membrane thickness.[90] Previous EPR studies have demonstrated that the M2 transmembrane helices are sensitive to the thickness of the bilayer.[22] However, the additional feature of the membrane lateral pressure profile was required in order to rationalize the dependence of transmembrane conformational equilibrium on the surrounding hydrophobic environment.[23] Cholesterol has a complex effect on the lateral pressure profile of the membrane, increasing the pressure in the bilayer interior while decreasing the lateral pressure of the interfacial region.[25]

We hypothesize that the conformational state stabilized by the presence of cholesterol may be rationalized due to the sterol's effects on membrane mechanics. Cholesterol-dependent increases in membrane thickness and the interior lateral pressure profile may favor a conformation in which the M2 transmembrane helices are more tightly packed[22,23] and less dynamic.[20] An increase in interior lateral pressure and decrease in the interfacial lateral pressure may serve to respectively "push" and "pull" the amphipathic helices towards the lipid head groups, where the helices can induce packing defects that deform the membrane. This model is consistent with the decreases in mobility and oxygen accessibility observed for the C-terminal transmembrane domain and the increases in accessibility to NiEDDA and a Ni-chelate lipid for the amphipathic helix site.

The results of the experiments performed with the penta-alanine mutant provide some insight about how conformational exchange in the transmembrane and amphipathic helices may be coupled. The five alanine substitutions appear to shift the conformational

equilibrium away from the more immobile amphipathic helix conformation. The mutations have the concomitant and intriguing effect of altering the conformational equilibrium and exchange of the pentaAla C-terminal helix site. In comparison to the corresponding site in M2, pentaAla L43R1 is less dynamic and less deep in the membrane in bilayers without cholesterol. Furthermore, the pentaAla L43R1 line shape is insensitive to the addition of cholesterol, and this observation tracks well with the corresponding accessibility data. At first glance, the conformation favored by the pentaAla transmembrane helices under both membrane conditions resembles the conformation favored by the M2 transmembrane helices in the presence of cholesterol. Undoubtedly further investigation is required to confirm this hypothesis, especially since we have limited insight about the arrangement of the helical bundle in the pentaAla mutant.

However, a picture emerges in which the wild-type M2 amphipathic helices function to induce looser packing of the transmembrane helices in 4:1 POPC:POPG membranes through several redundant mechanisms. Previous SDSL-EPR studies revealed that a K49C mutation abolished M2 ion channel function.[17] This lysine residue was hypothesized to prevent channel collapse by "anchoring" the transmembrane domain to the interfacial region of the membrane.[91] We hypothesize that the large, hydrophobic amino acids lining one face of the amphipathic helix act in a similar manner. Conformational plasticity appears to be a functional requirement for the M2 ion channel and scission functions. Stabilizing mutations to the transmembrane helix-helix interface have gone untapped[92], suggesting that selective pressure exists for the transmembrane helices to occupy a shallow energy landscape that enables facile exchange between

conformations.[93] Exchange between these conformations may then be regulated by the conformational specificity contained in other domains of the protein, such as the curvature-sensing amphipathic helices[41,42,87] or cytoplasmic tail residues involved in protein-protein interactions.[36–38,94]

## SUMMARY AND CONCLUSIONS

With the goal of characterizing concerted cholesterol-dependent conformational change in the C-terminal region of the M2 protein, we spin-labeled sites within the transmembrane domain, on both faces of the amphipathic helix, and in the distal cytoplasmic tail in bilayers with and without cholesterol. Line shape analysis and accessibility information reveal the existence of two amphipathic helix conformations that differ in mobility and membrane depth. Parallel studies on a scission-defective mutant revealed that the transmembrane and amphipathic helices exhibit altered conformational equilibria and exchange. Taken together, these experiments serve as strong evidence that the conformation more populated upon the addition of cholesterol is relevant for viral budding.

## SUPPORTING INFORMATION

The Supporting Information for Chapter 4 is located in Chapter S2.

## CHAPTER 4 CONTRIBUTIONS

Alice Herneisen ‘17 designed experiments pertaining to the pentaAla mutant and corresponding M2 sites, i.e. M2 sites 43 and 57. This includes generating the pentaAla plasmid, purifying, spin labeling, and reconstituting the protein, and data collection and interpretation. In addition, Alice Herneisen reconstituted M2 sites 60, 64, and 68 into

cholesterol and collected all of the corresponding accessibility data. The motivation for investigating cholesterol-dependent conformational change in the M2 protein was based on previous work using a truncated M2 construct (M2TMC, residues 23-60) carried out by Shawn Kim '14 and Mary Alice Upshur '12. Shenstone Huang '16 and Bryan Green '16 provided CW and power saturation data of M2 sites 51, 55, and 59 in 4:1 POPC:POPG bilayers. Stuart Arbuckle '17 provided CW and power saturation data of M2 sites 51 and 59 in 56:14:30 POPC:POPG:Cholesterol bilayers and performed spectral simulation of M2 and pentaAla sites 43 and 57 in the membranes studied here. Hayley Raymond '18 provided CW and power saturation data of M2 F55R1 in 56:14:30 POPC:POPG:Cholesterol bilayers. Grace Kim '17 provided spin labeled M2 K60R1 protein. Dr. Jimmy Feix (National Biomedical Electron Paramagnetic Resonance Center at the Medical College of Wisconsin) performed saturation recovery data collection and analysis. Alice Herneisen prepared proteoliposomes for circular dichroism and Dr. Kathleen Howard (Swarthmore College, Swarthmore, PA) collected spectra.

# Chapter 5: Curvature-Dependent Conformational Exchange of the Full-Length Influenza A M2 Protein and a Mutant Exhibiting Impaired Viral Scission

## INTRODUCTION

Dynamic membrane remodeling is a functional requirement for cell movement, division, communication, and vesicle trafficking.[24] The proper generation and stabilization of specific types of membrane curvature is also necessary for pathological events, such as virus entry and budding.[95,96] Membrane remodeling involves a complex interplay between lipids and proteins.[24] Membrane proteins have been hypothesized to deform the phospholipid bilayer through several mechanisms, including scaffolding, crowding, and insertion of amphipathic helices into the membrane interior.[24]

The mechanisms by which amphipathic helices remodel membrane curvature have been a topic of intense recent study.[85,97,98] The focus of this study is the amphipathic helix of the influenza A M2 protein, which is necessary and sufficient to induce scission *in vitro*[11,42] and *in vivo*.[12,40] The M2 protein is a 97-amino acid multifunctional, homotetrameric membrane protein composed of an extracellular N-terminal domain, a helical transmembrane domain with ion channel activity, and a C-terminal cytoplasmic tail.[10] The first ten residues (50-60) of the cytoplasmic tail form a juxtamembrane amphipathic helix.[17–19]

As a part of the broader work to characterize the structural plasticity of the M2 protein[19,33,61,99,100], and hence identify new drug targets, we have demonstrated that the amphipathic helices change their conformation and dynamics in response to changes in pH[17], the membrane environment[20,23], and the presence of adamantine drugs.[21] The M2

protein and amphipathic helix peptide have been observed to localize to regions of high membrane curvature[42,87,101], such as at the neck of a budding virus.[11,12,40]

Unlike many other protein domains studied in the context of this membrane-remodeling activity[102,103], the M2 amphipathic helix is tethered to a transmembrane domain that completely spans the bilayer. It has been proposed that the M2 protein possesses distinct membrane-remodeling domains that act synergistically to regulate proper viral budding.[41,104] However, how these domains may work in concert to promote viral egress is not understood.

Recent small-angle X-ray scattering (SAXS) studies have demonstrated that the M2 protein can generate scission-relevant negative Gaussian curvature (NGC) over a range of lipid compositions.[41] Mutations that disrupted the hydrophobic face of the amphipathic helix decreased the ability of the M2 protein to generate NGC over the range of lipid compositions studied, demonstrating that the curvature-remodeling capacity of the M2 protein is encoded in this short stretch of amino acids.[41] While this study provided important insight into the structural requirements for scission in terms of membrane phase, which depends on both the intrinsic curvature propensities of lipids and the shape of membrane-associated protein domains, an atomic-level understanding of M2 conformational changes associated with membrane remodeling is lacking.

Here, we use site-directed spin labeling (SDSL) in conjunction with electron paramagnetic resonance (EPR) to measure site-specific conformational changes in the full-length M2 protein. We investigate structural dynamics of two sites reporting on the M2 transmembrane and amphipathic helices. In addition, we characterized the conformational dynamics of the corresponding sites in a mutant that exhibits an

attenuated ability to generate negative Gaussian curvature. Both the amphipathic and transmembrane helices appear to populate two conformations, as determined by spectral simulation and saturation recovery EPR. The amphipathic helix site investigated here does not undergo detectable membrane phase-dependent conformational exchange. In contrast, the C-terminal transmembrane domain appears to undergo conformational exchange dependent on membrane phase and the presence of cholesterol. The pentaAla mutant exhibits an altered conformational equilibrium relative to the wild-type protein, suggesting that conformational equilibrium and exchange are necessary for the wild-type protein to remodel membrane curvature.

## MATERIALS AND METHODS

Detailed methods are provided in Chapter S3.

### Spin labeling strategy.

Site-directed spin labeling involves attaching a nitroxide radical side chain, called R1, to a unique recombinant cysteine.[43,71] For this study, two labeling sites were selected to report on the conformational dynamics of two domains in the M2 protein (Figure 5.1A): the C-terminal end of the transmembrane helix (L43) and the amphipathic helix (H57). Neither of these residues is highly conserved[74], suggesting that the protein fold will tolerate spin label attachment at these sites. We also generated a penta-alanine (pentaAla) mutant containing five alanine substitutions to large, hydrophobic amino acids lining the membrane-exposed face of the amphipathic helix (Figure 5.1B and C). The amphipathic helix site H57R1 is solvent-exposed in the wild-type structure[18,19] and was selected over other sites to minimize further disruptions to the hydrophobic face of the

helix. Expression, purification, and spin labeling of M2 and pentaAla cysteine variants have been described previously (Chapter 4).

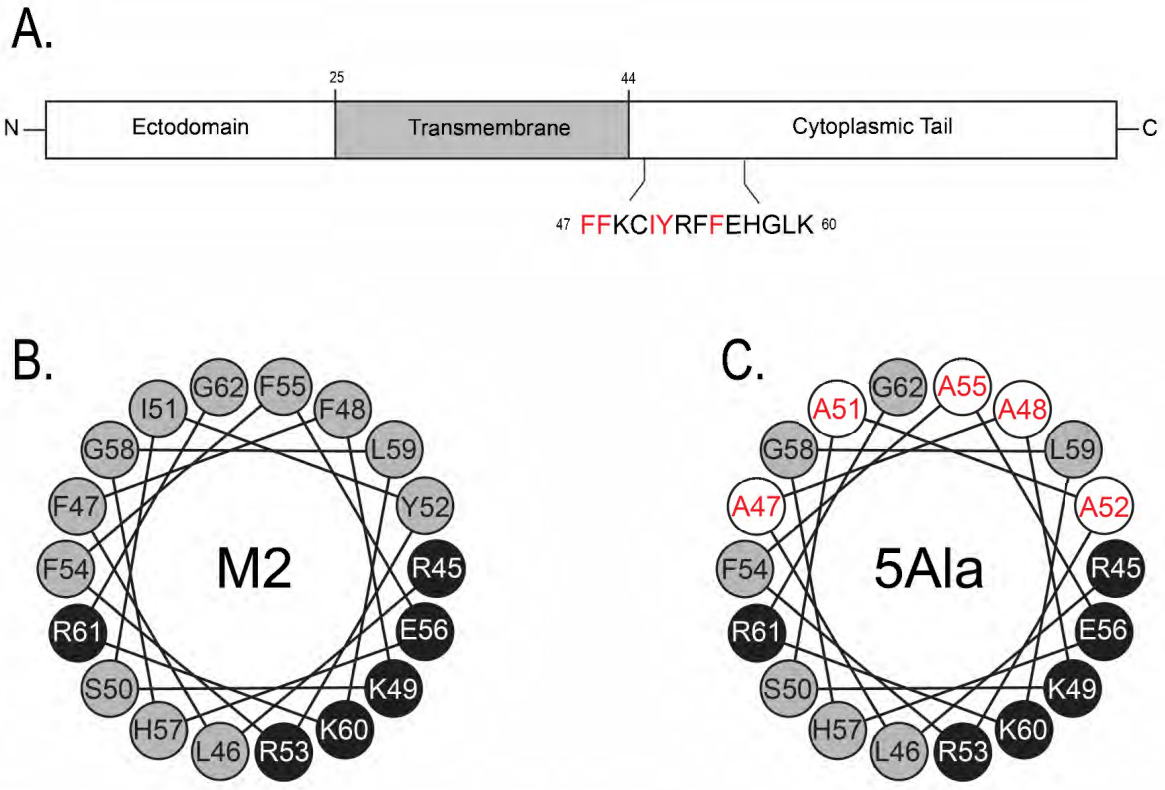


**Figure 5.1. Constructs investigated in this study.**
(A) Domain structure of the full-length M2 construct used in these studies. The amphipathic helix sites 47-60 are shown. Amino acids highlight in red were mutated to alanine in the PentaAla mutant. A helical wheel representation of the amphipathic helix of (B) wild-type M2 and (C) pentaAla.

### Lipid Sample Strategy and Preparation.

Proteoliposome sample preparation was based on previously published protocols ([18] and Chapter 4), with the following modifications. Purified M2 protein was reconstituted into 80/20 DOPC/DOPS and 80/20 DOPE/DOPS lipid samples at a 1:40 protein to lipid ratio. DOPE is a negative intrinsic-curvature lipid due to its small size of the polar head group relative to the cross-sectional area of the acyl chains.[24] This lipid

composition and protein:lipid ratio were chosen to corresponded to the region of a phase diagram generated by Schmidt et al.[41] in which only a single membrane phase existed. At a 80/20 DOPC/DOPS, 1:40 M2:lipid ratio, pure lamellar phase was detected. At a 80/20 DOPE/DOPS, 1:40 M2:lipid ratio, pure cubic phase was detected. Cubic phases are enriched in NGC. We hypothesize that these two different phases stabilize different curvature-dependent M2 conformations. In addition, to measure the effect of cholesterol on M2 conformational equilibrium, we prepared DOPC/DOPS and DOPE/DOPS proteoliposomes containing 30 mol % cholesterol. No phase diagrams currently exist for these protein and lipid compositions.

### EPR Continuous Wave and Power Saturation Measurements.

EPR data collection has been described previously (Chapter 3). Nitrogen power saturation experiments were collected over eight power levels. All other power saturation experiments were measured over 19 power levels. To minimize the effects of dipolar broadening, samples were spin-diluted by adding cysteineless full-length M2 and pentaAla constructs at an unlabeled:labeled 3:1 ratio.

## RESULTS

### M2 and PentaAla Mutant Amphipathic Helix Dynamics.

We collected information about the mobility and conformational equilibrium of residues reporting on the amphipathic helix (H57R1) and transmembrane (L43R1) domains. Continuous wave EPR spectra of these sitse in the wild type and pentaAla mutant in DOPC/DOPS and DOPE/DOPS membranes are shown in Figures 5.2 and 5.3.

The spectrum of wild-type M2 H57R1 clearly reveals a two-component nature in both DOPC/DOPS and DOPE/DOPS membranes (Figure 5.2). Each of the two components corresponds to a different degree of mobility of the nitroxide side chain.[105] The more immobile (i) and more mobile (m) components of the low-field peak are highlighted in darker and lighter shades of gray, respectively. For this site on the amphipathic helix, the relative intensity of the two components is not appreciably different whether the labeled protein is reconstituted into 80/20 DOPC/DOPS or DOPE/DOPS membranes.

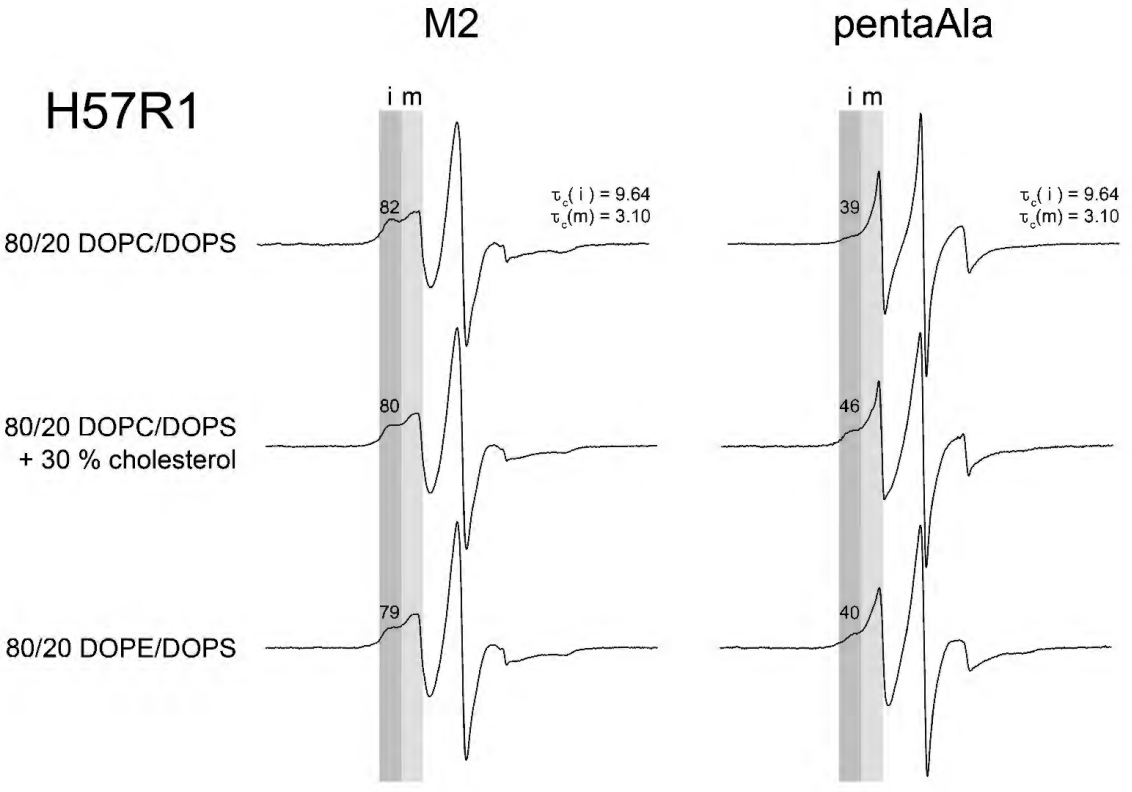


**Figure 5.2. Continuous wave X-band EPR dilute-labeled spectra of M2 and pentaAla H57R1 in the designated membrane environments.**
The light gray (m) and dark gray (i) boxes highlight the low-field mobile and immobile components, respectively. Correlation times in ns for each site are located on the right side of the topmost spectrum. The relative population of the immobile component is indicated above each low-field peak.

The relative mobility parameter and spectral simulation can provide qualitative and quantitative insights into the dynamic properties of the R1 side chain. The inverse central line width ($\Delta H_0^{-1}$) of an EPR spectrum serves as a semi-empirical mobility parameter that reflects spin label dynamics.[43,44] The inverse central line widths of for each R1 labeling site of the wild type and mutant protein in every membrane system studied here are shown in Figure 5.5A. The mobility parameter of M2 H57R1 in DOPC/DOPS and DOPE/DOPS membranes is not different within error.

Because $\Delta H_0^{-1}$ can be biased towards the more mobile spectral component[51,70], spectral simulation provides important complementary insight into the rotational modes of the R1 side chain.[48] Consistent with the observation of a two-component spectral line shape, simulation of the M2 H57R1 spectra required two motional components in order to achieve a reasonable fit (Figure S1). The correlation times of the mobile and immobile components are indicated on the right side of the corresponding spectrum in Figure 5.2. The relative population of the immobile component is indicated above the low-field peak. As expected based on the similarities of the R1 line shapes in the different lipid compositions, fits of the DOPC/DOPS and DOPE/DOPS data yielded nearly identical parameters (Table S3.1), indicating that the rotational modes of the amphipathic helix R1 side chain are similar in both lipid environments.

In order to gain insight about the conformational properties that are required for membrane remodeling, we performed line shape and mobility analysis on the same amphipathic helix site in the scission-defective pentaAla mutant protein.[11] A side-by-side comparison of the line shapes and mobilities of the M2 and pentaAla H57R1 sites in different lipid compositions are shown in Figures 5.2 and 5.5A, respectively. Strikingly,

under all lipid conditions, the pentaAla R1 spectrum exhibits a mobile peak with a much higher relative intensity than the corresponding M2 amphipathic helix site. In accordance with this observation, the relative mobility of the pentaAla site is much higher than the corresponding site in M2 (Figure 5.2A). Remarkably, simulations of the pentaAla H57R1 spectrum produced fits with nearly identical parameters to those exhibited by the wild type protein (Figure S1; Table S3.2). The main differences arise from the relative populations of the mobile component under each condition: while the wild type site has a relative immobile population of ~80% under all lipid conditions, the pentaAla site only has an immobile population of ~40%.

Whether the two motional components arise from two rotameric states of the R1 side chain or two conformational states of this region of the protein is currently being investigated with saturation recovery EPR experiments. Preliminary evidence suggests that wild-type M2 site 57 exchanges between two conformations with different accessibilities to paramagnetic relaxation agents in DOPE/DOPS bilayers (Jimmy Feix, personal communication). Furthermore, ongoing work in our group suggests that the two-component nature of the wild type M2 amphipathic helix spectra is not isolated to a specific site, but rather exists along the full length of the helix.[54]

**M2 and PentaAla Mutant C-Terminal Transmembrane Helix Dynamics.**

In order to characterize the dynamics and conformational equilibrium of the C-terminal transmembrane domain, we performed similar line shape, mobility, and simulation analysis on M2 and pentaAla site 43. Continuous wave EPR spectra of these sites in the wild type and pentaAla mutant in DOPC/DOPS and DOPE/DOPS membranes

are shown in Figure 5.3. Like the spectrum of the corresponding site in the amphipathic helix, the M2 L43R1 line shape exhibits a two-component nature in all membranes investigated. Increasing the DOPE content of the membrane results in an increase in the intensity of the low field immobile peak. This shift corresponds to a decrease in the $\Delta H_0^{-1}$ (Figure 5.5A), suggesting that spin label mobility at this site is lower when M2 is in DOPE/DOPS membranes. Spectral simulation yields correlation times for the fast and slow motional components that are slower than the corresponding components in the amphipathic helix site, consistent with more restriction in the rotational motion of the spin label due to the membrane-exposed nature of this site (Figure S1; Tables S3.3 and S3.4). Unlike the spin label on the amphipathic helix site, the relative populations immobile component of the transmembrane site increase as the DOPE content of the membrane increases, indicating that the presence of lipids with negative intrinsic curvature shifts conformational equilibrium towards the more immobile conformation.

The pentaAla line shapes reveal two prominent differences. A side-by-side comparison of the line shapes and mobilities of the M2 and pentaAla L43R1 sites in different lipid compositions are shown in Figures 5.2 and 5.5A, respectively. First, the relative weight of the immobile component for the mutant site 43 is higher in DOPC/DOPS membranes than in the corresponding M2 site. Consistent with these observations, spectral simulations for M2 L43 and pentaAla L43 in DOPC/DOPS membranes yielded a relative population of the immobile component of 54 and 89%, respectively. The intensity of the pentaAla L43R1 immobile peak does not appear to vary significantly with the presence of negative intrinsic curvature DOPE lipids.

Simulations of the DOPC/DOPS and DOPE/DOPS L43R1 spectral line shapes produced a relative population of the immobile component of 88 and 89%, respectively. Notably, the correlation times of the pentaAla transmembrane site were slightly higher than those for the corresponding M2 site. Taken together, these observations suggest that the pentaAla mutant exhibits altered conformational equilibria and conformational exchange properties.

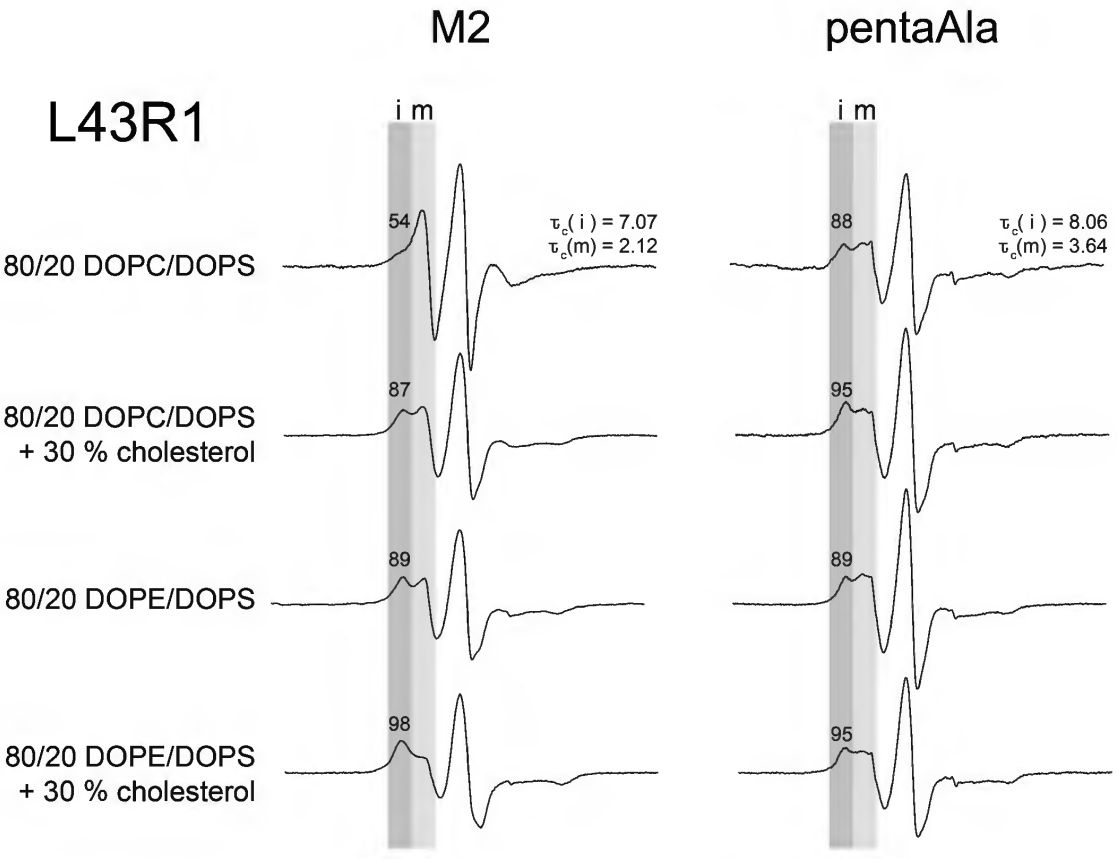


**Figure 5.3. Continuous wave X-band EPR dilute-labeled spectra of M2 and pentaAla L43R1 in the designated membrane environments.**
The light gray (m) and dark gray (i) boxes highlight the low-field mobile and immobile components, respectively. Correlation times in nanoseconds for each site are indicated on the right side of the topmost spectrum. The relative population of the immobile component is indicated above each low-field peak.

**Saturation Recovery EPR Indicates that Two Conformations Exist in the M2 and PentaAla Amphipathic Helix.**

To verify that the multi-component line shapes observed in the M2 and pentaAla amphipathic helix arise from conformational equilibrium rather than two rotameric states of the spin label, we performed saturation recovery EPR[47] on H57R1 samples reconstituted into DOPC/DOPS and DOPE/DOPS membranes (Figure 5.4A-D). Saturation recovery curves for M2 and pentaAla H57R1 in both membrane systems are best fit by double-exponential recoveries, consistent with conformational exchange at this site. Furthermore, the spin-lattice relaxation times for this site too slow for rotameric exchange (Table S3.5).

Saturation recovery results revealed that the two components exhibited different accessibilities to the paramagnetic relaxation agent $O_2$. In each case, the spin-lattice relaxation rate of the faster component (Figure 5.4 inset, red) is more dependent on the concentration of oxygen than the slower component (Figure 5.4 inset, blue). Because oxygen preferentially partitions into the membrane interior, this observation is consistent with the more mobile conformation being more deeply buried in the membrane than the immobile conformation.

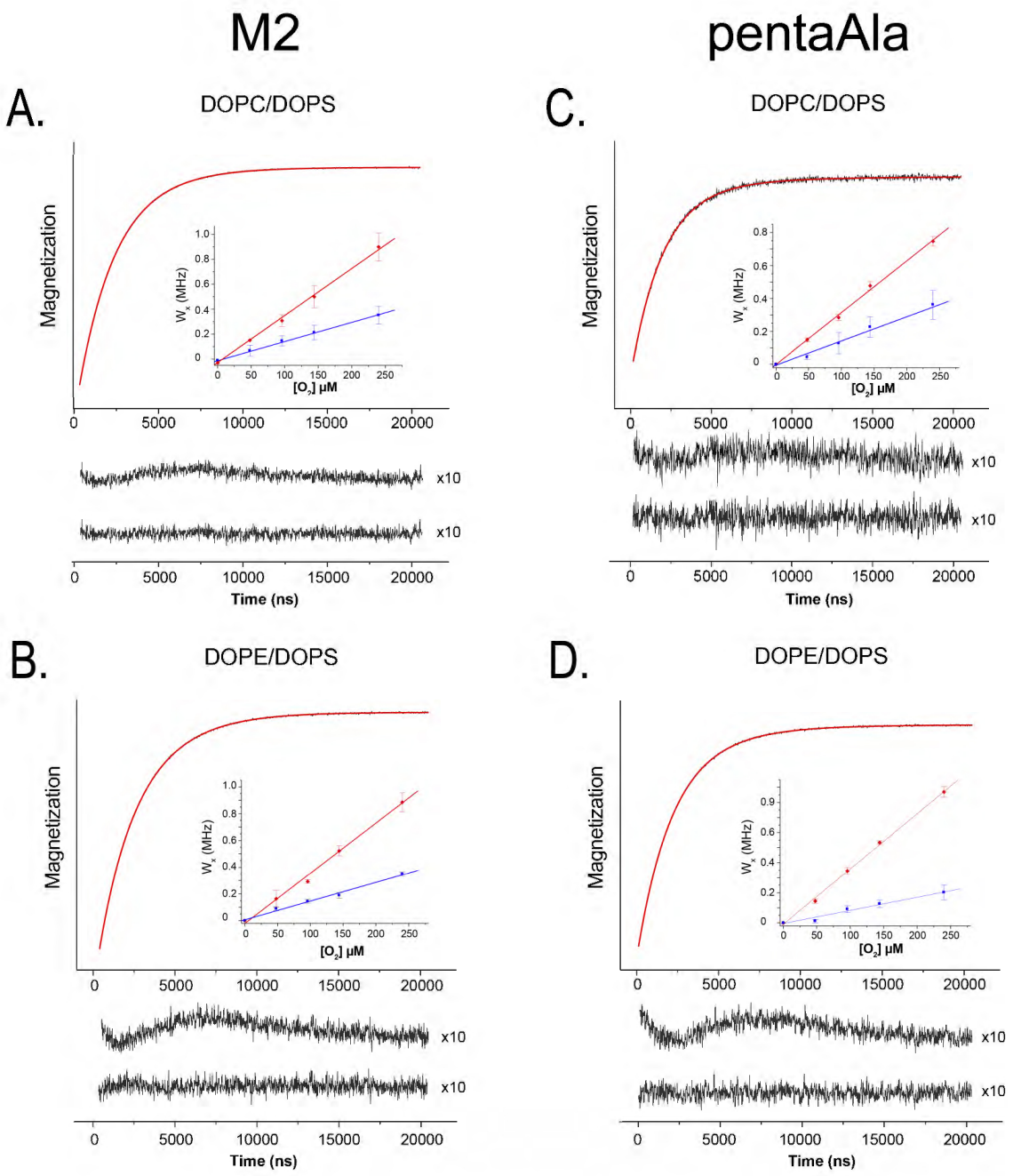


**Figure 5.4. Saturation recovery data indicate two components in conformational exchange in the M2 and pentaAla amphipathic helix in DOPC/DOPS and DOPE/DOPS membranes.**
Recovery curves for M2 H57R1 under 20% air in (A) DOPC/DOPS and (B) DOPE/DOPS membranes are best fit by a double-exponential. Recovery curves for pentaAla H57R1 under 20% air in (C) DOPC/DOPS and (D) DOPE/DOPS membranes are also best fit by a double-exponential. Residuals for single- (top) and double- (bottom) exponential fits are shown under each recovery curve. Insets show the dependence of the spin-lattice relaxation rates on oxygen for the mobile (red) and immobile (blue) components.

**The Influence of Cholesterol on Spectral Line Shapes and Dynamics.**

Previous work has demonstrated that the presence of cholesterol in the membrane can induce conformational exchange in the M2 protein ([20] and Chapter 4). Cholesterol, like DOPE, is a negative intrinsic curvature lipid.[106] In order to investigate the additive effects of cholesterol on M2 conformational equilibra in the ternary lipid system investigated here, we reconstituted the spin-labeled protein into membranes containing DOPC/DOPS and DOPE/DOPS membranes with 30% cholesterol. The CW EPR spectra of constructs in these membrane environments are shown along with the corresponding membranes without cholesterol in Figures 5.2 and 5.3.

The relative intensity of the immobile peak of the amphipathic helix site is similar in DOPC/DOPS membranes with and without cholesterol (Figure 5.2), suggesting that this region of the amphipathic helix does not undergo detectable cholesterol-dependent conformational exchange in this membrane system and at this peptide:lipid ratio. This observation holds for both the M2 and pentaAla H57R1 sites. Saturation recovery curves for M2 and pentaAla H57R1 in DOPC/DOPS membranes with 30% cholesterol are best fit by double-exponential recoveries, indicating that a conformational equilibrium continues to exist for this region. Furthermore, the spin-lattice relaxation rate of the slower component is less dependent on oxygen (Table S3.5), consistent with the slower state being less deep in the membrane.

In contrast to the lack of cholesterol-dependent conformational exchange observed for the amphipathic helix site, the relative intensity of the immobile peak of the transmembrane site increases with the addition of cholesterol to DOPC/DOPS membranes (Figure 5.3). In the wild type M2 construct, the relative population of the

immobile component in DOPC/DOPS/cholesterol membranes is 87%, which is similar to the relative population of the immobile component in DOPE/DOPS membranes. Furthermore, the correlation times produced from simulations of the protein reconstituted into DOPE/DOPS and DOPC/DOPS/cholesterol membranes are similar, suggesting that the rotational motion of the spin label, and hence the surrounding chemical environment, is similar in both lipid environments. Furthermore, the population of the immobile component of site 43 in DOPE/DOPS/cholesterol membranes is higher than the population of the immobile component when the protein is reconstituted into DOPE/DOPS membranes (98% vs. 89%, respectively)

While the pentaAla L43 site does not appear to undergo conformational exchange dependent on the amount of DOPE in the membrane, small differences exist in the relative populations of immobile component in DOPC/DOPS and DOPE/DOPS membranes with and without cholesterol. This observation may indicate that the C-terminal transmembrane domain undergoes a cholesterol-dependent shift in conformational equilibrium that operates independently of (in the case of the pentaAla mutant) or synergistically with (in the case of the wild type protein) the membrane phase-dependent conformational exchange.

However, we hesitate to over-interpret this observation, or attribute to it physiological significance. The phase diagrams corresponding to membranes of this lipid, cholesterol, and protein composition are unknown. At such high peptide:lipid:cholesterol ratios, cholesterol may precipitate into crystalline domains[107], or the protein may aggregate. Furthermore, the errors associated with the simulations are presently

unknown, and the small differences in the relative populations of the immobile components may not be significant.

### Localization of the C-Terminal Domain Relative to the Membrane Interior.

The oxygen accessibilities of both M2 and pentaAla sites in all membrane compositions investigated here are shown in Figure 5.5B. The accessibility profiles do not present any immediately discernable trends. The oxygen accessibility of L43R1 in the wild type protein is lower in DOPC/DOPS membranes than DOPE/DOPS membranes. For the same M2 site, the oxygen accessibility decreases significantly when cholesterol is added to the membrane. The corresponding site in the pentaAla construct has higher oxygen accessibility in all membrane environments, but the oxygen accessibility does not significantly vary as the DOPE or cholesterol content of the membrane is changed.

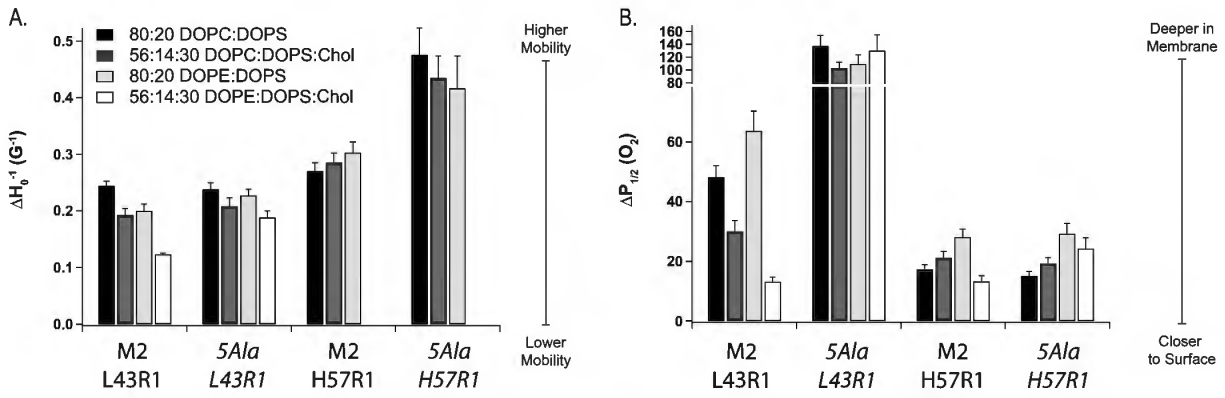


**Figure 5.5. Mobility and accessibility profiles of the M2 and pentaAla sites investigated in this study.**
(A) The inverse central line width (relative mobility) of the indicated M2 and pentaAla sites obtained from the dilite-labeled spectra of spin labeled protein reconstituted into membranes with the indicated lipid composition. (B) The oxygen accessibility of each site. Error bars represent the 95% confidence interval.

In general, the oxygen accessibility of site 57 is lower than site 43 in both the M2 and pentaAla constructs, consistent with this site being less deeply buried in the membrane. The oxygen accessibility of H57R1 does not vary greatly depending on the lipid environment. Furthermore, the accessibilities of the amphipathic helix sites are remarkably similar in both the M2 and pentaAla constructs.

The oxygen accessibilities present challenges in interpretation for several reasons. At such high protein to lipid ratios, the apparent oxygen accessibility of a given site may reflect protein-protein interactions in addition to depth in the membrane.[71] Furthermore, when conformational exchange gives rise to a two-component spectrum, as is suspected here, accessibility data will be biased towards the component with the highest accessibility to a given paramagnetic relaxation agent.

### Circular Dichroism to Assess M2 and PentaAla Global Secondary Structure.

In order to determine if the penta-alanine mutations and corresponding altered conformational equilibria arise from a loss of secondary structure in the C-terminal region, we recorded circular dichroism spectra of cysteineless M2 and pentaAla protein in DOPC/DOPS and DOPE/DOPS proteoliposomes (Figure S3.3). Due to the preliminary nature of these results, a brief interpretation of the findings is provided in the Chapter S3 Supporting Discussion.

## DISCUSSION

Data from line shape analysis and spectral simulation suggest that the transmembrane and amphipathic helix regions of the M2 protein exist in conformational equilibrium and undergo concerted conformational exchange in response to the curvature

properties of the membrane. The conformation that is more highly populated in the presence of DOPE and cholesterol, both of which have negative intrinsic curvature[108], is less dynamic than the other conformation. The pentaAla mutant differs from the wild-type protein in two important ways. First, the conformational equilibrium of the pentaAla amphipathic helix site differs significantly from the corresponding equilibrium in M2. In the pentaAla mutant, the mobile component dominates the spectral line shape. Second, the penta-alanine mutations in the amphipathic helices abolish detectable conformational exchange in the C-terminal transmembrane site. It is possible that this site undergoes conformational exchange between two slow-motion regimes; however, the oxygen accessibility information is consistent with a lack of conformational exchange that results in a change in helix membrane depth, as observed in the wild-type protein.

It has been proposed that influenza virus scission requires a minimum threshold of induced membrane NGC.[41] Evidence for this theory comes from the observation that the penta-alanine mutant can still generate cubic phases enriched in NGC, but over a reduced range of lipid compositions compared to the wild-type protein.[41] We find that the M2 conformational exchange observed here maps remarkably well to this activity profile. The correlation times and parameters obtained from fits of the M2 and pentaAla amphipathic helix sites suggest that the microenvironments surrounding the spin labels are similar in both constructs and both conformations. The essential difference between these constructs, then, is the equilibrium between the two conformations. We hypothesize that the attenuated ability of pentaAla to generate NGC results from the reduction in the population of mutant in the immobile, curvature-relevant conformation relative to the wild-type protein.

## CHAPTER 5 CONTRIBUTIONS

The work presented in this chapter represents only part of ongoing efforts in our lab to characterize the membrane-dependent, curvature-responsive conformational equilibrium of the M2 protein. The complexities of conformational exchange in this region cannot be captured in the two sites examined here, and the interested reader is directed to the thesis of D. Stuart Arbuckle '17.[54] Alice Herneisen '17 generated the pentaAla plasmid and purified and spin-labeled the pentaAla protein and corresponding wild-type M2 constructs. Alice Herneisen and Stuart Arbuckle reconstituted the protein and collected data. Stuart Arbuckle fit power saturation data for M2 L43R1. Alice Herneisen fit power saturation data for M2 H57R1 and pentaAla L43R1 and H57R1. Stuart Arbuckle simulated the M2 and pentaAla line shapes. Dr. Jimmy Feix (National Biomedical Electron Paramagnetic Resonance Center at the Medical College of Wisconsin) performed saturation recovery data collection and analysis. Dr. Kathleen Howard (Swarthmore College, Swarthmore, PA) prepared proteoliposomes CD samples and collected spectra.

## SUPPORTING INFORMATION

The Supporting Information for Chapter 5 is located in Chapter S3.

# Chapter 6: Future Directions

Research, I am told, does not have a neat ending point. In this Chapter, I summarize loose ends and propose directions for follow-up study. Some flow directly from the work presented in this thesis. Others are more exploratory. I hope all are within experimental reason.

## EXTENDING STRUCTURAL STUDIES OF THE INFLUENZA A M2 CYTOPLASMIC TAIL

### Closing the Loop on the Conformation(s) of Sites 61-70.

In Chapter 3, we showed that the region following the amphipathic is a part of a highly mobile unstructured segment under our model membrane conditions. These sites no longer exhibit the 3.6-periodicity in oxygen accessibilities characteristic of a helix; however, the oxygen accessibility profiles of sites 61-70 appear to sustain some periodic properties, suggesting that the region may continue along the membrane surface rather than making a sharp turn towards the aqueous phase to form an extended structure, as has commonly been depicted.[41,78] In some instances, however, an apparent helix periodicity can appear reach into the loop region.[51] In such cases, the contrast parameter $\Phi = \ln[\Delta P_{1/2}(O_2)/\Delta P_{1/2}(\text{NiEDDA})]$ can be used to locate the loop residues, as $\Phi$ varies little through loop regions.[51] Calculating the contrast parameter for sites 61-70 would require additional power saturation experiments in the presence of NiEDDA. However, such studies could provide reveal if sites 61-70 are unstructured or whether it truly exhibits residual periodic properties indicative of a partially ordered structure.

Additional insights into the conformational dynamics of this region might come from spectral simulation, which can provide the correlation times of the rotational modes

of a particular spin label side chain and, therefore, information about the asymmetry of the surrounding environment.[52] Notably, some residues in the post-amphipathic helix region exhibited line shapes with a two-component nature, e.g. sites 61, 64, 64, and 69. Spectral simulation has previously been used to reveal that an unstructured region of the SNARE protein synaptobrevin 2 was capable of transiently associating with the membrane interface in a curvature-dependent manner.[109] The cytoplasmic tail of the M2 protein could be investigated in a similar manner. Preliminary investigations of the dilute-labeled line shapes of distal cytoplasmic tail residues suggests that spin labels at these sites do not stably reside within 20 Å of each other; therefore dipolar broadening is unlikely, and pre-existing fully-labeled spectra of these sites can be simulated to extract correlation times.

In principle, each cysteine variant used for labeling studies should be assayed to demonstrate that mutation is not detrimental to structure or function. This presents challenges for sites 61-70, as the region is expendable for ion channel activity.[15,110] Furthermore, this protein segment contains several native residues with particular backbone (G62, P63, G67, P69) and electrostatic (E66, E70) properties that may differ markedly from those of the R1 side chain. Other EPR studies of highly dynamic, unstructured regions have used circular dichorism thermal unfolding studies to demonstrate that the R1 side chain does not significantly perturb protein stability.[111] The work done as a part of this thesis has laid the groundwork for CD studies of M2 cysteine variants in a variety of membrane systems. In the future, each cysteine construct can be assayed for thermal stability in conjunction with EPR studies. Additional circular dichroism studies will likely open up exiting new avenues beyond those performed as a

part of this thesis, e.g. by identifying global changes in M2 secondary structure in different membrane environments.

### Structural Studies of a Region of the M2 Protein Involved in Protein-Protein Interactions and Influenza Morphology.

Numerous studies have implicated the M2 cytoplasmic tail in viral assembly. In particular, the highly charged and conserved region between residues 71-80 plays an important role in proper viral morphology and genome packaging, as inferred through alanine substitutions and *in vivo* assays[35–38,58]. Furthermore, protein sequence analysis algorithms[64] predict that residues 70-80 are capable of forming an α-helix. Despite the functional importance of these residues, biophysical information about this region of the protein is extremely limited.

A recent solid-state NMR study of the full-length M2 protein attempted to assign chemical shifts to the region spanning residues 70-80 via spectral simulation, as resonances could not be definitively assigned.[34] Of the several secondary structure models generated to account for the chemical shifts included in 2D DARR and J-INADEQUATE spectra, one included an α-helical segment between residues 70-80. The final secondary structural model contained a purely coiled post-amphipathic helix cytoplasmic tail; however the structure with a helical segment between residues 70-80 provided a similar fit and was in better accord with the % helicity of VM+ bound M2 as determined by circular dichroism.[34]

The ambiguities of previous studies underscore the necessity for additional site-specific structural investigation of the distal cytoplasmic tail. One complication arises from the presence of a C-terminal hexahistidine tag on the constructs used in this thesis.

Previous SDSL-EPR studies have indicated that His-tags in the vicinity of spin label probes can greatly influence spectral line shape and apparent backbone mobility.[112] Therefore, further investigation of the M2 cytoplasmic tail will require a new construct with a N-terminal His tag and cleavage site (Appendix B). As a part of the ill-fated early work of the present thesis, this construct was obtained and adapted for EPR studies, with single cysteine substitutions introduced at sites 71-80 (Appendix C). Especial care will be required to verify that R1 labeling does not perturb structural elements required for M1-M2 interactions.

## CHARACTERIZING THE CONFORMATIONS OF THE PENTA-ALANINE MUTANT

### Next Steps in Unraveling PentaAla: Distance Information.

Detecting and interpreting cholesterol-dependent and curvature-dependent conformational exchange in the full-length protein was greatly facilitated by the efforts of previous Howard lab members, who took a multi-pronged approach to characterize the accessibility profiles of the two conformations and features of the packing of the homotetramer that differed between states.[20,82,84] Characterizing the conformational states of the pentaAla mutant, however, presents challenges. It is tempting to speculate that the mutant populates the same two conformations as M2 investigated in previous studies; however, we require additional evidence. Accessibility to paramagnetic reagents such as oxygen, NiEDDA, and the Nickel-chelate lipid used in this study provides only relative depth information under our experimental conditions. Our analysis would greatly benefit from distance information, such as the information provided by pulsed EPR techniques like double electron-electron resonance (DEER)[46], for the reasons discussed below.

*1. Assessing packing within the homotetramer.*

DEER experiments can resolve distance distributions longer than the 20 Å limit detectable from CW-EPR dipolar broadening.[46] DEER experiments conducted on the wild-type and penta-Ala construct could reveal if the two constructs exhibit different distance distributions and, therefore, different conformations. A distance distribution with larger separations between spin labels would be consistent with less tight packing of the tetrameric bundle. The transmembrane site investigated as a part of these studies is a poor candidate for DEER, as it exhibits significant dipolar broadening in both the M2 and pentaAla constructs, indicating that the spin labels reside stably within 20 Å. However, the amphipathic helix site appears to exhibit minimal dipolar broadening and is ideally poised for pulsed EPR techniques.

*2. Identifying conformational equilibrium through distance distributions.*

DEER experiments can also be used to identify differing conformational dynamics between the penta-Ala and wild-type construct. Homotetrameric membrane proteins like M2 are expected to possess two inter-subunit distances resulting from proximal and diagonal interactions between spin labels on different subunits. DEER experiments indicate that spin-labeled sites in the amphipathic helix give rise to four distance distributions, consistent with two distinct conformations of the homotetramer.[20] If the penta-Ala construct has lost its ability to populate the scission-relevant conformation, then DEER distance distributions may only provide one set of proximal and diagonal distances.

In preparation for collecting distance information using EPR techniques, an additional pentaAla amphipathic helix cysteine mutant, L59C, has been generated and transformed into the appropriate cells (Appendix C). In contrast to the H57 site, the L59 site is located on the hydrophobic face of the amphipathic helix. Comparing the accessibility profiles of M2 and pentaAla L59R1 may therefore provide more insight about the location of the pentaAla amphipathic helix with respect to the membrane.

### Assessing the Dynamic Properties of the diAla and triAla Mutants.

Virological studies have demonstrated that double alanine substitutions to any of the five sites mutated in the pentaAla construct are sufficient to abolish viral filament formation and result in virus particles with the scission-defective beads-on-a-string morphology.[40] However, single-alanine substitutions fail to produce the defective morphology.[12,40] These observations suggest that the ability of the amphipathic helix to mediate viral morphology relies on the physicochemical properties of the entire helix, such as hydrophobicity or hydrophobic moment[85], rather than the properties of a particular residue. In comparison to the wild-type M2 amphipathic helix (residues 45-62), the pentaAla amphipathic helix has a markedly reduced hydrophobicity and hydrophobic moment (Figure 1). Several studies have employed these physicochemical parameters to rationalize the interaction of amphipathic helices with the membrane[42,79,98,113]; however, these studies have almost exclusively focused on cytosolic proteins capable of peripheral and transient membrane association.

The M2 amphipathic helix, in contrast, is partially anchored to the membrane by

virtue of the transmembrane domain. Although a significant proportion of transmembrane proteins also contain membrane-proximal amphipathic helices that occupy the interfacial region[114], the curvature-sensing and curvature-remodeling of such "anchored" juxtamembrane helices has not, to our knowledge, been extensively described.

As a part of this thesis, two additional alanine mutants were generated: the F47A, F48A ("diAla") and the I51A, Y52A, F55A ("triAla") mutants. These two mutants possess hydrophobicity and hydrophobic moment values that fall as intermediates between those of M2 and pentaAla (Figure 6.1). The loss of function of the F47A, F48A mutant has been characterized *in vivo*.[40] Site-specific structural studies of the diAla and triAla mutant similar to those performed in this thesis could provide insight into the importance of "membrane-anchored" amphipathic helix hydrophobicity and hydrophobic moment in regulating conformational dynamics and insertion depth in the membrane. The implications of such studies would likely extend beyond improving our understanding of the M2 protein and provide general insight into how these physicochemical properties regulate the membrane association of amphipathic helices attached to transmembrane domains.

| Construct | Additional Mutations | Hydrophobicity | Hydrophobic Moment |
|---|---|---|---|
| M2 | - | 0.519 | 0.474 |
| pentaAla | F47A, F48A, I51A, Y52A, F55A | 0.066 | 0.248 |
| diAla | F47A, F48A | 0.267 | 0.387 |
| triAla | I51A, Y52A, F55A | 0.230 | 0.350 |

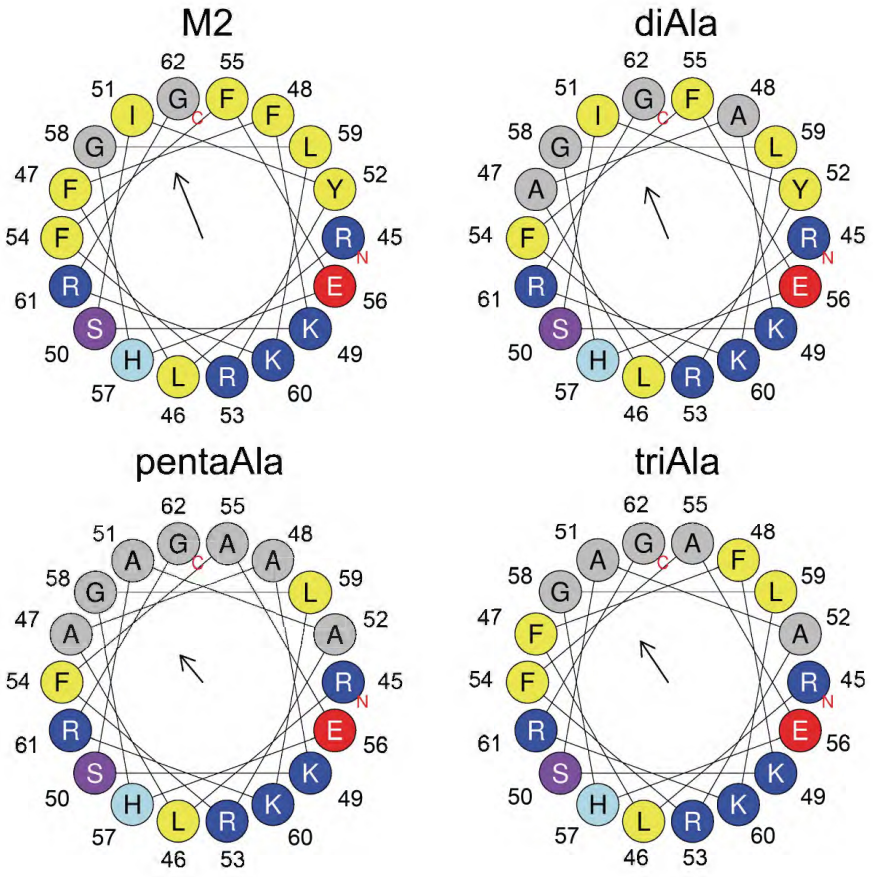


**Figure 6.1. Properties of the M2 and alanine mutant amphipathic helices.** Hydrophobic moment, hydrophobicity, and helical wheel diagrams were generated using HeliQuest.[115]

The F47A, F48A mutant may prove especially intriguing, as these residues have been proposed to form a flexible "hinge" connecting the transmembrane and amphipathic helices.[20] These residues, along with the amphipathic helices, occupy distinctly different environments in two published high-quality NMR structures of the M2 transmembrane and amphipathic helix domains. In the solid-state NMR structure solved in 1,2-dioleoyl-

sn-glycero-3-phosphochoine/1,2-dioleoyl-sn-glycero-3-phosphoethanolamine (DOPE/DOPC) bilayers (2L0J[19]), F47 and F48 constitute a tight 90° loop associated with the membrane. In contrast, in the solution-state NMR structure solved in dihexanoyl-sn-glycero-3-phosphocholine (DHPC) micelles (2RLF[100]), these residues form an extended loop that stretches away from the membrane. The conformation of the loop residues, therefore, may have important implications for the packing arrangements and membrane depth of the amphipathic helices.[20] The bulky, hydrophobic nature of the phenylalanine side chains could sensitize the "hinge" to the surrounding membrane environment, e.g. packing defects induced by cholesterol or cone-shaped lipids. Small alanine side chains may lack the ability to respond to membrane composition, and thus the loss in function of alanine mutants may specifically be explained by substitution to these two residues, as well as by alterations to the overall amphipathic helix hydrophobicity.

# Acknowledgements

First, as promised, I would like to thank Grace Kim ’17, who can commiserate with the dozens of hours that trickled by in experimental purgatory and the unglamorous gruntwork of generating constructs and performing purification after purification after purification, followed by reconstitution after reconstitution after reconstitution. I would like to thank Stuart Arbuckle ’17 for accommodating my questionable work habits and for discussions about M2 that went down the rabbit hole and back up again. I am grateful to Bryan Green ’16, who welcomed me into the lab and continued to help me even after his time here ended.

I wish Aaron Holmes ’18, Ben Hsiung ’18, Hayley Raymond ’18, and Abigail Wong-Rolle ’19 the best of luck in their future endeavors in the Howard lab.

And last, but the opposite of least, I would like to extend my greatest thanks to Kathleen Howard, who has supported me at every step, forward and backward, over the past year. Thank you.

# Chapter S1 Supporting Information for Chapter 3: Structural Features of the C-Terminal Domain of the Full-Length M2 Protein in Lipid Bilayers

## SUPPORTING MATERIALS AND METHODS.

### Materials.

Nickel-iminodiacetic acid (Ni-IDA) was purchased from Gold Biotechnology (Olivette, MO). The following lipid samples were purchased as a 25 mg/mL chloroform solution from Avanti Polar lipids (Alabaster, AL): 1-palmitoyl-2-oleoyl-sn-glycero-3-phosphocholine (POPC), 1-palmitoyl-2-oleoyl-sn-glycero-3-phospho-(1'-rac-glycerol) (POPG), and 1,2-dioleoyl-sn-glycero-3-[(N-(5-amino-1-carboxypentyl)iminodiacetic acid)succinyl] nickel salt (DOGS-NTA[Ni(II)]). (*S*-(1-oxyl-2,2,5,5-tetramethyl-2,5-dihydro-1H-pyrrol-3-yl)methyl methanesulfonothioate) (MTSL) spin label was purchased from Toronto Research Chemicals (North York, Canada). Proteoliposome samples were concentrated using a Beckman Coulter Optima Max-XL Ultracentrifuge (Pasadena, CA).

### Reconstitution of Full-Length M2 Protein into Lipid Bilayers.

Reconstitution protocols are based on previously published work.[17,18,21] Lipid films were prepared by combining 25 mg/mL chloroform POPC and POPG solutions in a 4:1 molar ratio. Each film contained 6.6 x $10^{-6}$ moles of lipid. The chloroform mixtures were dried under a gently stream of nitrogen gas and were lyophilized overnight to remove residual chloroform. Films were stored at -20°C.

Lipid films were rehydrated in 534 µL extruder buffer (50 mM Tris pH 7.8, 100 mM KCl, 1 mM EDTA) to a final lipid concentration of 9.36 mg/mL. The lipid

suspensions were resuspended by alternatively vortexing and bath sonicating the rehydrated films.

An Avanti Mini Extruder with 20 μm polycarbonate filters was equilibrated with extruder buffer to fill ~50 μL of extruder void space. The resuspended lipid films were extruded 15 times. A solution of 25 mg/mL OG was added to the extruded lipids to raise the detergent concentration (typically 30-35 mM) above the critical micelle concentration of 20-25 mM. The lipid/detergent solution equilibrated for 30 minutes.

The concentration of purified, OG-solubilized M2 protein was determined from the A280 and an extinction coefficient of 8480 $M^{-1}cm^{-1}$ (Appendix C). Protein was added to the lipid/detergent solution to achieve a 1:500 protein:lipid molar ratio.

A slurry of hydrophobic polystyrene beads (BioBeads) was hydrated dropwise by 50 mM Tris pH 8, 40 mM OG buffer. The BioBead equilibration buffer was subsequently changed to 50 mM Tris pH 7.8, 100 mM KCl, 1 mM EDTA. The BioBead slurry was stirred and degassed for one hour. The dilute proteoliposomes were nutated at 4°C while approximately 50 $\mu$L of the BioBead slurry was added to the proteoliposomes in 15 minute intervals until the total volume of BioBeads was 300 $\mu$L. The proteoliposome solution was concentrated by two rounds of ultracentrifugation at 90,000 rpm for 60 minutes at 4°C. The samples were frozen at -20°C and thawed prior to data collection.

For NiEDDA sample preparation, 50 mM NiEDDA, 50 mM Tris pH 8, 100 mM KCl buffer was used instead of extruder buffer. For nickel-chelate lipid sample preparation, 50 mM Tris pH 8, 100 mM KCl buffer was used instead of extruder buffer.

**Circular Dichroism Sample Preparation.**

For each sample, 3.3 x $10^{-6}$ moles of 4:1 POPC:POPG lipid films were rehydrated to 9.36 mg/mL in extruder buffer. Cysteineless and H57R1 M2 protein was reconstituted into the lipids in a 1:500 protein:lipid ratio as described above, with the exception that samples were not concentrated via ultracentrifugation. Instead, the dilute proteoliposome samples were treated according to the procedure described below. A liposome sample was prepared using the same lipid composition and sample preparation protocol.

To minimize solvent absorption, proteoliposome solutions were diluted with Millipore water by a factor of 2.5 to a final concentration of 20 mM Tris pH 7.8, 40 mM KCl. Diluted samples were concentrated by centrifugation with a 10K MWCO Amicon to a final protein concentration of appeoximately 0.5 mg/mL as estimated from the A280 and an extinction coefficient of 8480 $M^{-1}cm^{-1}$. The actual protein concentration of proteoliposome samples was measured using the $A_{280}$ on a Nanodrop spectrometer using a 50% dilution of an aliquot of the proteoliposome sample in 10% sodium dodecyl sulfide (SDS) to correct for solvent flattening.

CD spectra were collected on an Aviv Model 435 Circular Dichroism spectrometer at 25°C. A 35 $\mu$L aliquot of sample was loaded into 0.011 cm path length demountable quartz cuvette. Spectra were collected from 280 nm to 190 nm with a 1 nm step size. The averaging time at each point was 5 seconds, and the bandwidth was 2 mm. Three scans were collected and averaged. Spectral data collected directly from the instrument were converted from units of millidegrees to per residue molar absorption units (also known as molar circular dichroism, $\Delta\varepsilon$, in units of $M^{-1}cm^{-1}$) using the following equation:

$$\Delta\varepsilon = \theta * \frac{0.1 * MRW}{(P * CONC) * 3298} \quad (1)$$

where $\theta$ is spectral intensity data in millidegrees, P is the path length of the cuvette in cm, CONC is the protein concentration corrected for solvent flattening in units of mg/mL, and MRW (amu) is the mean residue weight defined as

$$MRW = \frac{protein\ MW}{number\ of\ residues} \quad (2)$$

A table of physical parameters corresponding to the M2 constructs used here is provided in Appendix C. The baseline scattering pattern produced by the liposome samples was subtracted from the proteoliposome CD signal.

## CHAPTER S3 SUPPORTING FIGURES AND TABLES.

**Figure S3.1. A representative M2 cysteine construct purification gel.**
The purity of M2 cysteine constructs was assessed at each stage in the purification protocol using SDS-PAGE. The M2 monomer runs as a band of approximately 15 kDa, and the dimer runs as a band of approximately 25 kDa.

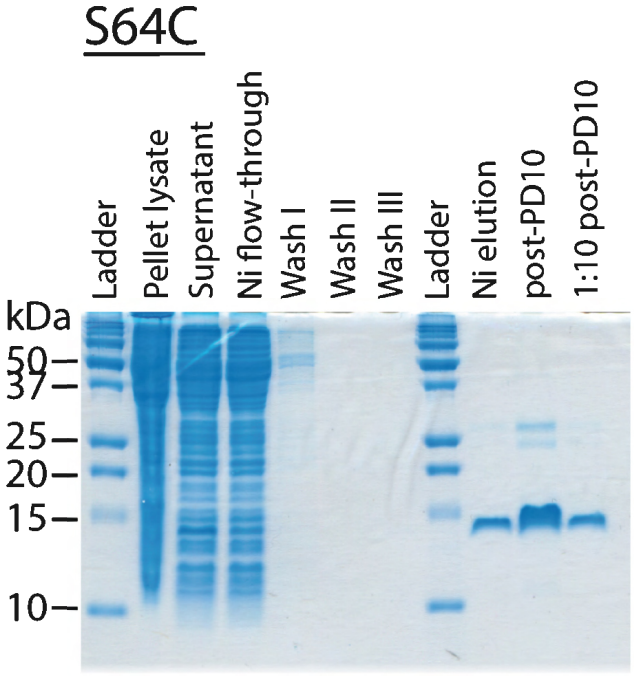


**Figure S3.2. Sequence analysis of the full-length cysteineless M2 protein.**
(A) PSIPRED indicates the predicted secondary structure of an amino acid sequence.[64] Pink cylinder, alpha-helix. Yellow arrow, beta-sheet. (B) DISOPRED measures the predicted intrinsic disorder of a sequence.[68] A significant value is beyond the 0.5 confidence score cutoff.

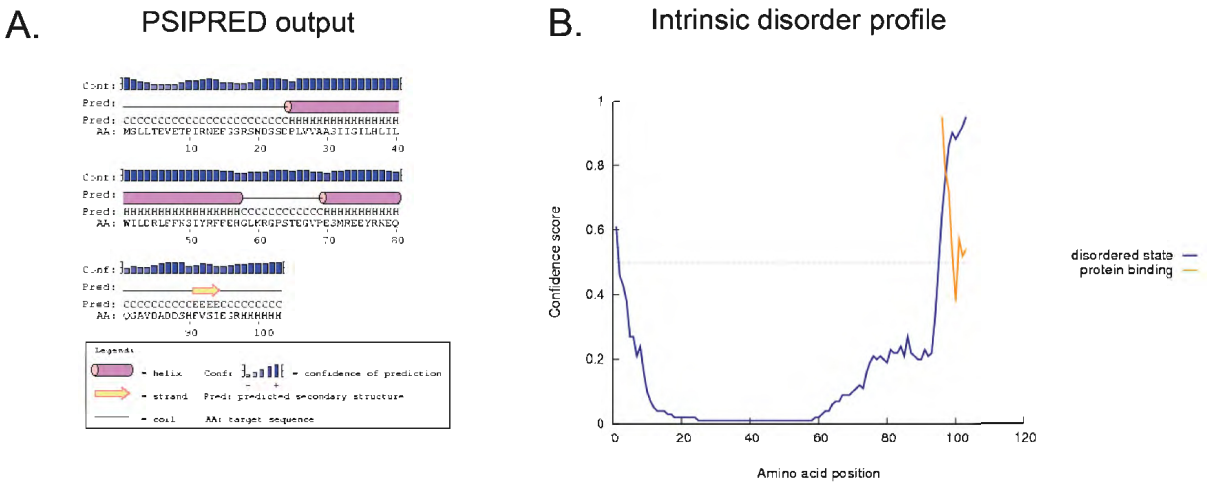

**Figure S3.3. The CD spectra of cysteineless and H57R1 M2 constructs reconstituted in 4:1 POPC:POPG proteoliposomes at a 1:500 protein:lipid ratio.**
The normalized molar ellipticity is in units of molar circular dichroism ($\Delta\varepsilon$, $M^{-1}cm^{-1}$). The M2 H57R1 spectrum exhibits stronger double minima at approximately 208 and 222 nm and a maximum at 190 nm, indicating higher α-helical character than the cysteineless protein. However, the relatively shallow minima exhibited by the cysteineless protein may be attributed to the age of the sample. Scattering caused by the liposomes combined with the low protein:lipid ratio limit the resolution of the spectrum and preclude spectral deconvolution.

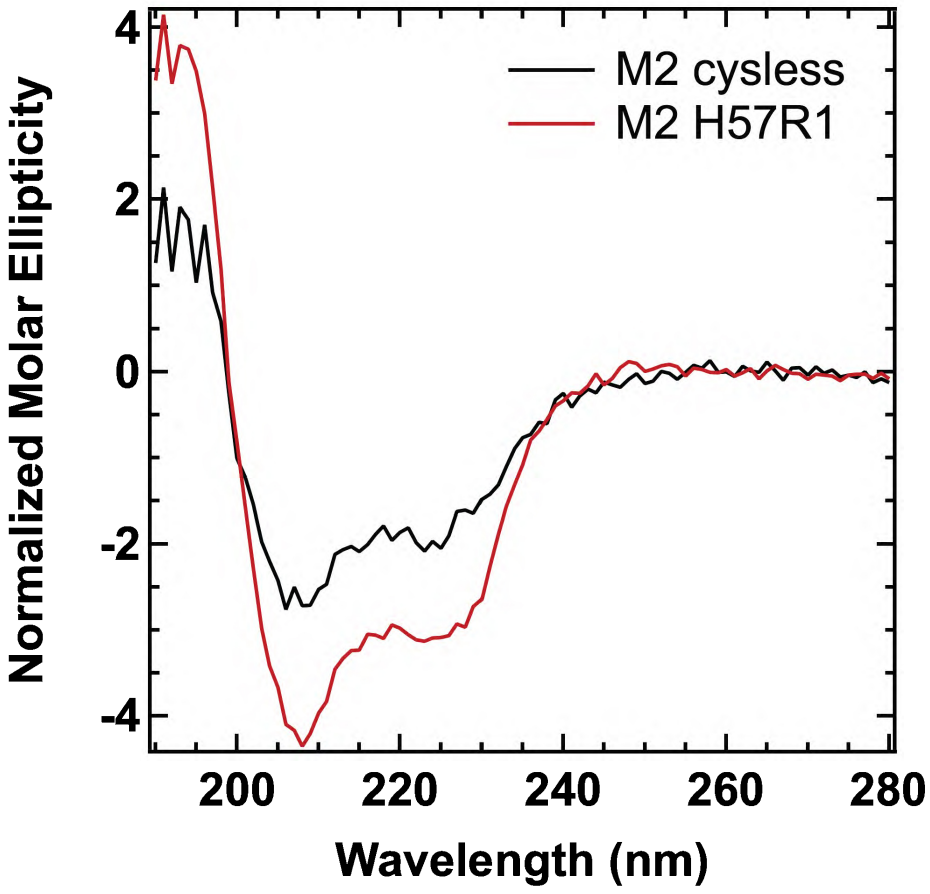

**Table S3.1. Mobility parameter ($\Delta H_0^{-1}$) data for spin labels at sites 50-70 of the full-length M2 protein reconstituted into 4:1 POPC:POPG bilayers.**
The data are shown in graphical form in Chapter 3, Figure 2. The error is described in Appendix C.

| Spin-Labeling Site | $\Delta H_0^{-1}$ ($G^{-1}$) | $\Delta H_0^{-1}$ Error ($G^{-1}$) |
|---|---|---|
| L43 | 0.256 | 0.01 |
| C50 | 0.227 | 0.02 |
| I51 | 0.213 | 0.03 |
| Y52 | 0.263 | 0.02 |
| R53 | 0.200 | 0.02 |
| F54 | 0.278 | 0.05 |
| F55 | 0.286 | 0.02 |
| E56 | 0.294 | 0.01 |
| H57 | 0.213 | 0.01 |
| G58 | 0.244 | 0.01 |
| L59 | 0.294 | 0.02 |
| K60 | 0.286 | 0.03 |
| R61 | 0.370 | 0.02 |
| G62 | 0.526 | 0.06 |
| P63 | 0.400 | 0.03 |
| S64 | 0.455 | 0.03 |
| T65 | 0.526 | 0.06 |
| E66 | 0.526 | 0.04 |
| G67 | 0.455 | 0.11 |
| V68 | 0.526 | 0.11 |
| P69 | 0.526 | 0.04 |
| E70 | 0.556 | 0.05 |

**Table S3.2. Accessibility data for spin labels at sites 50-70 of the full-length M2 protein reconstituted into 4:1 POPC:POPG bilayers.**
The data are shown in graphical form in Chapter 3, Figure 2. Errors represent the 95% confidence interval.

| Spin-Labeling Site | $P_{1/2}$ ($N_2$) | $P_{1/2}$ ($O_2$) | $P_{1/2}$ (NiEDDA) | $P_{1/2}$ (Ni Lipid) |
|---|---|---|---|---|
| L43 | 20.4508 | 144.39 | 27.003 | 0.655 |
| C50 | 15.0982 | 80.7662 | | |
| I51 | 17.4572 | 93.1623 | | |
| Y52 | 18.3883 | 101.354 | | |
| R53 | 24.1271 | 13.3101 | | |
| F54 | 7.9281 | 54.1275 | | |
| F55 | 16.572 | 85.2529 | | |
| E56 | 15.4738 | 61.7146 | | |
| H57 | 18.1681 | 61.17 | 59.822 | 0.883 |
| G58 | 19.4867 | 70.1528 | | |
| L59 | 18.8416 | 83.9373 | | |
| K60 | 17.3065 | 48.1676 | 29.851 | |
| R61 | 13.6199 | 42.3102 | | |
| G62 | 12.2454 | 26.5544 | | |
| P63 | 15.176 | 37.2284 | | |
| S64 | 13.408 | 32.163 | 94.5568 | 0.577 |
| T65 | 15.994 | 30.109 | | |
| E66 | 15.2637 | 33.7565 | | |
| G67 | 13.7214 | 25.4421 | | |
| V68 | 7.79421 | 19.0289 | 178.07 | 1.43 |
| P69 | 11.3743 | 26.1267 | | |
| E70 | 14.4359 | 28.9398 | | |

# Chapter S2 Supporting Information for Chapter 4: Cholesterol-Dependent Conformational Exchange of the Full-Length Influenza A M2 Protein and a Mutant Exhibiting Impaired Viral Scission

## SUPPORTING MATERIALS AND METHODS.

### Expression of M2 and PentaAla Cysteine Constructs.

The following plasmids were chemically transformed into OverExpress C43(DE3) competent cells according to the supplier's protocol: M2 cysteineless, M2 L43C, pentaAla cysteineless, pentaAla L43C, and pentaAla H57C. A 5 mL aliquot of Luria Broth (LB) supplemented with 100 $\mu$g/mL ampicillin was inoculated directly from a glycerol cell stock and was incubated at 37°C overnight (8-12 hrs) with shaking at 160-180 rpm. The entire 5 mL of overnight cell growth was transferred into 1L sterilized LB supplemented with 100 $\mu$g/mL ampicillin. When the $OD_{600}$ reached 0.7-1.0 (typically 2-3 hours), M2 expression was induced with 1 mM IPTG. After the OD stopped increasing (typically 2-3 hours), expression was halted by centrifugation at for 30 minutes at 4000 rpm, 9 acc / 5 dec, 4°C. Cell pellets were resuspended in ~50 mL fresh LB per liter of growth and were centrifuged again for 30 minutes at 4000 rpm, 9 acc / 5 dec, 4°C. The supernatant was discarded and cell pellets corresponding to ¼ L or ½ L of growth were stored at -80°C until purification. A summary of the physical parameters of these constructs is provided in Appendix C.

### Purification and Spin Labeling.

The purification performed based on previously published protocols with minor modifications.[18] A frozen cell pellet from ¼ or ½ L of growth was incubated in lysis

buffer (50 mM Tris pH 8, 30 mM octyl β-D-glucopyranoside (OG), 150 mM NaCl, 0.2 mg/mL DNase I, 0.25 mg/mL lysozyme, and 50 mM AEBSF) for 30-45 minutes on ice. The pellet was briefly vortexed and then sonicated on ice at 20% amplitude, 20 minutes, 1 sec on / 1 sec off. The total sonication time was 40 minutes. The lysate was centrifuged at 16,000 rpm for 30 minutes at 4°C. The clarified supernatant was decanted and supplemented with 7 mM β-mercaptoethanol and 20 mM imidazole.

A column with 0.5 mL Nickel-nitrilotriacetic acid (Ni-NTA) resin (Thermo Fisher) was equilibrated with 10 column volumes of ultrapure water followed by 10 column volumes of 50 mM Tris pH 8, 30 mM OG, 150 mM NaCl, and 20 mM imidazole buffer. The lysate supernatant was incubated on the column for 30 minutes with nutation at room temperature. The column was washed successively with 10 column-volumes of Wash I (50 mM Tris pH 8, 150 mM NaCl, 30 mM OG, 20% v/v glycerol), Wash II (50 mM Tris pH 8, 30 mM OG, 20% v/v glycerol), and Wash III (50 mM Tris pH 8, 30 mM OG, 20% v/v glycerol, 20 mM imidazole). Tenfold molar excess of (1-Oxyl-2,2,5,5-tetramethyl-Δ3-pyrroline-3-methyl) Methanethiosulfonate spin label (MTSL; Ontario Research Chemicals) was dissolved in 16 $\mu$L acetonitrile and diluted in 1 mL Wash III. The MTSL solution was applied to the column and was incubated for 24-48 hours at room temperature with nutation. The MTSL solution was allowed to elute, and the column was nutated for 20 minutes with Wash II to facilitate the removal of free spin label. The column was washed an additional 20 column-volumes of Wash II, followed by elution of the protein with Elution Buffer (50 mM Tris, 300 mM imidazole, 30 mM OG, and 20% v/v glycerol) until the A280 indicated that no protein remained on the column. The protein solution was buffer-swapped into 50 mM Tris pH 8, 30 mM OG buffer using

PD-10 desalting columns (GE Healthcare). The purity of protein was verified using Sodium dodecyl sulfate polyacrylamide gel electrophoresis.

The concentration of spin-labeled protein was determined according to a TEMPO calibration curve. The spin-labeling efficiency was calculated by comparing the concentration of spin-labeled protein to the concentration of protein determined from the A280 (Appendix C).

### Reconstitution of the M2 Protein into POPC:POPG Liposomes With 0 and 30% Cholesterol.

Premade lipid films consisting of $6.6x10^{-6}$ mol lipids were rehydrated in extruder buffer (50 mM Tris pH 7.8, 100 mM KCl, 1 mM EDTA) to achieve a concentration of 9.36 mg/mL lipids. The lipids were resuspended by alternative vortexing and bath sonication. The lipid suspension was extruded 15 times through 20 $\mu$m filter using an Avanti Mini Extruder. The lipids were solubilized to an OG concentration of 30-35 mM using a 25 mg/mL, 50 mM Tris pH 7.8, 100 mM KCl, 1 mM EDTA buffer, and the detergent/lipid solution was equilibrated for 30 minutes. Protein was added to achieve a protein:lipid ratio of 1:500. The solution was diluted by half with extruder Buffer to lower the OG concentration to below the CMC. A slurry of Bio-Beads was prepared by hydrating the beads in extruder Buffer and degassing under vacuum for an hour. The dilute proteoliposomes were nutated at 4°C while approximately 50 $\mu$L of the BioBead slurry was added to the proteoliposomes in 15 minute intervals until the total volume of BioBeads was 300 $\mu$L. The proteoliposome solution was concentrated by two rounds of ultracentrifugation at 90,000 rpm for 60 minutes at 4°C. The samples were frozen at -20°C and thawed prior to data collection. For NiEDDA sample preparation, 50 mM

NiEDDA, 50 mM Tris pH 8, 100 mM KCl buffer was used instead of extruder buffer. For nickel-chelate lipid sample preparation, 50 mM Tris pH 8, 100 mM KCl buffer was used instead of extruder buffer.

### Preparation of 4:1 POPC:POPG and 56:14:30 POPC:POPG:Cholesterol Saturation Recovery Samples.

Following CW EPR data collection, M2 and pentaAla H57R1 80:20 POPC:POPG and 56:14:30 POPC:POPG:Cholesterol proteoliposomes were resuspended in approximately 200 $\mu$L of extruder buffer and were pelleted by one round of ultracentrifugation at 90,000 rpm for 60 minutes at 4°C. The samples were stored on dry ice and were shipped to the Biomedical Electron Paramagnetic Resonance Center (Milwaukee, WI). Prior to saturation recovery sample preparation, samples were allowed to thaw 10-15 minutes and were resuspended in 20 $\mu$L extruder buffer.

### Circular Dichroism of M2 and PentaAla in 4:1 POPC:POPG and 56:14:30 POPC:POPG:Cholesterol Proteoliposomes.

For each sample, 3.3 x $10^{-6}$ moles of 4:1 POPC:POPG lipid films or 56:14:30 POPC:POPG:Cholesterol lipid films were rehydrated to 9.36 mg/mL in extruder buffer. Cysteineless and H57R1 M2 protein was reconstituted into the lipids in a 1:500 protein:lipid ratio as described above, with the exception that samples were not concentrated via ultracentrifugation. Instead, the dilute proteoliposome samples were treated according to the procedure described below. A liposome sample was prepared using the same lipid composition and sample preparation protocol.

To minimize solvent absorption, proteoliposome solutions were diluted with Millipore water by a factor of 2.5 to a final concentration of 20 mM Tris pH 7.8, 40 mM KCl. Diluted samples were concentrated by centrifugation with a 10K MWCO Amicon to a final protein concentration of approximately 0.5 mg/mL as estimated from the A280 and an extinction coefficient of 8480 $M^{-1}cm^{-1}$ for M2 and an extinction coefficient of 6990 $M^{-1}cm^{-1}$ for pentaAla (Appendix C). The actual protein concentration of proteoliposome samples was measured using the $A_{280}$ on a Nanodrop spectrometer using a 50% dilution of an aliquot of the proteoliposome sample in 10% sodium dodecyl sulfide (SDS) to correct for solvent flattening.

CD spectra were collected on an Aviv Model 435 Circular Dichroism spectrometer at 25°C. A 35 $\mu$L aliquot of sample was loaded into 0.011 cm path length demountable quartz cuvette. Spectra were collected from 280 nm to 190 nm with a 1 nm step size. The averaging time at each point was 5 seconds, and the bandwidth was 2 mm. Three scans were collected and averaged. Spectral data collected directly from the instrument were converted from units of millidegrees to per residue molar absorption units (also known as molar circular dichroism, $\Delta\varepsilon$, in units of $M^{-1}cm^{-1}$) using the following equation:

$$\Delta\varepsilon = \theta * \frac{0.1 * MRW}{(P * CONC) * 3298} \quad (1)$$

where $\theta$ is spectral intensity data in millidegrees, P is the path length of the cuvette in cm, CONC is the protein concentration corrected for solvent flattening in units of mg/mL, and MRW (amu) is the mean residue weight defined as

$$MRW = \frac{protein\ MW}{number\ of\ residues} \quad (2)$$

A table of physical parameters corresponding to the M2 constructs used here is provided in Appendix C. The baseline scattering pattern produced by the liposome samples was subtracted from the proteoliposome CD signal. During sample collection, the 56:14:30 POPC:POPG:Cholesterol liposomes precipitated out of solution.

## SUPPORTING DISCUSSION.

### Spectral Simulation of M2 and pentaAla Sites L43 and H57.

In order to resolve some of the ambiguities of mobility analysis that arise from multi-component spectra and to gain more quantitative information about the motion experienced by the spin label in the two conformations, we performed spectral simulation for sites 43 and 57 using MultiComponent, a LabVIEW program based on the MOMD approach.[48] Spectra were simulated with two motional components to produce a reasonable fit (Figure S2.2). The mobile and immobile components of M2 site 43 have correlation times of 2.47 and 8.78 ns, respectively. In cholesterol-free and 30% cholesterol environments, the relative population of the immobile component for site 43 is 44 and 84%, respectively. M2 site 57 has correlation times of 3.1 and 10.4 ns for the mobile and immobile components, respectively. In cholesterol-free and 30% cholesterol environments, the relative population of the immobile component for site 57 is 78 and 88%, respectively.

Remarkably, simulations of the pentaAla L43R1 and H57R1 spectra yield components with the same correlation times as reported for the corresponding sites in M2 (Tables S2.1-4). However, the relative populations of the two components differ markedly. In cholesterol-free and 30% cholesterol environments, the relative population of the immobile component for pentaAla site 43 is 84 and 85%, respectively. For the

amphipathic helix sites, the relative population of the immobile component is 35 and 59%, respectively. The similarities in the correlation times of the different components of pentaAla and M2 transmembrane and amphipathic helix sites suggest that spin labels in both constructs experience similar environments. However, conformational exchange between the two environments is severely limited by the five alanine substitions to the amphipathic helix. In contrast, the mutations appear to abolish conformational exchange in the transmembrane domain. Notably, these spectral simulations were performed with the assumption that the pentaAla mutant continues to sample a two-conformational equilibrium and require further experimental validation.

### Assessing the Relative Depth of M2 and pentaAla Site 57.

One interesting observation is that pentaAla H57R1 has both lower oxygen and NiEDDA accessibility than the corresponding site in M2 in environments with and without cholesterol (Figure 4.2F and G). In order to gain insight about the relative depth of the spin labeled sites in the membrane, we calculated the depth parameter $\Phi = \ln[\Delta P_{1/2}(O_2)/\Delta P_{1/2}(\text{NiEDDA})]$. High exposure to oxygen and minimal exposure to NiEDDA, as is expected when a spin label is positioned in the membrane, results in a positive depth parameter. Conversely, more solvent-exposed labels have zero or negative depth parameters.[43,44] PentaAla site H57R1 has depth parameters of 0.47 and -0.39 in bilayers lacking and containing cholesterol, respectively. The corresponding M2 site has depth parameters of 0.032 and -1.2 under the same conditions. Converting these values into specific distances within the membrane presents challenges, as reliable distance calibration points are difficult to obtain for the interfacial region.[116] However, the relative

values of the depth parameters of the mutant and wild-type sites suggest that substitution of the five bulky hydrophobic residues results, somewhat unexpectedly, in site 57 becoming less solvent-exposed. Such a result may arise from a rotation around the helical axis, which could bring site 57 in closer proximity to the membrane. Rotation around the helical axis in the M2 protein has previously been observed in response to a pH-induced conformational change.[17] The depth parameter could not be calculated for transmembrane helix sites due to the low accessibility of these residues to NiEDDA.

### Preliminary CD Spectra Suggest the pentaAla Substitutions Do Not Alter the Global Secondary Structure of the M2 Protein.

Circular dichroism spectra of the cysteineless M2 and pentaAla constructs reconstituted into 4:1 POPC:POPG membranes with 0% and 30% cholesterol are shown in Figure S2.4. Scattering caused by the liposomes combined with the low protein:lipid ratio limit the resolution of the spectrum and preclude spectral deconvolution. M2 and pentaAla in 4:1 POPC:POPG proteoliposomes (black and green traces, respectively) exhibit similar spectral features and intensities from 200-280 nm, suggesting that the global secondary structure characteristics of these two constructs is similar. Differences in the absorbance at 190 nm may arise from lipid absorption in this region or differences in solvent flattening between samples.[88] Spectra of M2 and pentaAla protein in POPC:POPG proteoliposomes with cholesterol were collected and are included for reference; however, precipitation was observed throughout the course of sample collection. These spectra are therefore not subject to interpretation. Future CD experiments will use a higher protein:lipid ratio and bicelles in lieu of proteoliposomes to improve signal and limit scattering, respectively.

**CHAPTER S2 SUPPORTING FIGURES AND TABLES.**

**Figure S2.1. Representative purification gels of M2 and pentaAla single-cysteine constructs.**
The purity of cysteine constructs was assessed at each stage in the purification protocol using SDS-PAGE. The M2 monomer runs as a band of approximately 15 kDa, and the dimer runs as a band of approximately 25 kDa. The pentaAla monomer appears to run as two bands at approximately 11 kDa and 15 kDa, and the dimer runs as two bands at approximately 20 kDa and 25 kDa.

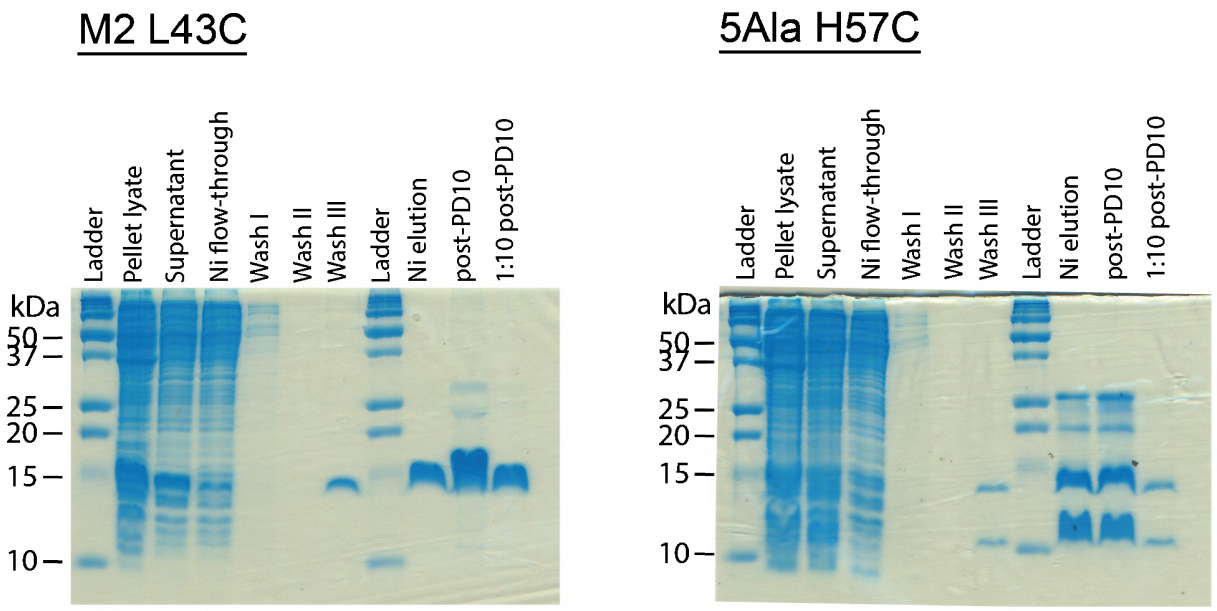

**Figure S2.2. Simulated fits of M2 and pentaAla sites 43 and 57 reconstituted into 4:1 POPC:POPG membranes with 0% and 30% cholesterol.**
The percentage on the left or right-hand side of each spectrum refers to the relative population of the immobile component. Fits were performed by Stuart Arbuckle '17.[54]

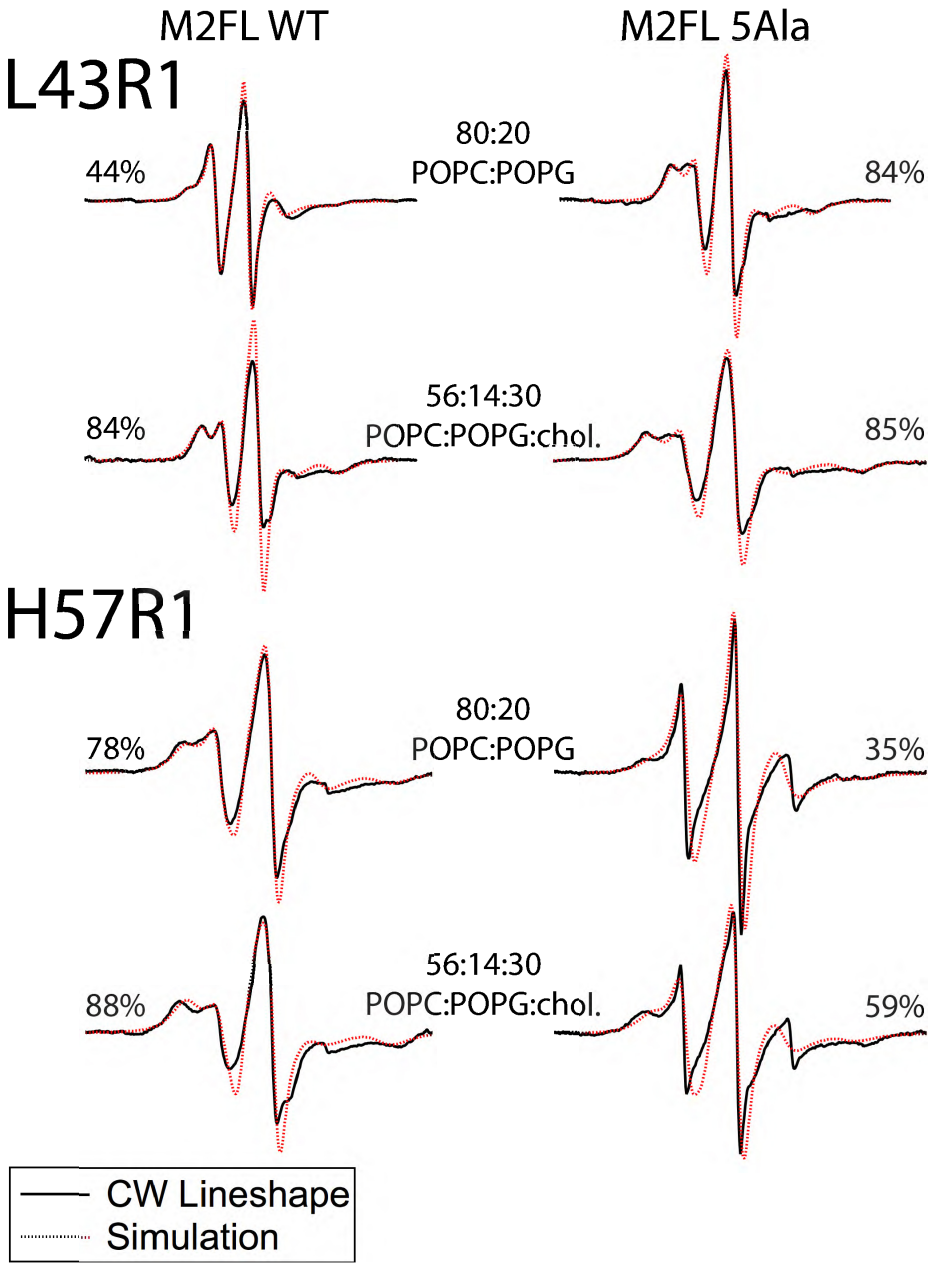

**Figure S2.3. Sequence analysis of the full-length pentaAla M2 protein.**
PSIPRED indicates the predicted secondary structure of an amino acid sequence.[64] Pink cylinder, alpha-helix. Yellow arrow, beta-sheet.

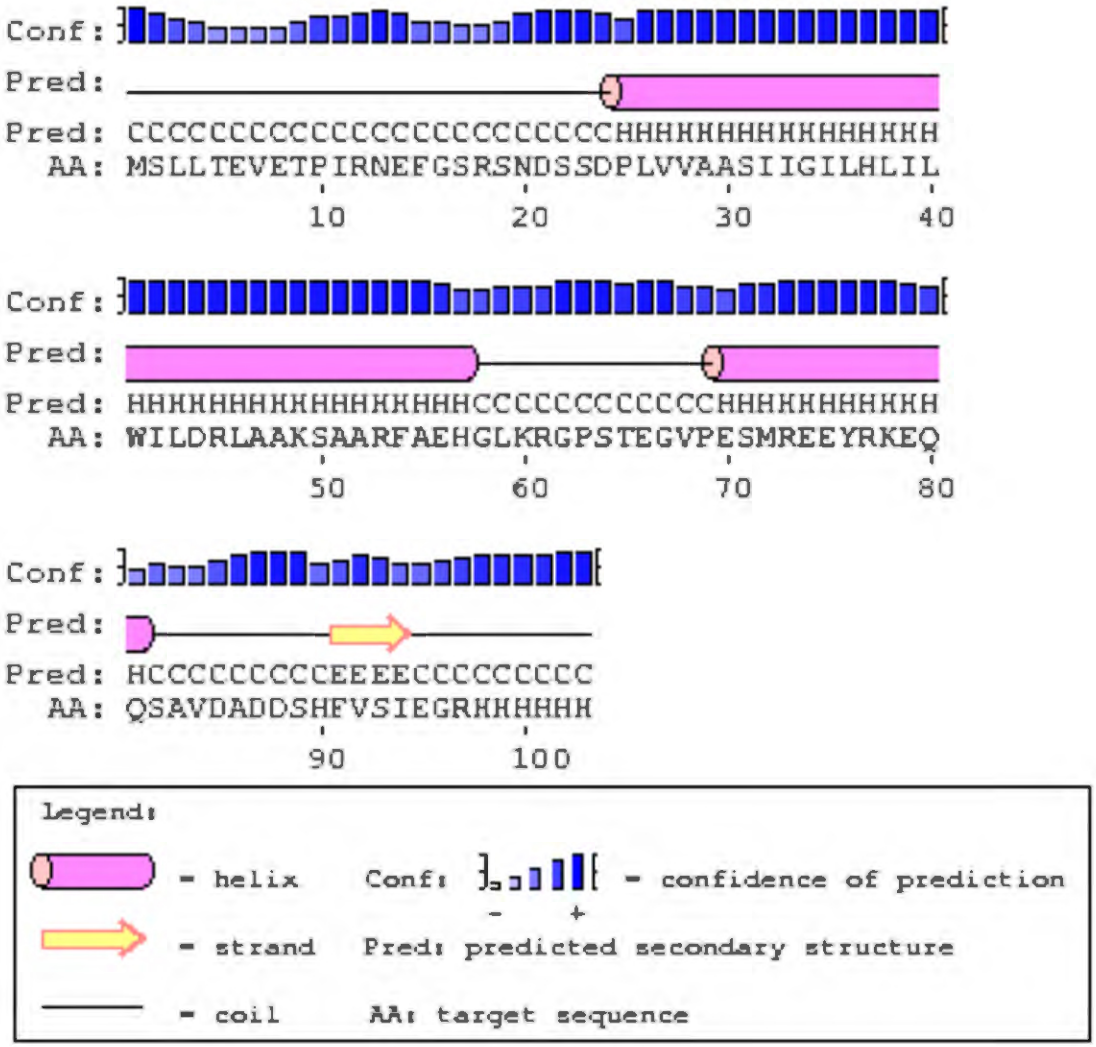

**Figure S2.4. The CD spectra of cysteineless M2 and pentaAla constructs reconstituted into 4:1 POPC:POPG proteoliposomes with 0% and 30% cholesterol at a 1:500 protein:lipid ratio.**
All spectra exhibit double minima at approximately 208 and 222 nm and a maximum at 190 nm, indicating α-helical character.

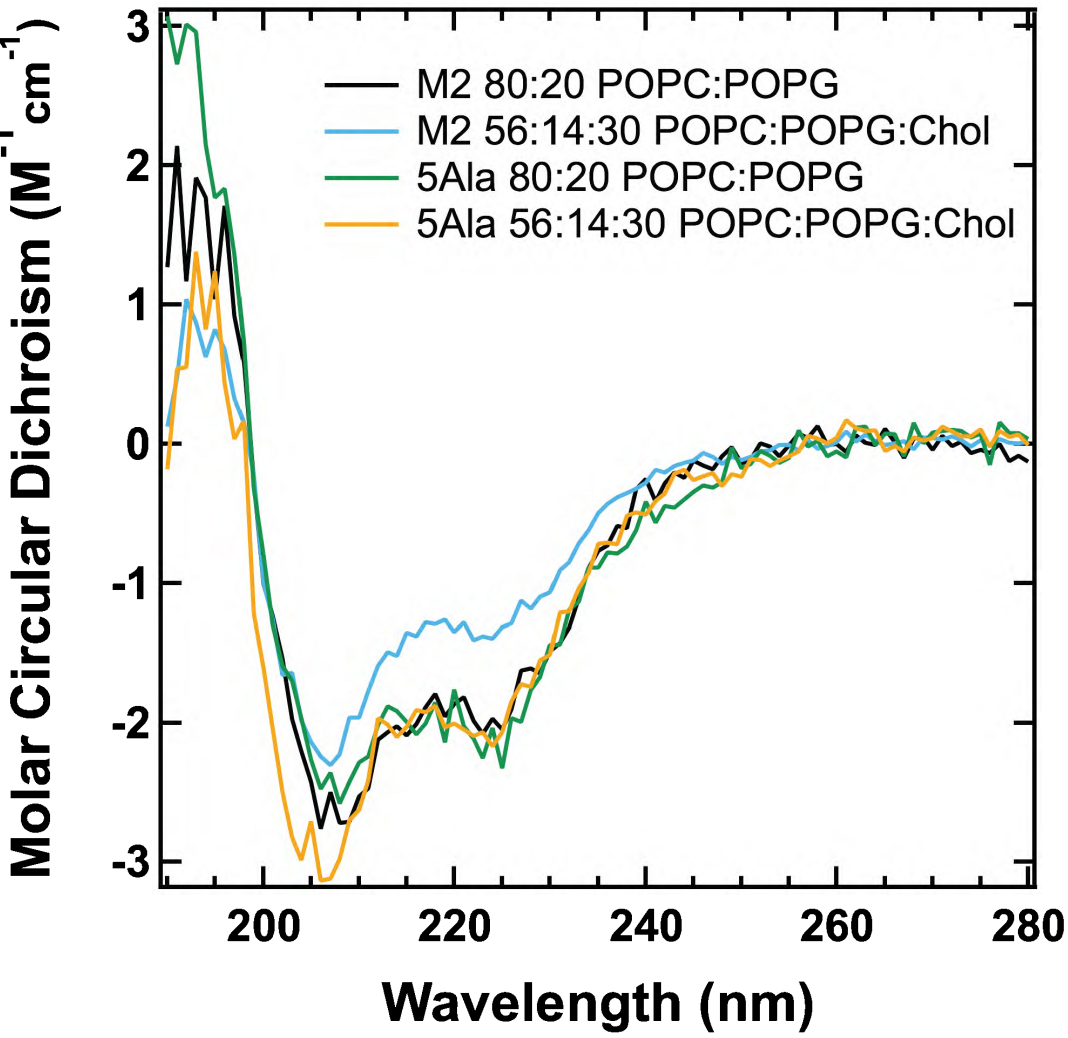

**Table S2.1 A summary of the MultiComponent fit parameters obtained by spectral simulation of M2 L43R1.**

| Site | Membrane | % mobile | % immobile | $t_c$, mobile | $t_c$, immobile |
|---|---|---|---|---|---|
| 43 | 80/20 POPC/POPG | 16 | 84 | 2.47 | 8.78 |
| 43 | 56/14/30 POPC/POPG/Chol | 15 | 85 | 2.47 | 8.78 |

**Table S2.2. A summary of the MultiComponent fit parameters obtained by spectral simulation of M2 H57R1.**

| Site | Membrane | % mobile | % immobile | $t_c$, mobile | $t_c$, immobile |
|---|---|---|---|---|---|
| 57 | 80/20 POPC/POPG | 22 | 78 | 3.1 | 10.4 |
| 57 | 56/14/30 POPC/POPG/Chol | 12 | 88 | 3.1 | 10.4 |

**Table S2.3. A summary of the MultiComponent fit parameters obtained by spectral simulation of pentaAla L43R1.**

| Site | Membrane | % mobile | % immobile | $t_c$, mobile | $t_c$, immobile |
|---|---|---|---|---|---|
| 43 | 80/20 POPC/POPG | 16 | 84 | 2.47 | 8.78 |
| 43 | 56/14/30 POPC/POPG/Chol | 15 | 85 | 2.47 | 8.78 |

**Table S2.4 A summary of the MultiComponent fit parameters obtained by spectral simulation of pentaAla H57R1.**

| Site | Membrane | % mobile | % immobile | $t_c$, mobile | $t_c$, immobile |
|---|---|---|---|---|---|
| 57 | 80/20 POPC/POPG | 65 | 35 | 3.1 | 10.4 |
| 57 | 56/14/30 POPC/POPG/Chol | 41 | 59 | 3.1 | 10.4 |

# Chapter S3 Supporting Information for Chapter 5: Curvature-Dependent Conformational Exchange of the Full-Length Influenza A M2 Protein and a Mutant Exhibiting Impaired Viral Scission

## SUPPORTING MATERIALS AND METHODS.

### Expression of M2 and PentaAla Cysteine Constructs and Purification and Spin Labeling.

Identical protein stocks were used for the experiments described in Chapters 4 and 5. Expression, Purification, and Spin Labeling protocols are described in Chapter S2.

### Preparation of DOPC/DOPS and DOPE/DOPS Lipid Stocks With 0 and 30% Cholesterol.

1,2-dioleoyl-sn-glycero-3-phospho-L-serine sodium salt (DOPS) and 1,2-dioleoyl-sn-glycero-3-phosphoethanolamine (DOPE) lipids were purchased as 25 mg/mL chloroform stocks from Avanti Polar Lipids (Alabaster, AL). 1,2-dioleoyl-sn-glycero-3-phosphocholine (DOPC) was purchased from the same company as a powder and was dissolved into chloroform at a concentration of 25 mg/mL prior to use. Cholesterol powder was dissolved to a concentration of 25 mg/mL prior to use. Chloroform solutions of lipids were combined in a 80/20 DOPC/DOPS or DOPE/DOPS molar ratio. Chloroform samples were prepared from chloroform solutions of 56/14/30 DOPC/DOPS/Cholesterol or 56/14/30 DOPE/DOPS/Cholesterol molar ratios. Chloroform was evaporated under a gentle stream of nitrogen, and the lipid films were lyophilized for 12 hours. Protein was reconstituted into proteoliposomes as previously described (Chapter S2), with the following exceptions.

Protein was reconstituted into vesicles at a 1:40 protein:lipid ratio. Due to the prohibitive protein requirements, some reconstitutions were performed using one-third or

one-sixth of the amount of lipids and protein described in Chapter S2 (i.e. $2.2x10^{-6}$ mol lipids and $1.1x10^{-6}$ mol lipids for one-third and one-sixth size reconstitutions, respectively). Additionally, dilute-labeled samples were prepared from cysteineless and labeled protein stocks combined in a 3:1 ratio. Dilution of the spin-labeled protein with cysteineless protein minimizes the effects of dipolar broadening, which precludes accurate fitting of CW spectral line shapes with the Multicomponent software package.[48]

### Preparation of 80/20 DOPC/DOPS, 56/14/30 DOPC/DOPS/Cholesterol, and 80/20 DOPE/DOPS Saturation Recovery Samples.

Following CW EPR data collection, fully labeled M2 and pentaAla H57R1 80/20 DOPC/DOPS, 56/14/30 DOPC/DOPS/Cholesterol, and 80/20 DOPE/DOPS proteoliposomes were resuspended in approximately 200 $\mu$L of extruder buffer and were pelleted by one round of ultracentrifugation at 90,000 rpm for 60 minutes at 4°C. The samples were stored on dry ice and were shipped to the Biomedical Electron Paramagnetic Resonance Center (Milwaukee, WI). Prior to saturation recovery sample preparation, samples were allowed to thaw 10-15 minutes and were resuspended in 20 $\mu$L extruder buffer.

### Circular Dichroism of M2 and PentaAla in 80/20 DOPC/DOPS and DOPE/DOPS Proteoliposomes.

Circular dichroism sample preparation and data collection has been described in Chapter S2. A similar procedure was followed here, with the exception that cysteineless M2 and pentaAla protein was reconstituted at a 1:40 peptide:lipid ratio, and only a small

aliquot of the dilute proteoliposome solution was diluted 2.5-fold in water to achieve s protein concentration of approximately 0.5 mg/mL.

## SUPPORTING DISCUSSION.

### Cautious Interpretation of CD Results of M2 and PentaAla in DOPC/DOPS and DOPE/DOPS Proteoliposomes.

Circular dichroism spectra of cysteineless M2 and pentaAla reconstituted into 80/20 DOPC/DOPS and DOPE/DOPS liposomes are shown in Figure S3.3. The spectra were deconvoluted[117] using the SELCON3, CONTIN, and CDSSTR analysis programs are presented in Tables S3.6-S3.9. Deconvolution was performed using the DichroWeb server.[118]

While the CD spectra produced by the M2 and pentaAla proteoliposome samples were of a high spectral quality, several challenges preclude confident interpretation of spectral analysis program outputs. An NRMSD > 0.1 suggests that the spectrum cannot be reproduced well from the reference set.[117] This result may arise from an inaccurate scaling factor, or the secondary structure of the protein may differ markedly from every other protein in the reference set. In general, CDSSTR produces the smallest NRMSD, whereas SELCON3 produces the highest NRMSD. While a small NRMSD is a requirement for a confident deconvolution, it does not necessarily mean that the results are accurate.[117]

Visual analysis of the deconvolution output indicated that the SELCON3 algorithm did not fit the M2 and pentaAla spectra well. The CONTIN algorithm sometimes did not fit the key alpha-helical regions of ~220 and ~209 nm well. The CDSSTR produced the best fit in each case. All three analysis programs yielded similar

secondary structure content, which is a positive result. Based on the spectral deconvolution performed here, M2 exhibits similar secondary structure characteristics in DOPC/DOPS and DOPE/DOPS membranes, which are known to be in the lamellar and cubic phase, respectively.[41] M2 and pentaAla exhibit similar secondary structure content in DOPE/DOPS membranes; however, the pentaAla sample has ~10% lower helicity in the DOPC/DOPS sample, which may suggest that the amphipathic helix (approximately 10 residues in a ~100-residue peptide) has become unfolded.

However, we hesitate to overinterpret these results for the following reasons. The phase behaviors of the DOPC/DOPS and DOPE/DOPS lipids in the absence of protein are not known. Accurate deconvolution requires subtraction of background liposome scattering from the proteoliposome sample.[88] If the liposome samples exhibit size and shape characteristics that differ from the proteoliposome samples, then the background-subtracted spectral line shapes may be inaccurate. Given that M2 and pentaAla exhibit different phase behavior in DOPC/DOPS and DOPE/DOPS membranes[41], this complication could prevent even a relative comparison of the secondary structure content of the two protein constructs. In the future, CD studies will be performed on bicelles, which produce less scattering and a more homogenous membrane environment.

**SUPPORTING FIGURES AND TABLES.**

**Figure S3.1. Simulated fits of M2 and pentaAla sites 43 and 57 reconstituted into 4:1 DOPC:DOPS and DOPE:DOPS membranes with 0% and 30% cholesterol.**
The percentage on the left or right-hand side of each spectrum refers to the relative population of the immobile component. Fits were performed by Stuart Arbuckle '17.[54]

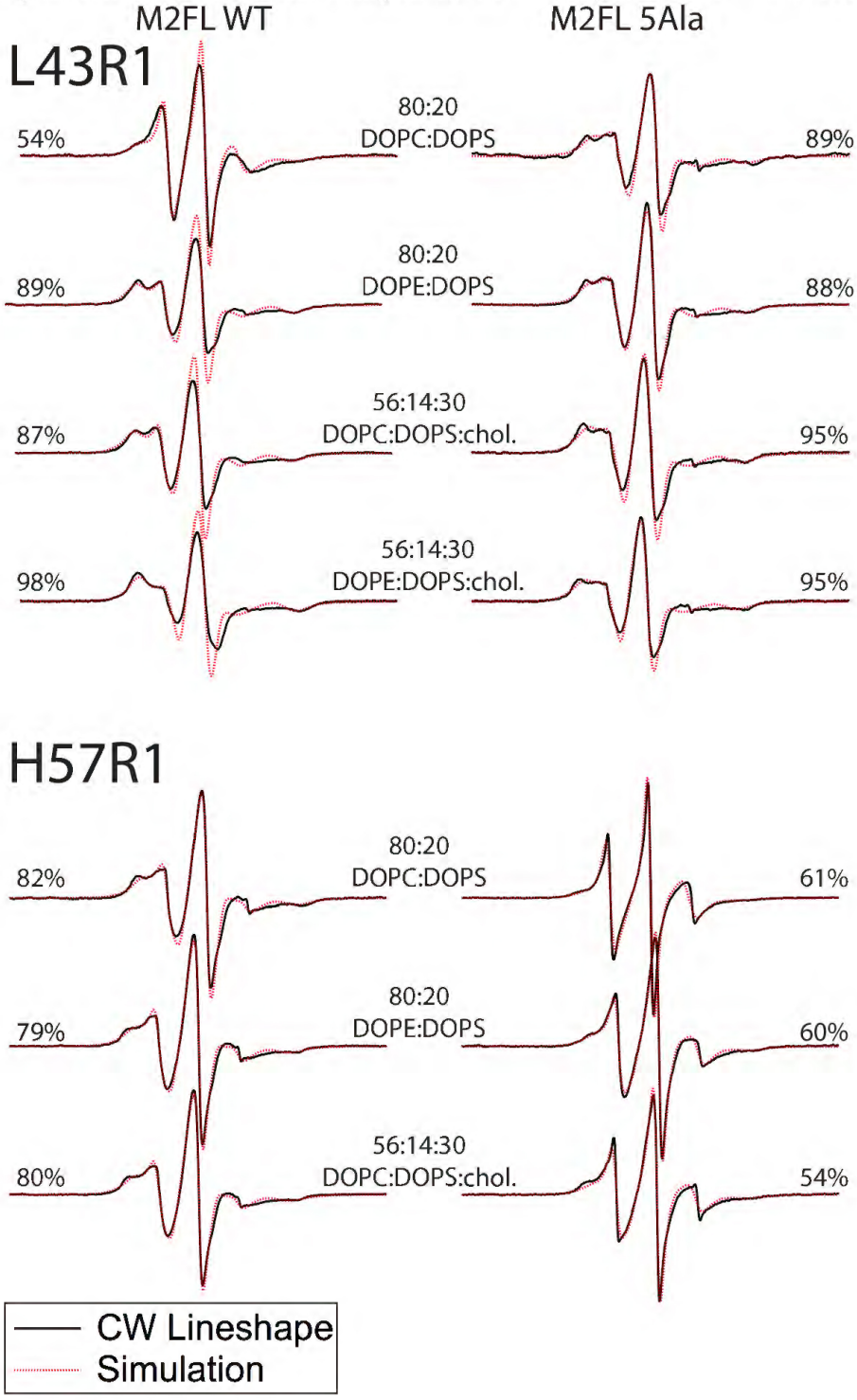

**Figure S3.2. Fully and dilute-labeled spectra of M2 and pentaAla L43R1 in DOPC/DOPS and DOPE/DOPS membranes with 0 and 30% cholesterol at a 1:40 peptide:lipid ratio.**

Dilute-labeled spectra were prepared by diluting spin-labeled protein with cysteineless protein in a 1:3 ratio of labeled:cysteineless protein.

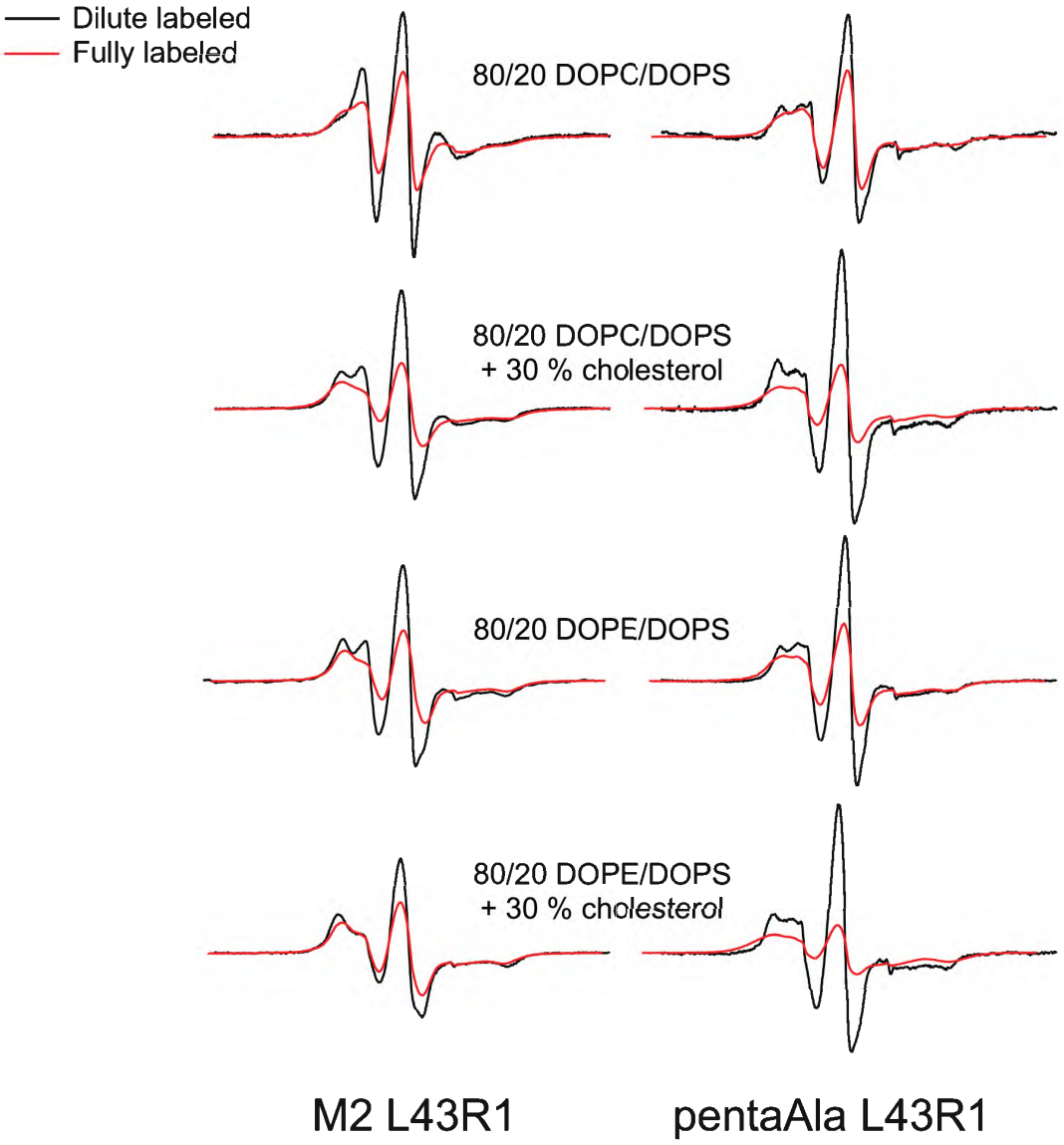

**Figure S3.3. The CD spectra of cysteineless M2 and pentaAla constructs reconstituted into 4/1 DOPC/DOPS and DOPE/DOPS proteoliposomes at a 1:40 protein:lipid ratio.**
All spectra exhibit double minima at approximately 208 and 222 nm and a maximum at 190 nm, indicating α-helical character.

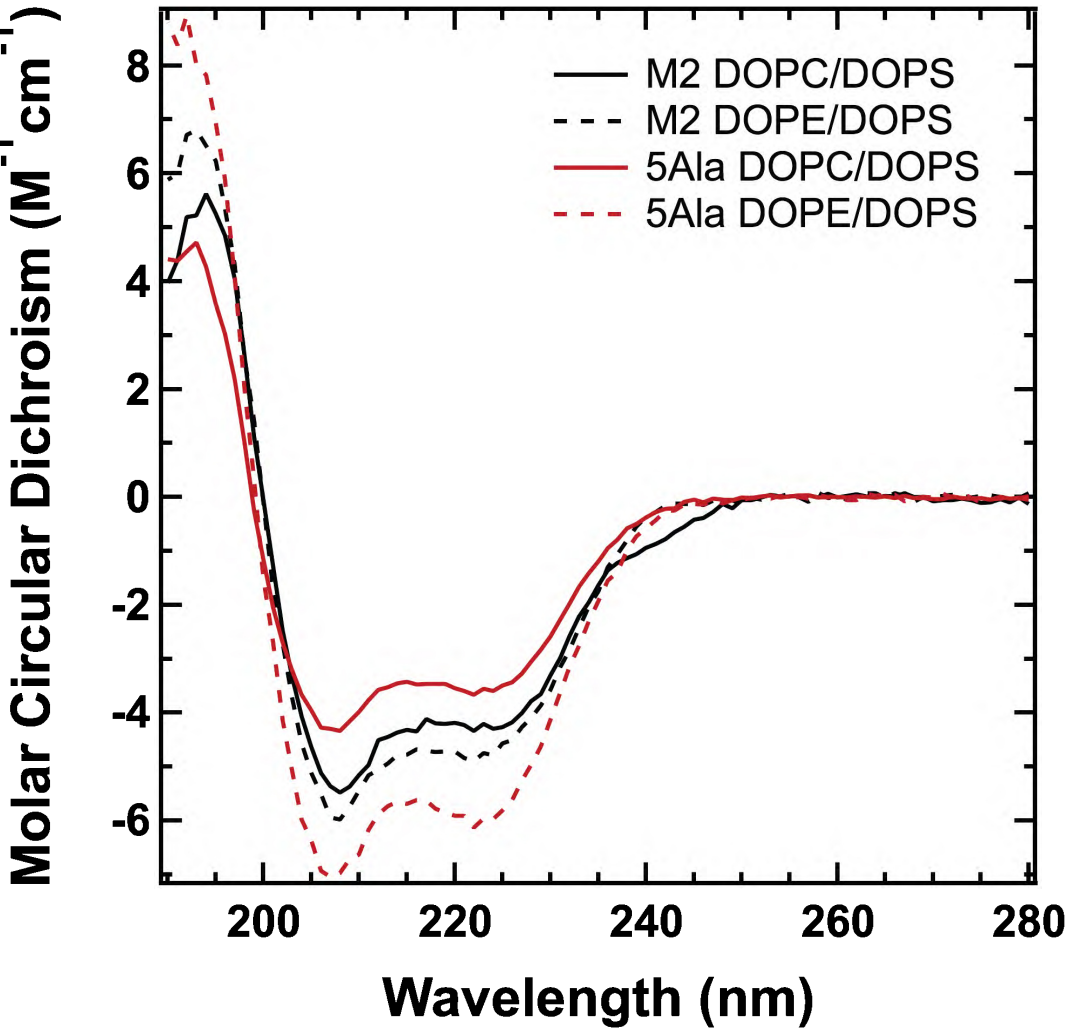

**Table S3.1. A summary of the MultiComponent fit parameters obtained by spectral simulation of M2 H57R1 in the following lipid environments.**

| Site | Membrane | % mobile | % immobile | $t_c$, mobile | $t_c$, immobile |
|---|---|---|---|---|---|
| 57 | 80/20 DOPE/DOPS | 21 | 79 | 3.1 | 9.64 |
| 57 | 80/20 DOPC/DOPS | 18 | 82 | 3.1 | 9.64 |
| 57 | 56/14/30 DOPC/DOPS/Chol | 20 | 80 | 3.1 | 9.64 |

**Table S3.2. A summary of the MultiComponent fit parameters obtained by spectral simulation of pentaAla H57R1 in the following lipid environments.**

| Site | Membrane | % mobile | % immobile | $t_c$, mobile | $t_c$, immobile |
|---|---|---|---|---|---|
| 57 | 80/20 DOPE/DOPS | 60 | 40 | 3.1 | 9.64 |
| 57 | 80/20 DOPC/DOPS | 61 | 39 | 3.1 | 9.64 |
| 57 | 56/14/30 DOPC/DOPS/Chol | 54 | 46 | 3.1 | 9.64 |

**Table S3.3. A summary of the MultiComponent fit parameters obtained by spectral simulation of M2 L43R1 in the following lipid environments.**

| Site | Membrane | % mobile | % immobile | $t_c$, mobile | $t_c$, immobile |
|---|---|---|---|---|---|
| 43 | 80/20 DOPE/DOPS | 11 | 89 | 2.12 | 7.07 |
| 43 | 56/14/30 DOPE/DOPS/Chol | 2 | 98 | 2.12 | 7.07 |
| 43 | 80/20 DOPC/DOPS | 46 | 54 | 2.12 | 7.07 |
| 43 | 56/14/30 DOPC/DOPS/Chol | 13 | 87 | 2.12 | 7.07 |

**Table S3.4. A summary of the MultiComponent fit parameters obtained by spectral simulation of pentaAla L43R1 in the following lipid environments.**

| Site | Membrane | % mobile | % immobile | $t_c$, mobile | $t_c$, immobile |
|---|---|---|---|---|---|
| 43 | 80/20 DOPE/DOPS | 12 | 88 | 3.46 | 8.06 |
| 43 | 56/14/30 DOPE/DOPS/Chol | 5 | 95 | 3.46 | 8.06 |
| 43 | 80/20 DOPC/DOPS | 11 | 89 | 3.46 | 8.06 |
| 43 | 56/14/30 DOPC/DOPS/Chol | 5 | 95 | 3.46 | 8.06 |

For a full summary of fit parameters, including tensors and hyperfine splittings, the interested reader is referred to the thesis of D. Stuart Arbuckle '17.[54]

**Table S3.5. Saturation recovery of the M2 and pentaAla constructs data identify two components in conformational exchange in DOPC/DOPS and DOPE/DOPS membranes.**

Data were collected on M2 and pentaAla H57R1 reconstituted into 4:1 DOPC/DOPS and DOPE/DOPS proteoliposomes with 0% and 30% cholesterol. "Fast" and "slow" refer to the relative relaxation times of the spin label in the two different conformations.

| Construct | Lipid composition | $T_1$ fast (μsec)[a] | $T_1$ slow (μsec)[a] | $W_x$ fast (MHz/mM $O_2$)[b] | $W_x$ slow (MHz/mM $O_2$)[b] |
|---|---|---|---|---|---|
| M2 H57R1 | 4:1 DOPC/DOPS | 2.49 | 4.36 | 3.77 | 1.54 |
| M2 H57R1 | + 30% cholesterol | 2.47 | 4.49 | 2.61 | 0.85 |
| M2 H57R1 | 4:1 DOPE/DOPS | 2.08 | 3.93 | 3.76 | 1.42 |
| 5Ala H57R1 | 4:1 DOPC/DOPS | 2.69 | 5.81 | 3.14 | 1.47 |
| 5Ala H57R1 | + 30% cholesterol | 3.07 | 6.48 | 3.04 | 0.82 |
| 5Ala H57R1 | 4:1 DOPE/DOPS | 3.01 | 4.72 | 3.67 | 0.87 |

[a]spin-latice relaxation times were determined in 0% oxygen, i.e. in nitrogen

[b]slopes of $O_2$ collision rates obtained by collecting data at five different oxygen concentrations

**Table S3.6. CD spectral deconvolution of M2 in 80/20 DOPC/DOPS proteoliposomes.**

| Structural Element | Analysis Program | | | Average |
|---|---|---|---|---|
| | SELCON3 | CONTIN | CDSSTR | |
| Helix1 | 0.274 | 0.245 | 0.350 | 0.290 |
| Helix2 | 0.197 | 0.185 | 0.210 | 0.197 |
| HelixSum | 0.471 | 0.430 | 0.560 | 0.487 |
| Strand1 | -0.026 | 0.000 | 0.040 | 0.005 |
| Strand2 | 0.051 | 0.058 | 0.020 | 0.043 |
| StrandSum | 0.025 | 0.058 | 0.060 | 0.048 |
| Turns | 0.144 | 0.136 | 0.170 | 0.150 |
| Unordered | 0.360 | 0.376 | 0.210 | 0.315 |
| NRMSD | 0.204 | 0.111 | 0.009 | 0.108 |

**Table S3.7. CD spectral deconvolution of M2 in 80/20 DOPE/DOPS proteoliposomes.**

| Structural Element | Analysis Program | | | Average |
|---|---|---|---|---|
| | SELCON3 | CONTIN | CDSSTR | |
| Helix1 | 0.295 | 0.279 | 0.340 | 0.305 |
| Helix2 | 0.206 | 0.187 | 0.210 | 0.201 |
| HelixSum | 0.501 | 0.466 | 0.550 | 0.506 |
| Strand1 | -0.020 | 0.000 | 0.030 | 0.003 |
| Strand2 | 0.048 | 0.052 | 0.030 | 0.043 |
| StrandSum | 0.028 | 0.052 | 0.060 | 0.047 |
| Turns | 0.138 | 0.125 | 0.160 | 0.141 |
| Unordered | 0.351 | 0.357 | 0.250 | 0.319 |
| NRMSD | 0.167 | 0.057 | 0.008 | 0.077 |

**Table S3.8. CD spectral deconvolution of pentaAla in 80/20 DOPC/DOPS proteoliposomes.**

| Structural Element | Analysis Program | | | Average |
|---|---|---|---|---|
| | SELCON3 | CONTIN | CDSSTR | |
| Helix1 | 0.196 | 0.192 | 0.220 | 0.203 |
| Helix2 | 0.163 | 0.149 | 0.190 | 0.167 |
| HelixSum | 0.359 | 0.341 | 0.410 | 0.370 |
| Strand1 | 0.073 | 0.049 | 0.040 | 0.054 |
| Strand2 | 0.073 | 0.082 | 0.050 | 0.068 |
| StrandSum | 0.146 | 0.131 | 0.090 | 0.122 |
| Turns | 0.136 | 0.133 | 0.150 | 0.140 |
| Unordered | 0.359 | 0.396 | 0.330 | 0.362 |
| NRMSD | 0.231 | 0.053 | 0.024 | 0.103 |

**Table S3.9. CD spectral deconvolution of pentaAla in 80/20 DOPE/DOPS proteoliposomes.**

| Structural Element | Analysis Program | | | Average* |
|---|---|---|---|---|
| | SELCON3† | CONTIN | CDSSTR | |
| Helix1 | 0.31 | 0.311 | 0.360 | 0.336 |
| Helix2 | 0.187 | 0.186 | 0.190 | 0.188 |
| HelixSum | 0.497 | 0.497 | 0.550 | 0.524 |
| Strand1 | 0.097 | 0.000 | 0.050 | 0.025 |
| Strand2 | 0.056 | 0.045 | 0.030 | 0.038 |
| StrandSum | 0.153 | 0.045 | 0.080 | 0.063 |
| Turns | 0.101 | 0.12 | 0.110 | 0.115 |
| Unordered | 0.249 | 0.338 | 0.270 | 0.304 |
| NRMSD | 17.092 | 0.061 | 0.008 | 0.035 |

† The SELCON3 analysis program failed to produce a reasonable fit for the CD signal.
*Average was calculated from the CONTIN and CDSSTR outputs only

# Appendix A: Synthesis of the Aqueous Paramagnetic Relaxation Agent NiEDDA for SDSL-EPR Accessibility Studies

EPR power saturation experiments provide insight into the accessibility of a spin label to paramagnetic relaxation reagents[43] (discussed further in Chapter 2). The small, hydrophobic species $O_2$ partitions into the lipid bilayer or sites of close protein-protein interactions and remains largely excluded from the aqueous phase. To obtain complementary information about the accessibility of a spin label to the solution phase, the water-soluble nickel compound nickel ethylenediaminediacetate (NiEDDA) is commonly used. As a neutral compound, NiEDDA can partition to a slight extent in hydrophobic regions; for a paramagnetic relaxation agent that strictly occupies the aqueous phase, the negatively charged compound chromium oxalate (CrOX) may be used.[43]

This chapter documents the synthesis of NiEDDA used in these studies from Nickel (II) hydroxide and Ethylenediamine-N,N′-diacetic acid (Figure A1).

### Synthesis of NiEDDA.

The NiEDDA synthesis protocol was kindly provided by Dr. Jim Feix (Department of Biophysics, National Biomedical EPR Center, Medical College of Wisconsin, Milwaukee, WI) by way of Dr. Christian Altenbach (Jules Stein Eye Institute, UCLA School of Medicine, Los Angeles, CA).

Approximately 880 mg (0.005 mol) of Ethylenediamine-N,N′-diacetic acid (EDDA; Sigma-Aldrich #15,8186; MW = 176.17 g/mol) was dissolved in 350 mL of

Millipore water in a 500 mL round-bottom flask. The solution was stirred on a rotary evaporator (rotovap) with no vacuum until the EDDA completely dissolved (approximately 40 minutes). Approximately 460 mg (0.005 mol) Nickel (II) hydroxide ($Ni(OH)_2$; Sigma-Aldrich #28,362; MW=92.73 g/mol) was added to the EDDA solution. The resulting solution was a turbid light green color due to the presence of insoluble $Ni(OH)_2$. The flask was stirred on a rotovap for 10 hours at 60°C. As the insoluble $Ni(OH)_2$ converted to the soluble NiEDDA, the solution transitioned from green to blue (Figure A1). The flask stirred at room temperature overnight without vacuum.

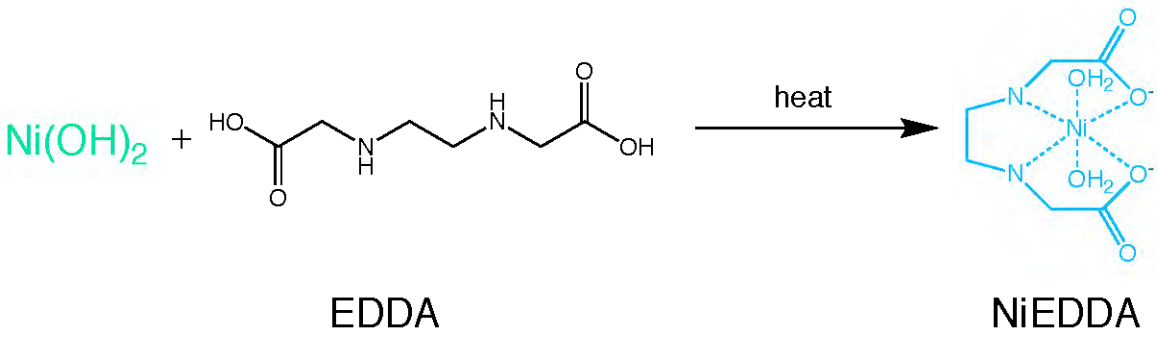


**Figure A1. The synthesis of NiEDDA from nickel (II) hydroxide and Ethylenediamine-N,N′-diacetic acid.**

The next day, the solution was vacuum-filtered through a Büchner funnel apparatus with Whatman qualitative filter paper. Insoluble, unreacted $Ni(OH)_2$ collected on the filter. The volume of the filtered NiEDDA solution was decreased through rotary evaporation, with vacuum, for several hours. A small amount of ethanol was added to form an azeotrope and decrease the boiling temperature.

The remaining NiEDDA solution was divided among several 50 mL Falcon tubes for freezing in dry ice. Once the NiEDDA solution had completely frozen, the NiEDDA was lyophilized for 48 hours until a fluffy light blue powder appeared. Following

lyophilization, the purity of the NiEDDA powder was verified using ultraviolet-visible (UV-Vis) and EPR spectroscopy, as discussed below.

**Verification of the Purity of the Synthesized NiEDDA.**

NiEDDA produces two unique peaks at 600 and 367 nm in UV-Vis absorbance spectra.[84] A NiEDDA buffer of approximately 200 mM NiEDDA, 100 mM KCl, and 50 mM Tris pH 7.8 was prepared and filtered through a 0.2 $\mu$M pore-size filter. The absorbance spectrum of the NiEDDA buffer was measured using a Cary UV-Vis Spectrometer with a 1 cm pathlength cuvette. Absorbance spectra were also recorded for $Ni(OH)_2$ in 100 mM KCl, 50 mM Tris pH 7.8 buffer and pure 100 mM KCl, 50 mM Tris pH 7.8 buffer (Figure AA2).

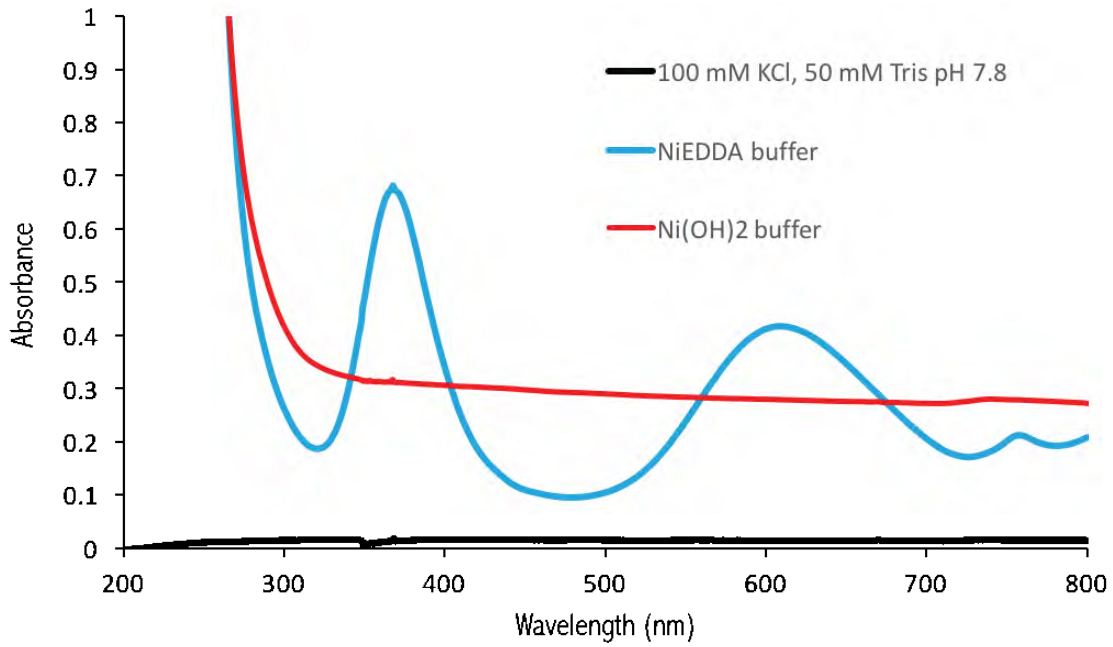


**Figure A2. The UV-Vis absorbance spectrum of synthesized NiEDDA. Samples were prepared as described in the text.**

The NiEDDA absorbance spectrum exhibits peaks at approximately 367 and 610 nm that are absent in the buffer and $Ni(OH)_2$ buffer solutions, suggesting that the synthesized NiEDDA is pure following filtering.

**Verification of the Paramagnetic Behavior of the Synthesized NiEDDA.**

Interaction between a nitroxide radical and paramagnetic relaxation agent results in an increase in the amount of power required for spin label saturation[43]. To verify the paramagnetic character of the newly synthesized NiEDDA, a power saturation was performed using aqueous 4-Hydroxy-2,2,6,6-tetramethylpiperidine 1-oxyl label (TEMPOL; Aldrich CAS 2226-96-2). A 100 $\mu$M solution of TEMPOL was prepared in 100 mM KCl, 50 mM Tris pH 7.8 buffer, and the natural relaxation rate of the label was measured over eight power levels in a gas-permeable TPX tube equilibrated with nitrogen (Figure A3). A 100 $\mu$M solution of TEMPOL was also prepared in 50 mM NiEDDA, 100 mM KCl, 50 mM Tris pH 7.8 buffer. Following equilibration in nitrogen gas, a power saturation experiment was performed over 16 power levels to measure the saturation of the spin label in the presence of NiEDDA (Figure A3).

The aqueous TEMPOL saturated in the presence of nitrogen but failed to saturate in NiEDDA buffer, confirming that the synthesized NiEDDA exhibited the paramagnetic properties required for further studies.

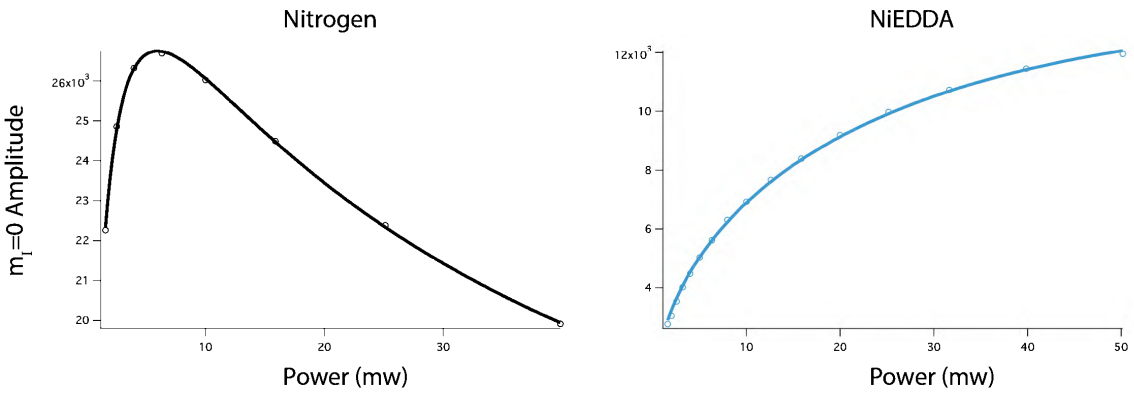


**Figure A3. The power saturation curves of 100 µM TEMPOL in the presence of nitrogen gas (left) and 50 mM NiEDDA (right).**
The graphs reveal that the aqueous spin label fails to saturate when NiEDDA is included as a paramagnetic relaxation agent. Power saturation experiments were collected over eight power levels in the presence of nitrogen and over 16 power levels in the presence of NiEDDA.

### Preparation of NiEDDA Buffer for Accessibility Studies.

Previous SDSL-EPR work on the M2 protein used 20 mM NiEDDA buffer for accessibility studies.[17,20] The membrane-facing and aqueous-exposed sides of the amphipathic helix exhibited differences in accessibility to NiEDDA; however, the magnitude of the difference was muted relative to the error in accessibility measurements.[17] This effect could result from the mobility of the amphipathic helix or shallow penetration of NiEDDA into the lipid bilayer. In order to increase the magnitude in the difference in NiEDDA accessibility of solvent-exposed and buried sites, we prepared 50 mM NiEDDA, 100 mM KCl, 50 mM Tris pH 7.8 buffer for use in these studies.

# Appendix B: TEV Protease Expression and Purification

## OVERVIEW: TEV PROTEASE

The tobacco etch virus (TEV) protease is commonly employed to cleave recombinant proteins containing engineered affinity tags. This cysteine protease is favored for its stringent specificity and ease of production in *E. coli* cells[119]. The widely circulating TEV protease expression vector pRK793 exists as a maltose-binding protein (MBP) fusion construct and harbors the S219V mutation, which minimizes autoinactivation. The MBP fusion facilitates proper folding of the protease and promotes solubility, thereby contributing to high expression yields. The fusion product self-cleaves to produce a TEV protease with N-terminal and C-terminal hexahistidine and polyarginine affinity tags, respectively[120].

Purification of MBP-$His_6$-TEV(S219V)-$Arg_5$ protease requires an immobilized metal affinity chromatography step to isolate the protein to homogeneity, followed by gel size exclusion chromatography to separate the MBP. The following protocol was adapted from methods described in *Tropea et al.*[120] and has been developed for Swarthmore College facilities.

## MATERIALS

### Expression Materials.

1. A glycerol stock of *E. coli* BL21(DE3) competent cells containing the pRK793 $His_6$-TEV(S219V)-$Arg_5$ protease expression vector.
2. Stocks of 100 mg/mL ampicillin in deionized water. The ampicillin stocks should be filtered prior to use and stored at -20°C.

3. Stocks of 1M isopropyl-β-D-thiogalactopyranoside (IPTG) in deionized water, filtered and stored at -20°C.
4. An autoclave with a slow-exhaust setting for preparing sterile media (see below).
5. A 100 mL stock solution of Miller's LB and 1000 mL of Miller's LB in a 2L baffle-bottom flask. Typically several liters of LB are used at a time due to the resource-intensiveness of preparing the Sephadex-75 column.
6. A temperature-controlled incubator with a shaking platform that can accommodate several 2L baffle-bottom flasks. We use New Brunswick Scientific C25 and Innova® 42 incubators.
7. A spectrophotometer for measuring the optical density at 600 nm ($OD_{60}$) of bacterial cultures. We use an Amerscham Biosciences Ultrospec10 cell density meter.
8. A medium-speed centrifuge for pelleting cells, e.g. Thermo Scientific Sorvall Legend RT+.

**Purification Materials.**

1. TEV lysis buffer: 20 mM Tris pH 8, 500 mM NaCl. 1 mg/mL DNase I, 20 mM $MgCl_2$, and 5 mM $CaCl_2$ should be added immediately before use.
2. TEV wash buffer: 20 mM Tris pH 8, 500 mM NaCl, 25 or 50 mM imidazole (see section A3.3 for details).
3. TEV elution buffer: 20 mM Tris pH 8, 500 mM NaCl, 400 mM imidazole
4. S-75 buffer: 25 mM $Na_2HPO_4/NaH_2PO_4$ pH 8, 200 mM NaCl, 10% glycerol, 2 mM EDTA, 10 mM DTT

5. A stock of 1M Dithiothreitol (DTT), stored at -20°C.
6. A stock of 0.5 M Ethylenediaminetetraacetic acid (EDTA) pH 8.
7. A cell disruption device to homogenize TEV-expressing BL21(DE3) cell lysates. We break cells for large-scale purifications using the M-110Y high-pressure pneumatic homogenizer (Microfluidics, MA, USA).
8. A high-speed centrifuge. We use a Thermo Scientific Sorvall RC6+.
9. Ni-NTA or Ni-IDA resin.
10. A spectrophotometer calibrated to record absorbance at 280 (A280). Our lab is equipped with a Thermo Scientific NanoDrop 2000.
11. ÄKTA Purification Basic 10 chromatography system (Amersham Biosciences, NJ, USA).
12. A Superdex-75 gel filtration column.
13. Degassed, filtered Millipore water and 20% ethanol.
14. Amicon Stirred Cells for pressure-based sample concentration. TEV protease is liable to precipitate when centrifugal filters are used.
15. A Dewar flask filled with liquid nitrogen. Please consult with a research advisor about departmental safety procedures when dispensing and handling liquid nitrogen.

**TEV PROTEASE OVEREXPRESSION**

A starter culture of 5 mL LB supplemented with 100 $\mu$g/mL ampicillin was inoculated directly from a glycerol stock of *E. coli* BL21(DE3) competent cells containing the pRK793 $His_6$-TEV(S219V)-$Arg_5$ protease expression vector. The culture was grown in 37°C overnight with shaking at 250 rpm. The next morning, the 1 mL of

starter culture was transferred to 1 L of LB media containing 100 $\mu$g/mL ampicillin. Cultures were induced with 1 mM IPTG at an OD of ~0.6 (approximately four hours). The induced cells were grown for four hours at 30°C before harvest. The cultures were divided into 750 mL centrifuge tubes and were pelleted at 4000 rpm for 30 minutes at 4°C. In total, six cell pellets from three liters of growth were recovered and stored at -80°C.

### TEV PROTEASE PURIFICATION

The entire purification process is ideally performed in one day, as TEV precipitates easily. The Sephadex-75 size exclusion column must be equilibrated prior to use. The column was equilibrated in 1 L of degassed, filtered Millipore water and 20% ethanol (degassed five minutes using an in-house vacuum pump) the night before the purification. In the hours leading up to the size exclusion step, the column was equilibrated in degassed, filtered S-75 buffer.

The cell pellets were resuspended in 20 mL of TEV lysis buffer per liter of growth and were stored on ice. The suspension was passed through a M-110Y high-pressure pneumatic homogenizer; instructions for this device are located in the Biochemistry Resource Room. The cell lysate was collected in centrifuge tubes and was centrifuged at 14000 rpm for 30 minutes at 4°C (9 acc/4 dec). The supernatant containing the soluble fraction was applied to two Ni-IDA columns with 2 mL resin bed volumes that had been pre-equilibrated in five column-volumes of Millipore water and lysis buffer. Approximately 65 mL of supernatant was applied to the two columns and was eluted. The columns were washed with four column volumes of 25 mM imidazole wash buffer and with three column volumes of 50 mM imidazole wash buffer, until the protein

A280 stabilized. The His-tagged protein was eluted with one column volume fractions of elution buffer. Elution fractions were pooled based on purity monitored by SDS-PAGE.

The pooled elution fractions were concentrated to approximately 5 mL, the loading volume of the S-75 column, using a stirred pressure concentration cell. The concentrated samples were passed through a 0.2 $\mu$m filter to remove particulates, though in the future the solution should be centrifuged at 14000 rpm in a minicentrifuge to remove any precipitation. The column sample was then applied to the pre-equilibrated Sephadex-75 column. Fractions with high A280 peaks were monitored by SDS-PAGE and were pooled accordingly. The pooled fractions were concentrated to a final concentration of 0.62 mg/mL and were flash-frozen in liquid nitrogen and stored at -80°C.

The yield for this trial was 1.55 mg ($\varepsilon_{280}$ = 1.19 mg/mL), which is lower than expected, although the purity of the protein was high (Figure A??). Purified TEV protease should be stored at concentrations lower than 1 mg/mL to minimize precipitation. Often this requires diluting the pooled S-75 fractions to 0.98 mg/mL.

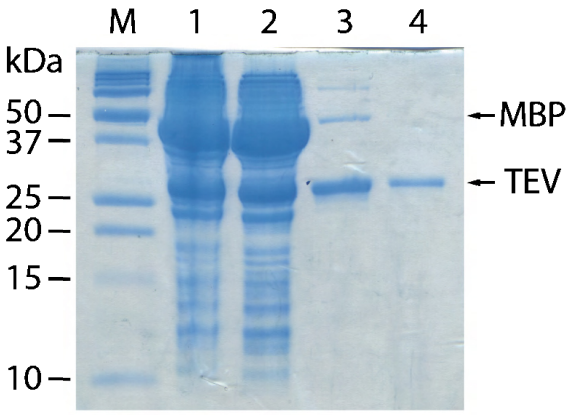


**Figure B1. SDS-PAGE evidence for the purity of $His_6$-TEV(S219V)-$Arg_5$ protease used in these studies.**
M: molecular weight marker. Lane 1: Cell pellet lysate. Lane 2: Soluble lysate extract following centrifugation. Lane 3: Pooled elution fractions following Ni-IDA affinity purification. Lane 4: Pooled fractions following S-75 size exclusion chromatography. The bands corresponding to TEV protease (26 kDa) and MBP (42.5 kDa) are indicated.

## REMOVAL OF THE HEXAHISTIDINE TAG

Previous SDSL-EPR studies of full-length M2 employed constructs containing a C-terminal hexahistidine tag preceded by a Factor Xa cleavage site (IE / GR). Given the propensity of Factor Xa protease for off-target cleavage[119], this hexahistidine tag was not removed prior to reconstitution and data collection[18]. Extending spectroscopic studies towards the C-terminal end of the protein necessitated removal of the tag in order to minimize topological artifacts potentially introduced by polyhistidine interactions. A new M2 construct with an N-terminal hexahistidine tag followed by a TEV protease cleavage site (ENLYFQ / SNA) was therefore generated. TEV cleavage liberated the construct from a 2483.66 Da, 21-residue tag with the sequence MHHHHHHSSGVDLGTENLYFQ. Three non-endogenous residues, SNA, remained on the N-terminal end of the peptide following cleavage.

Because TEV protease contains a catalytic cysteine residue[119], the cleavage reaction had to be carried out before the covalent attachment of the spin label. Therefore, TEV protease was added directly to the M2 fractions eluted from the nickel resin (section A2). The fractions were additionally supplemented with 2 mM DTT to provide reducing power. The efficiency of TEV protease cleavage decreases in OG detergent, although the effect appears to depend largely on the nature of the tagged-protein-micelle complexes formed, rather than inactivation of the TEV itself[121]. To increase cleavage efficiency, 0.62 mg/mL TEV was added 1:20 to the protein solution by weight. The reaction was incubated overnight at room temperature.

The cleavage reaction products were passed through a PD-10 Desalting Column (GE Healthcare, IL, USA) to remove imidazole and DTT prior to the Ni-NTA clean-up step (desalting buffer: 50 mM Tris pH 8 and 30 mM OG). Next, nickel resin pre-

equilibrated in desalting buffer was added directly to the cleavage products to remove TEV protease and any uncleaved proteins. Approximately 100 $\mu$L of resin was added per 4 mg of protein. Following a 10-minute nutation step to facilitate binding, the samples were centrifuged at 4000 rpm for 10 minutes. The supernatant, which should contain soluble, cleaved M2, was collected and saved for spin labeling and downstream analysis.

# Appendix C: Parameters, Data Processing and Error Analysis

## DETERMINATION OF M2 SPIN-LABELING EFFICIENCY

The amount of spin-labeled M2 was calculated by double-integrating the EPR resonances of spin-labeled protein stock in OG micelles relative to the signal from the following 4-Hydroxy-TEMPO standard curve:

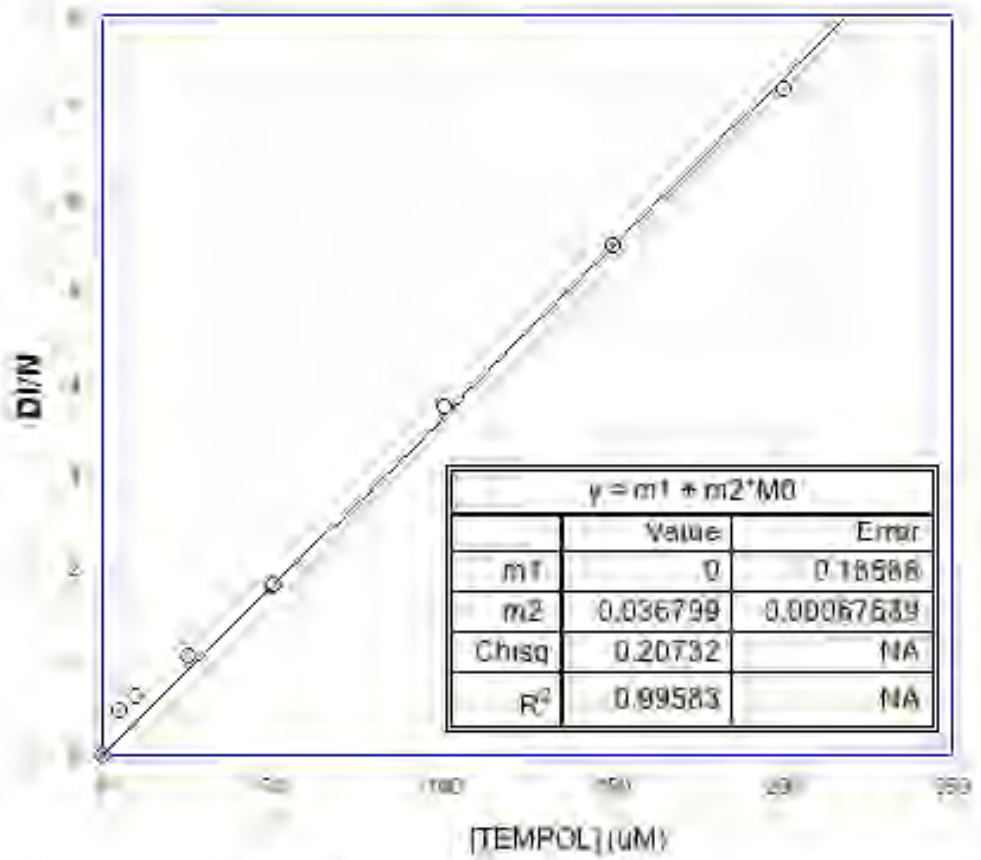


**Figure C1. The TEMPO standard curve used to calculate the concentration of spin-labeled M2.**
At spin-labeled protein concentrations < 25 μM, the calibration curve under-estimates the amount of spin label present.

From a measured DI/N, the following equation can be used to calculate the amount of spin label in solution:

$$[Spin\ label]\ (in\ \mu M) = \frac{1}{0.0368} \times DI/N = 27.2 \times DI/N \quad (1)$$

To match the sample conditions used to establish the calibration curve, approximately 30 $\mu$L of a spin-labeled protein solution in OG was drawn into a 50 $\mu$L disposable micropipette (VWR International, Radnor, PA) and sealed with wax. The CW EPR spectrum was measured using the following experimental parameters: Center field: 3480 G, Sweep width: 150 G, Receiver Gain: $1x10^4$, Frequency: 9.795 GHz, Power: 2 mW (Attenuation 20 dB), Modulation frequency: 100 kHz, Modulation Amplitude: 1.0G, Resolution in X: 1024, Sweep time: 41.943 (Conversion Time: 40.960 ms, Time Constant: 5.120 ms), Number of scans: 29.

The spin labeling efficiency was calculated as the ratio of the spin label concentration to the concentration of protein determined from the protein A280:

$$Spin\ labeling\ efficiency = \frac{[SL]}{[Protein\ conc.\ from\ A280]} \times 100\% \quad (2)$$

The extinction coefficients used to calculate the protein concentration from the A280 are documented in a later section.

## ERROR ANALYSIS

If the measurements of two values $x$ and $y$ are independent and subject only to random uncertainties (that is, their uncertainties $\delta x$ and $\delta y$ are described by a Gaussian distribution), then the uncertainty $\delta q$ of the summed value $q = x + y$ is[122]

$$\delta q = \sqrt{(\delta x)^2 + (\delta y)^2} \quad (3)$$

To calculate the error associated with an accessibility parameter, we use the error measured from the 95% confidence interval of the fit of the power saturation curve for each relaxation agent ($R_x$):

$$\Delta P_{\frac{1}{2}}(R_x)\ Error = \sqrt[2]{(Error\ P_{\frac{1}{2}}(R_x))^2 + (Error\ P_{\frac{1}{2}}(N_2))^2} \quad (4)$$

Uncertainty in measurements of the central linewidth ($\Delta H_0$) arise from uncertainties in the Gauss values of the central peak maximum ($H_{max}$) and minimum ($H_{min}$) due to "flat" or "jagged" peaks, e.g. as shown in Figure 2. If the peak ends in a perfect point, then the associated error in the measurement is zero.

Here, we calculate the uncertainty associated with the central linewidth as

$$\delta\Delta H = \sqrt{(\delta H_{max})^2 + (\delta H_{min})^2} \quad (5)$$

Because the inverse central linewidth $\Delta H_0^{-1}$ comes directly from $\Delta H_0$, the two values share the same fractional uncertainty[122]

$$fractional\ uncertainty = \frac{\delta x}{|x|} \quad (6)$$

Therefore, the uncertainty in $\Delta H_0^{-1}$ is calculated as

$$\delta\Delta H_0^{-1} = \frac{\delta\Delta H_0}{\Delta H_0} \times \Delta H_0^{-1} \quad (7)$$

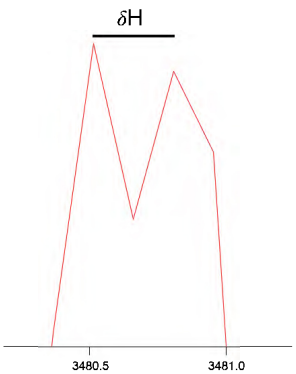


**Figure C2. The uncertainty ($\delta H$) associated with identifying the Gauss value of the central peak maximum or minimum.**

## PHYSICAL PARAMETERS OF CONSTRUCTS PREPARED FOR THIS THESIS

### The Physical Parameters of M2 50-70 Cysteine Mutants.

**Table S1. M2 single-cysteine constructs 50-70.**
Engineered cysteine substitutions are underlined. Expected non-MTSL labeled molecular weights and extinction coefficients were calculated using the ExPASy ProtParam tool.[123] All constructs contain the mutations W15F, C17S, C19S, and C50S in addition to a C-terminal hexahistidine tag with an IE/GR cleavage site. The pentaAla constructs contain the additional mutations F47A, F48A, I51A, Y52A, and F55A.

| Construct Name | Amino Acid Sequence | MW (Da) | $\varepsilon_{280}$ ($M^{-1}cm^{-1}$) |
|---|---|---|---|
| M2 cysteineless | MSLLTEVETPIRNEFGSRSNDSSDPLVVAASIIGILHLILWILDRLFFKSIYRFF EHGLKRGPSTEGVPESMREEYRKEQQSAVDADDSHFVSIEGRHHHHHH | 11892.33 | 8480 |
| M2 L43C | MSLLTEVETPIRNEFGSRSNDSSDPLVVAASIIGILHLILWI<u>C</u>DRLFFKSIYRFF EHGLKRGPSTEGVPESMREEYRKEQQSAVDADDSHFVSIEGRHHHHHH | 11882.30 | 8480 |
| M2 C50 | MSLLTEVETPIRNEFGSRSNDSSDPLVVAASIIGILHLILWILDRLFFK<u>C</u>IYRFF EHGLKRGPSTEGVPESMREEYRKEQQSAVDADDSHFVSIEGRHHHHHH | 11908.39 | 8480 |
| M2 I51C | MSLLTEVETPIRNEFGSRSNDSSDPLVVAASIIGILHLILWILDRLFFKS<u>C</u>YRFF EHGLKRGPSTEGVPESMREEYRKEQQSAVDADDSHFVSIEGRHHHHHH | 11882.30 | 8480 |
| M2 Y52C | MSLLTEVETPIRNEFGSRSNDSSDPLVVAASIIGILHLILWILDRLFFKSI<u>C</u>RFF EHGLKRGPSTEGVPESMREEYRKEQQSAVDADDSHFVSIEGRHHHHHH | 11832.29 | 6990 |
| M2 R53C | MSLLTEVETPIRNEFGSRSNDSSDPLVVAASIIGILHLILWILDRLFFKSIY<u>C</u>FF EHGLKRGPSTEGVPESMREEYRKEQQSAVDADDSHFVSIEGRHHHHHH | 11839.28 | 8480 |
| M2 F54C | MSLLTEVETPIRNEFGSRSNDSSDPLVVAASIIGILHLILWILDRLFFKSIYR<u>C</u>F EHGLKRGPSTEGVPESMREEYRKEQQSAVDADDSHFVSIEGRHHHHHH | 11848.29 | 8480 |
| M2 F55C | MSLLTEVETPIRNEFGSRSNDSSDPLVVAASIIGILHLILWILDRLFFKSIYRF<u>C</u> EHGLKRGPSTEGVPESMREEYRKEQQSAVDADDSHFVSIEGRHHHHHH | 11848.29 | 8480 |
| M2 E56C | MSLLTEVETPIRNEFGSRSNDSSDPLVVAASIIGILHLILWILDRLFFKSIYRFF <u>C</u>HGLKRGPSTEGVPESMREEYRKEQQSAVDADDSHFVSIEGRHHHHHH | 11866.35 | 8480 |
| M2 H57C | MSLLTEVETPIRNEFGSRSNDSSDPLVVAASIIGILHLILWILDRLFFKSIYRFF E<u>C</u>GLKRGPSTEGVPESMREEYRKEQQSAVDADDSHFVSIEGRHHHHHH | 11858.32 | 8480 |
| M2 G58C | MSLLTEVETPIRNEFGSRSNDSSDPLVVAASIIGILHLILWILDRLFFKSIYRFF EH<u>C</u>LKRGPSTEGVPESMREEYRKEQQSAVDADDSHFVSIEGRHHHHHH | 11938.41 | 8480 |
| M2 L59C | MSLLTEVETPIRNEFGSRSNDSSDPLVVAASIIGILHLILWILDRLFFKSIYRFF EHG<u>C</u>KRGPSTEGVPESMREEYRKEQQSAVDADDSHFVSIEGRHHHHHH | 11882.30 | 8480 |
| M2 K60C | MSLLTEVETPIRNEFGSRSNDSSDPLVVAASIIGILHLILWILDRLFFKSIYRFF EHGL<u>C</u>RGPSTEGVPESMREEYRKEQQSAVDADDSHFVSIEGRHHHHHH | 11867.29 | 8480 |
| M2 R61C | MSLLTEVETPIRNEFGSRSNDSSDPLVVAASIIGILHLILWILDRLFFKSIYRFF EHGLK<u>C</u>GPSTEGVPESMREEYRKEQQSAVDADDSHFVSIEGRHHHHHH | 11839.28 | 8480 |
| M2 G62C | MSLLTEVETPIRNEFGSRSNDSSDPLVVAASIIGILHLILWILDRLFFKSIYRFF EHGLKR<u>C</u>PSTEGVPESMREEYRKEQQSAVDADDSHFVSIEGRHHHHHH | 11938.41 | 8480 |

| Construct Name | Amino Acid Sequence | MW (Da) | $\varepsilon_{280}$ ($M^{-1}cm^{-1}$) |
|---|---|---|---|
| M2 P63C | MSLLTEVETPIRNEFGSRSNDSSDPLVVAASIIGILHLILWILDRLFFKSIYRFF EHGLKRGCSTEGVPESMREEYRKEQQSAVDADDSHFVSIEGRHHHHHH | 11898.35 | 8480 |
| M2 S64C | MSLLTEVETPIRNEFGSRSNDSSDPLVVAASIIGILHLILWILDRLFFKSIYRFF EHGLKRGPCTEGVPESMREEYRKEQQSAVDADDSHFVSIEGRHHHHHH | 11908.39 | 8480 |
| M2 T65C | MSLLTEVETPIRNEFGSRSNDSSDPLVVAASIIGILHLILWILDRLFFKSIYRFF EHGLKRGPSCEGVPESMREEYRKEQQSAVDADDSHFVSIEGRHHHHHH | 11894.36 | 8480 |
| M2 E66C | MSLLTEVETPIRNEFGSRSNDSSDPLVVAASIIGILHLILWILDRLFFKSIYRFF EHGLKRGPSTCGVPESMREEYRKEQQSAVDADDSHFVSIEGRHHHHHH | 11866.35 | 8480 |
| M2 G67C | MSLLTEVETPIRNEFGSRSNDSSDPLVVAASIIGILHLILWILDRLFFKSIYRFF EHGLKRGPSTECVPESMREEYRKEQQSAVDADDSHFVSIEGRHHHHHH | 11938.41 | 8480 |
| M2 V68C | MSLLTEVETPIRNEFGSRSNDSSDPLVVAASIIGILHLILWILDRLFFKSIYRFF EHGLKRGPSTEGCPESMREEYRKEQQSAVDADDSHFVSIEGRHHHHHH | 11896.33 | 8480 |
| M2 P69C | MSLLTEVETPIRNEFGSRSNDSSDPLVVAASIIGILHLILWILDRLFFKSIYRFF EHGLKRGPSTEGVCESMREEYRKEQQSAVDADDSHFVSIEGRHHHHHH | 11898.35 | 8480 |
| M2 E70C | MSLLTEVETPIRNEFGSRSNDSSDPLVVAASIIGILHLILWILDRLFFKSIYRFF EHGLKRGPSTEGVPCSMREEYRKEQQSAVDADDSHFVSIEGRHHHHHH | 11866.35 | 8480 |

**The Physical Parameters of M2 71-80 Cysteine Mutants.**

Plasmid encoding full-length M2 (A/Udorn/72) in a cysteine-free background was kindly provided by Bruk Mensa (University of California, San Francisco). This construct additionally contains the mutation W15F and an N-terminal hexahistidine tag followed by the TEV protease cleavage sequence ENLYFQ / SNA. Single-cysteine mutations were introduced into the M2(W15F, C17S, C19S, C50S) sequence using a PCR-based QuikChange Lightning Site-Directed Mutagenesis Kit according to the manufacturer's protocol (Agilent Technologies, CA, USA). All constructs were verified using fluorescence-based automated sequencing services (Genewiz Inc., NJ, USA). Table C2 summarizes construct sequences and select physical parameters. The construct containing the N-terminal $His_6$-tag is referred to as His-M2. Following TEV cleavage, the construct

contains an N-terminal tripeptide SNA overhang. This construct is referred to as SNA-M2.

**Table C2. M2 single-cysteine constructs 71-80.**
Engineered cysteine mutations are underlined. Expected non-MTSL labeled molecular weights and extinction coefficients were calculated using the ExPASy ProtParam tool[123].

| Construct Name | Amino Acid Sequence | MW (Da) | $\varepsilon_{280}$ ($M^{-1}cm^{-1}$) |
|---|---|---|---|
| A/Udorn/72 | MSLLTEVETPIRNE G R NDSSDPLVVAASIIGILHLILWILDRLF FK IYRFFEHGLKRGPSTEGVPESMREEYRKEQQSAVDADDSH FVSIELE | 10943.46 | 13980 |
| His-M2 WT (W15F, C17S, C19S, C50S) | MHHHHHHSSGVDLGTENLYFQSNAMSLLTEVETPIRNEFGSRS NDSSDPLVVAASIIGILHLILWILDRLFFKSIYRFFEHGLKRGPSTE GVPESMREEYRKEQQSAVDADDSHFVSIELE | 13836.42 | 9970 |
| SNA-M2 WT (W15F, C17S, C19S, C50S) | SNAMSLLTEVETPIRNEFGSRSNDSSDPLVVAASIIGILHLILWILD RLFFKSIYRFFEHGLKRGPSTEGVPESMREEYRKEQQSAVDAD DSHFVSIELE | 11370.78 | 8480 |
| His-M2 S71C | MHHHHHHSSGVDLGTENLYFQSNAMSLLTEVETPIRNEFGSRS NDSSDPLVVAASIIGILHLILWILDRLFFKSIYRFFEHGLKRGPSTE GVPE**C**MREEYRKEQQSAVDADDSHFVSIELE | 13852.48 | 9970 |
| SNA-M2 S71C | SNAMSLLTEVETPIRNEFGSRSNDSSDPLVVAASIIGILHLILWILD RLFFKSIYRFFEHGLKRGPSTEGVPE**C**MREEYRKEQQSAVDAD DSHFVSIELE | 11386.84 | 8480 |
| His-M2 M72C | MHHHHHHSSGVDLGTENLYFQSNAMSLLTEVETPIRNEFGSRS NDSSDPLVVAASIIGILHLILWILDRLFFKSIYRFFEHGLKRGPSTE GVPES**C**REEYRKEQQSAVDADDSHFVSIELE | 13808.37 | 9970 |
| SNA-M2 S72C | SNAMSLLTEVETPIRNEFGSRSNDSSDPLVVAASIIGILHLILWILD RLFFKSIYRFFEHGLKRGPSTEGVPES**C**REEYRKEQQSAVDADD SHFVSIELE | 11342.72 | 8480 |
| His-M2 R73C | MHHHHHHSSGVDLGTENLYFQSNAMSLLTEVETPIRNEFGSRS NDSSDPLVVAASIIGILHLILWILDRLFFKSIYRFFEHGLKRGPSTE GVPESM**C**EEYRKEQQSAVDADDSHFVSIELE | 13783.37 | 9970 |
| SNA-M2 R73C | SNAMSLLTEVETPIRNEFGSRSNDSSDPLVVAASIIGILHLILWILD RLFFKSIYRFFEHGLKRGPSTEGVPESM**C**EEYRKEQQSAVDAD DSHFVSIELE | 11317.73 | 8480 |
| His-M2 RE74C | MHHHHHHSSGVDLGTENLYFQSNAMSLLTEVETPIRNEFGSRS NDSSDPLVVAASIIGILHLILWILDRLFFKSIYRFFEHGLKRGPSTE GVPESMR**C**EYRKEQQSAVDADDSHFVSIELE | 13810.45 | 9970 |
| SNA-M2 E74C | SNAMSLLTEVETPIRNEFGSRSNDSSDPLVVAASIIGILHLILWILD RLFFKSIYRFFEHGLKRGPSTEGVPESMR**C**EYRKEQQSAVDAD DSHFVSIELE | 11344.80 | 8480 |
| His-M2 E75C | MHHHHHHSSGVDLGTENLYFQSNAMSLLTEVETPIRNEFGSRS NDSSDPLVVAASIIGILHLILWILDRLFFKSIYRFFEHGLKRGPSTE GVPESMRE**C**YRKEQQSAVDADDSHFVSIELE | 13810.45 | 9970 |
| SNA-M2 E75C | SNAMSLLTEVETPIRNEFGSRSNDSSDPLVVAASIIGILHLILWILD RLFFKSIYRFFEHGLKRGPSTEGVPESMRE**C**YRKEQQSAVDAD DSHFVSIELE | 11344.80 | 8480 |
| His-M2 Y76C | MHHHHHHSSGVDLGTENLYFQSNAMSLLTEVETPIRNEFGSRS NDSSDPLVVAASIIGILHLILWILDRLFFKSIYRFFEHGLKRGPSTE GVPESMREE**C**RKEQQSAVDADDSHFVSIELE | 13776.39 | 8480 |
| SNA-M2 Y76C | SNAMSLLTEVETPIRNEFGSRSNDSSDPLVVAASIIGILHLILWILD RLFFKSIYRFFEHGLKRGPSTEGVPESMREE**C**RKEQQSAVDAD DSHFVSIELE | 11310.74 | 6990 |

| Construct Name | Amino Acid Sequence | MW (Da) | $\varepsilon_{280}$ ($M^{-1}cm^{-1}$) |
|---|---|---|---|
| His-M2 R77C | MHHHHHHSSGVDLGTENLYFQSNAMSLLTEVETPIRNEFGSRS NDSSDPLVVAASIIGILHLILWILDRLFFKSIYRFFEHGLKRGPSTE GVPESMREEY**C**KEQQSAVDADDSHFVSIELE | 13783.37 | 9970 |
| SNA-M2 R77C | SNAMSLLTEVETPIRNEFGSRSNDSSDPLVVAASIIGILHLILWILD RLFFKSIYRFFEHGLKRGPSTEGVPESMREEY**C**KEQQSAVDAD DSHFVSIELE | 11317.73 | 8480 |
| His-M2 K78C | MHHHHHHSSGVDLGTENLYFQSNAMSLLTEVETPIRNEFGSRS NDSSDPLVVAASIIGILHLILWILDRLFFKSIYRFFEHGLKRGPSTE GVPESMREEYR**C**EQQSAVDADDSHFVSIELE | 13811.39 | 9970 |
| SNA-M2 K78C | SNAMSLLTEVETPIRNEFGSRSNDSSDPLVVAASIIGILHLILWILD RLFFKSIYRFFEHGLKRGPSTEGVPESMREEYR**C**EQQSAVDAD DSHFVSIELE | 11345.74 | 8480 |
| His-M2 E79C | MHHHHHHSSGVDLGTENLYFQSNAMSLLTEVETPIRNEFGSRS NDSSDPLVVAASIIGILHLILWILDRLFFKSIYRFFEHGLKRGPSTE GVPESMREEYRK**C**QQSAVDADDSHFVSIELE | 13810.45 | 9970 |
| SNA-M2 E79C | SNAMSLLTEVETPIRNEFGSRSNDSSDPLVVAASIIGILHLILWILD RLFFKSIYRFFEHGLKRGPSTEGVPESMREEYRK**C**QQSAVDAD DSHFVSIELE | 11344.80 | 8480 |
| His-M2 Q80C | MHHHHHHSSGVDLGTENLYFQSNAMSLLTEVETPIRNEFGSRS NDSSDPLVVAASIIGILHLILWILDRLFFKSIYRFFEHGLKRGPSTE GVPESMREEYRKE**C**QSAVDADDSHFVSIELE | 13811.43 | 9970 |
| SNA-M2 Q80C | SNAMSLLTEVETPIRNEFGSRSNDSSDPLVVAASIIGILHLILWILD RLFFKSIYRFFEHGLKRGPSTEGVPESMREEYRKE**C**QSAVDAD DSHFVSIELE | 11345.78 | 8480 |

**The Physical Parameters of pentaAla Cysteine Mutants.**

**Table C3. PentaAla construct physical parameters.**
Engineered cysteine substitutions are underlined. Expected non-MTSL labeled molecular weights and extinction coefficients were calculated using the ExPASy ProtParam tool.[123] All constructs contain the mutations W15F, C17S, C19S, and C50S in addition to a C-terminal hexahistidine tag with an IE/GR cleavage site. The pentaAla constructs contain the additional mutations F47A, F48A, I51A, Y52A, and F55A.

| Construct Name | Amino Acid Sequence | MW (Da) | $\varepsilon_{280}$ ($M^{-1}cm^{-1}$) |
|---|---|---|---|
| pentaAla cysteineless | MSLLTEVETPIRNEFGSRSNDSSDPLVVAASIIGILHLILWILDRL*AAKSAA* RF*A*EHGLKRGPSTEGVPESMREEYRKEQQSAVDADDSHFVSIEGRHHH HHH | 11529.85 | 6990 |
| pentaAla L43C | MSLLTEVETPIRNEFGSRSNDSSDPLVVAASIIGILHLILWI**C**DRL*AAKSAA* RF*A*EHGLKRGPSTEGVPESMREEYRKEQQSAVDADDSHFVSIEGRHHH HHH | 11519.83 | 6990 |
| pentaAla H57C | MSLLTEVETPIRNEFGSRSNDSSDPLVVAASIIGILHLILWILDRL*AAKSAA* RF*A*E**C**GLKRGPSTEGVPESMREEYRKEQQSAVDADDSHFVSIEGRHHH HHH | 11495.85 | 6990 |
| pentaAla L59C | MSLLTEVETPIRNEFGSRSNDSSDPLVVAASIIGILHLILWILDRL*AAKSAA* RF*A*EHG**C**KRGPSTEGVPESMREEYRKEQQSAVDADDSHFVSIEGRHH HHHH | 11519.83 | 6990 |
| pentaAla V68C | MSLLTEVETPIRNEFGSRSNDSSDPLVVAASIIGILHLILWILDRL*AAKSAA* RF*A*EHGLKRGPSTEG**C**PESMREEYRKEQQSAVDADDSHFVSIEGRHHH HHH | 11533.86 | 6990 |

## POWER SATURATION LEVELS

**Table C4. Power levels used for power saturation experiments in the presence of nitrogen gas and no relaxation agent.**

| Attenuation | Power (mW) |
|---|---|
| 21 | 1.581 |
| 19 | 2.514 |
| 17 | 3.985 |
| 15 | 6.315 |
| 13 | 10.01 |
| 11 | 15.86 |
| 9 | 25.14 |
| 7 | 39.85 |

**Table C5. Power levels used for power saturation experiments with low accessibility to fast-relaxing paramagnetic reagents.**

| Attenuation | Power (mW) |
|---|---|
| 21 | 1.581 |
| 20 | 1.997 |
| 19 | 2.514 |
| 18 | 3.165 |
| 17 | 3.985 |
| 16 | 5.016 |
| 15 | 6.315 |
| 14 | 7.95 |
| 13 | 10.01 |
| 12 | 12.6 |
| 11 | 15.86 |
| 10 | 19.97 |
| 9 | 25.14 |
| 8 | 31.65 |
| 7 | 39.85 |
| 6 | 50.16 |

**Table C6. Power levels used for power saturation experiments with high accessibility to fast-relaxing paramagnetic reagents.**

| Attenuation | Power (mW) |
|---|---|
| 20 | 1.997 |
| 19 | 2.514 |
| 18 | 3.165 |
| 17 | 3.985 |
| 16 | 5.016 |
| 15 | 6.315 |
| 14 | 7.95 |
| 13 | 10.01 |
| 12 | 12.6 |
| 11 | 15.86 |
| 10 | 19.97 |
| 9 | 25.14 |
| 8 | 31.65 |
| 7 | 39.85 |
| 6 | 50.16 |
| 5 | 63.31 |
| 4 | 79.7 |
| 3 | 100.3 |
| 2 | 126.3 |

# References

(1) Lina, B. (2008) History of Influenza Pandemics, in *Paleomicrobiology: Past Human Infections* (Raoult, D., and Drancourt, M., Eds.) 1st ed., pp 199–211. Springer.
(2) Krammer, F., and Palese, P. (2015) Advances in the development of influenza virus vaccines. *Nat. Rev. Drug Discov. 14*, 167–182.
(3) Rossman, J. S., and Lamb, R. A. (2010) Swine-origin Influenza Virus and the 2009 Pandemic. *Am. J. Respir. Crit. Care Med. 181*, 295–296.
(4) Schmitt, A. P., and Lamb, R. A. (2005) Influenza virus assembly and budding at the viral budozone. *Adv. Virus Res. 64*, 383–416.
(5) Samji, T. (2009) Influenza A: understanding the viral life cycle. *Yale J. Biol. Med. 82*, 153–9.
(6) Klenk, H.-D., Rott, R., and Becht, H. (1972) On the structure of the influenza virus envelope. *Virology 47*, 579–591.
(7) Gerl, M. J., Sampaio, J. L., Urban, S., Kalvodova, L., Verbavatz, J.-M., Binnington, B., Lindemann, D., Lingwood, C. A., Shevchenko, A., Schroeder, C., and Simons, K. (2012) Quantitative analysis of the lipidomes of the influenza virus envelope and MDCK cell apical membrane. *J. Cell Biol. 196*, 213–21.
(8) Veit, M., and Thaa, B. (2011) Association of influenza virus proteins with membrane rafts. *Adv. Virol. 2011*, 370606.
(9) Nayak, D. P., Balogun, R. A., Yamada, H., Zhou, Z. H., and Barman, S. (2009) Influenza virus morphogenesis and budding. *Virus Res. 143*, 147–161.
(10) Rossman, J. S., and Lamb, R. A. (2011) Influenza virus assembly and budding. *Virology 411*, 229–236.
(11) Rossman, J. S., Jing, X. H., Leser, G. P., and Lamb, R. A. (2010) Influenza Virus M2 Protein Mediates ESCRT-Independent Membrane Scission. *Cell 142*, 902–913.
(12) Rossman, J. S., Jing, X. H., Leser, G. P., Balannik, V., Pinto, L. H., and Lamb, R. A. (2010) Influenza Virus M2 Ion Channel Protein Is Necessary for Filamentous Virion Formation. *J. Virol. 84*, 5078–5088.
(13) Nieva, J. L., Madan, V., and Carrasco, L. (2012) Viroporins: structure and biological functions. *Nat. Rev. Microbiol. 10*, 563–574.
(14) Pinto, L. H., and Lamb, R. A. (2006) The M2 proton channels of influenza A and B viruses. *J. Biol. Chem. 281*, 8997–9000.
(15) Ma, C., Polishchuk, A. L., Ohigashi, Y., Stouffer, A. L., Schön, A., Magavern, E., Jing, X., Lear, J. D., Freire, E., Lamb, R. A., DeGrado, W. F., and Pinto, L. H. (2009) Identification of the functional core of the influenza A virus A/M2 proton-selective ion channel. *Proc. Natl. Acad. Sci. U. S. A. 106*, 12283–8.
(16) Influenza (Seasonal). World Health Organization.
(17) Nguyen, P. A., Soto, C. S., Polishchuk, A., Caputo, G. A., Tatko, C. D., Ma, C. L., Ohigashi, Y., Pinto, L. H., DeGrado, W. F., and Howard, K. P. (2008) pH-induced conformational change of the influenza M2 protein C-terminal domain. *Biochemistry 47*, 9934–9936.
(18) Huang, S., Green, B., Thompson, M., Chen, R., Thomaston, J., DeGrado, W. F., and Howard, K. P. (2015) C-terminal juxtamembrane region of full-length M2 protein forms a membrane surface associated amphipathic helix. *Protein Sci. 24*, 426–429.

(19) Sharma, M., Yi, M., Dong, H., Qin, H., Peterson, E., Busath, D. D., Zhou, H.-X., and Cross, T. A. (2010) Insight into the Mechanism of the Influenza A Proton Channel from a Structure in a Lipid Bilayer. *Science (80-. ). 330*, 509–512.
(20) Kim, S. S., Upshur, M. A., Saotome, K., Sahu, I. D., McCarrick, R. M., Feix, J. B., Lorigan, G. A., and Howard, K. P. (2015) Cholesterol-Dependent Conformational Exchange of the C-Terminal Domain of the Influenza A M2 Protein. *Biochemistry 54*, 7157–7167.
(21) Thomaston, J. L., Nguyen, P. A., Brown, E. C., Upshur, M. A., Wang, J., DeGrado, W. F., and Howard, K. P. (2013) Detection of drug-induced conformational change of a transmembrane protein in lipid bilayers using site-directed spin labeling. *Protein Sci. 22*, 65–73.
(22) Duong-Ly, K. C., Nanda, V., Degrado, W. F., and Howard, K. P. (2005) The conformation of the pore region of the M2 proton channel depends on lipid bilayer environment. *Protein Sci. 14*, 856–61.
(23) Saotome, K., Duong-Ly, K. C., and Howard, K. P. (2015) Influenza A M2 protein conformation depends on choice of model membrane. *Biopolymers 104*, 405–411.
(24) McMahon, H. T., and Gallop, J. L. (2005) Membrane curvature and mechanisms of dynamic cell membrane remodelling. *Nature 438*, 590–596.
(25) Cantor, R. S. (1999) Lipid Composition and the Lateral Pressure Profile in Bilayers. *Biophys. J. 76*, 2625–2639.
(26) Cleverley, D. Z., Geller, H. M., and Lenard, J. (1997) Characterization of Cholesterol-Free Insect Cells Infectible by Baculoviruses: Effects of Cholesterol on VSV Fusion and Infectivity and on Cytotoxicity Induced by Influenza M2 Protein. *Exp. Cell Res. 233*, 288–296.
(27) Thaa, B., Levental, I., Herrmann, A., and Veit, M. (2011) Intrinsic membrane association of the cytoplasmic tail of influenza virus M2 protein and lateral membrane sorting regulated by cholesterol binding and palmitoylation. *Biochem. J. 437*, 389–397.
(28) Thaa, B., Siche, S., Herrmann, A., and Veit, M. (2014) Acylation and cholesterol binding are not required for targeting of influenza A virus M2 protein to the hemagglutinin-defined budozone. *FEBS Lett. 588*, 1031–1036.
(29) Schroeder, C., Heider, H., Moncke-Buchner, E., and Lin, T. I. (2005) The influenza virus ion channel and maturation cofactor M2 is a cholesterol-binding protein. *Eur. Biophys. J. with Biophys. Lett. 34*, 52–66.
(30) Luo, W., Cady, S. D., and Hong, M. (2009) Immobilization of the influenza A M2 transmembrane peptide in virus envelope-mimetic lipid membranes: a solid-state NMR investigation. *Biochemistry 48*, 6361–8.
(31) Cristian, L., Lear, J. D., and DeGrado, W. F. (2003) Use of thiol-disulfide equilibria to measure the energetics of assembly of transmembrane helices in phospholipid bilayers. *Proc. Natl. Acad. Sci. U. S. A. 100*, 14772–7.
(32) Ekanayake, E. V., Fu, R., and Cross, T. A. (2016) Structural Influences: Cholesterol, Drug, and Proton Binding to Full-Length Influenza A M2 Protein. *Biophys. J. 110*, 1391–1399.
(33) Hu, F., Luo, W., Cady, S. D., and Hong, M. (2011) Conformational plasticity of the influenza A M2 transmembrane helix in lipid bilayers under varying pH, drug binding, and membrane thickness. *Biochim. Biophys. Acta - Biomembr. 1808*, 415–423.
(34) Liao, S. Y., Fritzsching, K. J., and Hong, M. (2013) Conformational analysis of the

full-length M2 protein of the influenza A virus using solid-state NMR. *Protein Sci. 22*, 1623–1638.
(35) McCown, M. F., and Pekosz, A. (2005) The influenza a Virus M-2 cytoplasmic tail is required for infectious virus production and efficient genome packaging. *J. Virol. 79*, 3595–3605.
(36) McCown, M. F., and Pekosz, A. (2006) Distinct domains of the influenza A virus M2 protein cytoplasmic tail mediate binding to the M1 protein and facilitate infectious virus production. *J. Virol. 80*, 8178–8189.
(37) Chen, B. J., Leser, G. P., Jackson, D., and Lamb, R. A. (2008) The Influenza Virus M2 Protein Cytoplasmic Tail Interacts with the M1 Protein and Influences Virus Assembly at the Site of Virus Budding. *J. Virol. 82*, 10059–10070.
(38) Grantham, M. L., Stewart, S. M., Lalime, E. N., and Pekosz, A. (2010) Tyrosines in the Influenza A Virus M2 Protein Cytoplasmic Tail Are Critical for Production of Infectious Virus Particles. *J. Virol. 84*, 8765–8776.
(39) Stewart, S. M., and Pekosz, A. (2011) Mutations in the Membrane-Proximal Region of the Influenza A Virus M2 Protein Cytoplasmic Tail Have Modest Effects on Virus Replication. *J. Virol. 85*, 12179–12187.
(40) Roberts, K. L., Leser, G. P., Ma, C., and Lamb, R. A. (2013) The amphipathic helix of influenza A virus M2 protein is required for filamentous bud formation and scission of filamentous and spherical particles. *J. Virol. 87*, 9973–82.
(41) Schmidt, N. W., Mishra, A., Wang, J., DeGrado, W. F., and Wong, G. C. L. (2013) Influenza Virus A M2 Protein Generates Negative Gaussian Membrane Curvature Necessary for Budding and Scission. *J. Am. Chem. Soc. 135*, 13710–13719.
(42) Martyna, A., Bahsoun, B., Badham, M. D., Srinivasan, S., Howard, M. J., and Rossman, J. S. (2017) Membrane remodeling by the M2 amphipathic helix drives influenza virus membrane scission. *Sci. Rep. 7*, 44695.
(43) Klug, C. S., and Feix, J. B. (2008) Methods and Applications of Site-Directed Spin Labeling EPR Spectroscopy, in *Biophysical Tools for Biologists: Volume 1 In Vitro Techniques*, pp 617–658. Elsevier Academic Press Inc, San Diego, CA.
(44) Altenbach, C., López, C. J., Hideg, K., and Hubbell, W. L. (2015) Exploring Structure, Dynamics, and Topology of Nitroxide Spin-Labeled Proteins Using Continuous-Wave Electron Paramagnetic Resonance Spectroscopy, in *Methods in Enzymology*, pp 59–100.
(45) Hubbell, W. L., Mchaourab, H. S., Altenbach, C., and Lietzow, M. A. (1996) Watching proteins move using site-directed spin labeling. *Structure 4*, 779–783.
(46) McHaourab, H. S., Steed, P. R., and Kazmier, K. (2011, November 9) Toward the fourth dimension of membrane protein structure: Insight into dynamics from spin-labeling EPR spectroscopy. *Structure*.
(47) Bridges, M. D., Hideg, K., and Hubbell, W. L. (2010) Resolving Conformational and Rotameric Exchange in Spin-Labeled Proteins Using Saturation Recovery EPR. *Appl. Magn. Reson. 37*, 363–390.
(48) Budil, D. E., Lee, S., Saxena, S., and Freed, J. H. (1996) Nonlinear-Least-Squares Analysis of Slow-Motion EPR Spectra in One and Two Dimensions Using a Modified Levenberg–Marquardt Algorithm. *J. Magn. Reson. Ser. A 120*, 155–189.
(49) Levitt, M. H. (2008) Spin dynamics: basics of nuclear magnetic resonance. John Wiley & Sons.

(50) Rieger, P. (2007) Introduction, in *Electron Spin Resonance: Analysis and Interpretation* 1st ed., pp 1–20. Royal Society of Chemistry, Cambridge.
(51) Isas, J. M., Langen, R., Haigler, H. T., and Hubbell, W. L. (2002) Structure and Dynamics of a Helical Hairpin and Loop Region in Annexin 12: A Site-Directed Spin Labeling Study. *Biochemistry 41*, 1464–1473.
(52) Columbus, L., and Hubbell, W. L. (2004) Mapping Backbone Dynamics in Solution with Site-Directed Spin Labeling: GCN4−58 bZip Free and Bound to DNA. *Biochemistry 43*, 7273–7287.
(53) López, C. J., Fleissner, M. R., Guo, Z., Kusnetzow, A. K., and Hubbell, W. L. (2009) Osmolyte perturbation reveals conformational equilibria in spin-labeled proteins. *Protein Sci. 18*, 1637–52.
(54) Arbuckle, D. S. (2017) EPR Characterization of Membrane-Dependent, Curvature-Inducing Conformational Equilibrium in Influenza A M2 Protein. Swarthmore College.
(55) Gross, A., and Hubbell, W. L. (2001) Identification of Protein Side Chains near the Membrane−Aqueous Interface: A Site-Directed Spin Labeling Study of KcsA. *Biochemistry 41*, 1123–1128.
(56) Leonov, H., Astrahan, P., Krugliak, M., and Arkin, I. T. (2011) How Do Aminoadamantanes Block the Influenza M2 Channel, and How Does Resistance Develop? *J. Am. Chem. Soc. 133*, 9903–9911.
(57) Rossman, J. S., and Lamb, R. A. (2013) Viral membrane scission. *Annu. Rev. Cell Dev. Biol. 29*, 551–69.
(58) Iwatsuki-Horimoto, K., Horimoto, T., Noda, T., Kiso, M., Maeda, J., Watanabe, S., Muramoto, Y., Fujii, K., and Kawaoka, Y. (2006) The cytoplasmic tail of the influenza A virus M2 protein plays a role in viral assembly. *J. Virol. 80*, 5233–5240.
(59) Rossman, J. S., Jing, X. H., Leser, G. P., Balannik, V., Pinto, L. H., and Lamb, R. A. (2010) Influenza Virus M2 Ion Channel Protein Is Necessary for Filamentous Virion Formation. *J. Virol. 84*, 5078–5088.
(60) Kerviel, A., Dash, S., Moncorgé, O., Panthu, B., Prchal, J., Décimo, D., Ohlmann, T., Lina, B., Favard, C., Decroly, E., Ottmann, M., Roingeard, P., and Muriaux, D. (2016) Involvement of an Arginine Triplet in M1 Matrix Protein Interaction with Membranes and in M1 Recruitment into Virus-Like Particles of the Influenza A(H1N1)pdm09 Virus. *PLoS One* (Pekosz, A., Ed.) *11*, e0165421.
(61) Zhou, H.-X., and Cross, T. A. (2013) Modeling the membrane environment has implications for membrane protein structure and function: Influenza A M2 protein. *Protein Sci. 22*, 381–394.
(62) Kwon, B., Tietze, D., White, P. B., Liao, S. Y., and Hong, M. (2015) Chemical ligation of the influenza M2 protein for solid-state NMR characterization of the cytoplasmic domain. *Protein Sci. 24*, 1087–1099.
(63) Leiding, T., Wang, J., Martinsson, J., DeGrado, W. F., and Arsköld, S. P. (2010) Proton and cation transport activity of the M2 proton channel from influenza A virus. *Proc. Natl. Acad. Sci. U. S. A. 107*, 15409–14.
(64) Buchan, D. W. A., Minneci, F., Nugent, T. C. O., Bryson, K., and Jones, D. T. (2013) Scalable web services for the PSIPRED Protein Analysis Workbench. *Nucleic Acids Res. 41*, W349–W357.
(65) Bussell, R., and Eliezer, D. (2001) Residual structure and dynamics in Parkinson's disease-associated mutants of alpha-synuclein. *J. Biol. Chem. 276*, 45996–6003.

(66) Barré, P., and Eliezer, D. (2013) Structural transitions in tau k18 on micelle binding suggest a hierarchy in the efficacy of individual microtubule-binding repeats in filament nucleation. *Protein Sci. 22*, 1037–48.
(67) Georgieva, E. R., Xiao, S., Borbat, P. P., Freed, J. H., and Eliezer, D. (2014) Tau Binds to Lipid Membrane Surfaces via Short Amphipathic Helices Located in Its Microtubule-Binding Repeats. *Biophys. J. 107*, 1441–1452.
(68) Ward, J. J., McGuffin, L. J., Bryson, K., Buxton, B. F., and Jones, D. T. (2004) The DISOPRED server for the prediction of protein disorder. *Bioinformatics 20*, 2138–2139.
(69) Jao, C. C., Hegde, B. G., Chen, J., Haworth, I. S., and Langen, R. (2008) Structure of membrane-bound alpha-synuclein from site-directed spin labeling and computational refinement. *Proc. Natl. Acad. Sci. U. S. A. 105*, 19666–71.
(70) Mchaourab, H. S., Lietzow, M. A., Hideg, K., and Hubbell, W. L. (1996) Motion of Spin-Labeled Side Chains in T4 Lysozyme. Correlation with Protein Structure and Dynamics†. *Biochemistry 35*, 7692–7704.
(71) Hubbell, W. L., Gross, A., Langen, R., and Lietzow, M. A. (1998) Recent advances in site-directed spin labeling of proteins. *Curr. Opin. Struct. Biol. 8*, 649–56.
(72) Richardson, J. S., and Richardson, D. C. (1988) Amino acid preferences for specific locations at the ends of alpha helices. *Science 240*, 1648–52.
(73) Bra□ndén, C.-I., and Tooze, J. (1999) Introduction to protein structure. Garland Pub.
(74) Darapaneni, V. (2015, January 20) Large-scale Analysis of Influenza A Virus Sequences Reveals Universally Conserved Residues of Matrix Proteins. *Am. J. Curr. Microbiol.*
(75) Desuzinges Mandon, E., Traversier, A., Champagne, A., Benier, L., Audebert, S., Balme, S., Dejean, E., Rosa Calatrava, M., and Jawhari, A. (2017) Expression and purification of native and functional influenza A virus matrix 2 proton selective ion channel. *Protein Expr. Purif. 131*, 42–50.
(76) Holsinger, L. J., Shaughnessy, M. A., Micko, A., Pinto, L. H., and Lamb, R. A. (1995) Analysis Of The Posttranslational Modifications Of The Influenza-Virus M2 Protein. *J. Virol. 69*, 1219–1225.
(77) Thomas, J. M., Stevens, M. P., Percy, N., and Barclay, W. S. (1998) Phosphorylation of the M2 Protein of Influenza A Virus Is Not Essential for Virus Viability. *Virology 252*, 54–64.
(78) Liao, S. Y., Yang, Y., Tietze, D., and Hong, M. (2015) The Influenza M2 Cytoplasmic Tail Changes the Proton-Exchange Equilibria and the Backbone Conformation of the Transmembrane Histidine Residue to Facilitate Proton Conduction. *J. Am. Chem. Soc. 137*, 6067–6077.
(79) Chong, S. S. Y., Taneva, S. G., Lee, J. M. C., and Cornell, R. B. (2014) The Curvature Sensitivity of a Membrane-Binding Amphipathic Helix Can Be Modulated by the Charge on a Flanking Region. *Biochemistry 53*, 450–461.
(80) Yang, S.-T., Kiessling, V., Simmons, J. A., White, J. M., and Tamm, L. K. (2015) HIV gp41–mediated membrane fusion occurs at edges of cholesterol-rich lipid domains. *Nat. Chem. Biol. 11*, 424–431.
(81) Leser, G. P., and Lamb, R. A. (2005) Influenza virus assembly and budding in raft-derived microdomains: A quantitative analysis of the surface distribution of HA, NA and M2 proteins. *Virology 342*, 215–227.
(82) Kim, S. S. (2014) Probing and Characterizing Different Conformations of the

Influenza A M2 Protein Using SDSL-EPR Spectroscopy. Swarthmore College.
(83) Subczynski, W. K., Raguz, M., and Widomska, J. (2010) Studying Lipid Organization in Biological Membranes Using Liposomes and EPR Spin Labeling, in *Methods in molecular biology (Clifton, N.J.)*, pp 247–269.
(84) Upshur, M. A. (2012) SDSL EPR Spectroscopy Reveals Cholesterol Dependent Conformational Shift of Influenza A Protein. Swarthmore College.
(85) Drin, G., and Antonny, B. (2010) Amphipathic helices and membrane curvature. *FEBS Lett. 584*, 1840–1847.
(86) Richardson, J. S., and Richardson, D. C. (1989) Principles and Patterns of Protein Conformation, in *Prediction of Protein Structure and the Principles of Protein Conformation*, pp 1–98. Springer US, Boston, MA.
(87) Martyna, A., Gómez-Llobregat, J., Lindén, M., and Rossman, J. S. (2016) Curvature Sensing by a Viral Scission Protein. *Biochemistry 55*, 3493–3496.
(88) Miles, A. J., and Wallace, B. A. (2016) Circular dichroism spectroscopy of membrane proteins. *Chem. Soc. Rev. 45*, 4859–4872.
(89) Veglia, G., Nelson, S. E. D., and Gopinath, T. (2016) Allosteric Regulation of the M2 Protein from Influenza A by Cholesterol. *Biophys. J. 110*, 1207–8.
(90) Zhao, W., Róg, T., Gurtovenko, A. A., Vattulainen, I., and Karttunen, M. (2007) Atomic-Scale Structure and Electrostatics of Anionic Palmitoyloleoylphosphatidylglycerol Lipid Bilayers with Na+ Counterions. *Biophys. J. 92*, 1114–1124.
(91) Nguyen, P. A. (2008) Conformational Changes in the M2 Protein of Influenza A Virus upon pH Activation and Drug Binding. Swarthmore College.
(92) Howard, K. P., Lear, J. D., and DeGrado, W. F. (2002) Sequence determinants of the energetics of folding of a transmembrane four-helix-bundle protein. *Proc. Natl. Acad. Sci. 99*, 8568–8572.
(93) Deupi, X., and Kobilka, B. K. (2010) Energy landscapes as a tool to integrate GPCR structure, dynamics, and function. *Physiology (Bethesda). 25*, 293–303.
(94) Wang, D., Harmon, A., Jin, J., Francis, D. H., Christopher-Hennings, J., Nelson, E., Montelaro, R. C., and Li, F. (2010) The lack of an inherent membrane targeting signal is responsible for the failure of the matrix (M1) protein of influenza A virus to bud into virus-like particles. *J. Virol. 84*, 4673–81.
(95) Chlanda, P., and Zimmerberg, J. (2016) Protein-lipid interactions critical to replication of the influenza A virus during infection. *FEBS Lett.*
(96) Martyna, A., and Rossman, J. (2014) Alterations of membrane curvature during influenza virus budding. *Biochem. Soc. Trans. 42*, 1425–1428.
(97) Drin, G., Casella, J.-F., Gautier, R., Boehmer, T., Schwartz, T. U., and Antonny, B. (2007) A general amphipathic α-helical motif for sensing membrane curvature. *Nat. Struct. Mol. Biol. 14*, 138–146.
(98) Vanni, S., Vamparys, L., Gautier, R., Drin, G., Etchebest, C., Fuchs, P. F. J., and Antonny, B. (2013) Amphipathic Lipid Packing Sensor Motifs: Probing Bilayer Defects with Hydrophobic Residues. *Biophys. J. 104*, 575–584.
(99) Yi, M., Cross, T. A., and Zhou, H.-X. (2009) Conformational heterogeneity of the M2 proton channel and a structural model for channel activation. *Proc. Natl. Acad. Sci. 106*, 13311–13316.
(100) Schnell, J. R., and Chou, J. J. (2008) Structure and mechanism of the M2 proton

channel of influenza A virus. *Nature 451*, 591–U12.
(101) Wang, T., and Hong, M. (2015) Investigation of the Curvature Induction and Membrane Localization of the Influenza Virus M2 Protein Using Static and Off-Magic-Angle Spinning Solid-State Nuclear Magnetic Resonance of Oriented Bicelles. *Biochemistry 54*, 2214–2226.
(102) Ambroso, M. R., Hegde, B. G., and Langen, R. (2014) Endophilin A1 induces different membrane shapes using a conformational switch that is regulated by phosphorylation. *Proc. Natl. Acad. Sci. 111*, 6982–6987.
(103) Jao, C. C., Hegde, B. G., Gallop, J. L., Hegde, P. B., McMahon, H. T., Haworth, I. S., and Langen, R. (2010) Roles of Amphipathic Helices and the Bin/Amphiphysin/Rvs (BAR) Domain of Endophilin in Membrane Curvature Generation. *J. Biol. Chem. 285*, 20164–20170.
(104) Ho, C. S., Khadka, N. K., She, F., Cai, J., and Pan, J. (2016) Influenza M2 Transmembrane Domain Senses Membrane Heterogeneity and Enhances Membrane Curvature. *Langmuir 32*, 6730–6738.
(105) Kusnetzow, A. K., Altenbach, C., and Hubbell, W. L. (2006) Conformational States and Dynamics of Rhodopsin in Micelles and Bilayers. *Biochemistry 45*, 5538–5550.
(106) Yang, S.-T., Kreutzberger, A. J. B., Lee, J., Kiessling, V., and Tamm, L. K. (2016) The role of cholesterol in membrane fusion. *Chem. Phys. Lipids*.
(107) Epand, R. F., Thomas, A., Brasseur, R., Vishwanathan, S. A., Hunter, E., and Epand, R. M. (2006) Juxtamembrane Protein Segments that Contribute to Recruitment of Cholesterol into Domains. *Biochemistry 45*, 6105–6114.
(108) Iversen, L., Mathiasen, S., Larsen, J. B., and Stamou, D. (2015) Membrane curvature bends the laws of physics and chemistry. *Nat. Chem. Biol. 11*, 822–825.
(109) Liang, B., Dawidowski, D., Ellena, J. F., Tamm, L. K., and Cafiso, D. S. (2014) The SNARE Motif of Synaptobrevin Exhibits an Aqueous–Interfacial Partitioning That Is Modulated by Membrane Curvature. *Biochemistry 53*, 1485–1494.
(110) Tobler, K., Kelly, M. L., Pinto, L. H., and Lamb, R. A. (1999) Effect of cytoplasmic tail truncations on the activity of the M-2 ion channel of influenza A virus. *J. Virol. 73*, 9695–9701.
(111) Chui, A. J., López, C. J., Brooks, E. K., Chua, K. C., Doupey, T. G., Foltz, G. N., Kamel, J. G., Larrosa, E., Sadiki, A., and Bridges, M. D. (2015) Multiple Structural States Exist Throughout the Helical Nucleation Sequence of the Intrinsically Disordered Protein Stathmin, As Reported by Electron Paramagnetic Resonance Spectroscopy. *Biochemistry 54*, 1717–1728.
(112) Bavi, N., Cortes, D. M., Cox, C. D., Rohde, P. R., Liu, W., Deitmer, J. W., Bavi, O., Strop, P., Hill, A. P., Rees, D., Corry, B., Perozo, E., and Martinac, B. (2016) The role of MscL amphipathic N terminus indicates a blueprint for bilayer-mediated gating of mechanosensitive channels. *Nat. Commun. 7*, 11984.
(113) Fernández-Vidal, M., Jayasinghe, S., Ladokhin, A. S., and White, S. H. (2007) Folding amphipathic helices into membranes: amphiphilicity trumps hydrophobicity. *J. Mol. Biol. 370*, 459–70.
(114) Granseth, E., von Heijne, G., and Elofsson, A. (2005) A Study of the Membrane–Water Interface Region of Membrane Proteins. *J. Mol. Biol. 346*, 377–385.
(115) Gautier, R., Douguet, D., Antonny, B., and Drin, G. (2008) HELIQUEST: a web server to screen sequences with specific -helical properties. *Bioinformatics 24*, 2101–

2102.
(116) Rufener, E., Frazier, A. A., Wieser, C. M., Hinderliter, A., and Cafiso, D. S. (2005) Membrane-Bound Orientation and Position of the Synaptotagmin C2B Domain Determined by Site-Directed Spin Labeling †. *Biochemistry 44*, 18–28.
(117) Sreerama, N., and Woody, R. W. (2000) Estimation of Protein Secondary Structure from Circular Dichroism Spectra: Comparison of CONTIN, SELCON, and CDSSTR Methods with an Expanded Reference Set. *Anal. Biochem. 287*, 252–260.
(118) Whitmore, L., and Wallace, B. A. (2004) DICHROWEB, an online server for protein secondary structure analyses from circular dichroism spectroscopic data. *Nucleic Acids Res. 32*, W668–73.
(119) Waugh, D. S. (2011, December) An overview of enzymatic reagents for the removal of affinity tags. *Protein Expr. Purif.*
(120) Tropea, J. E., Cherry, S., and Waugh, D. S. (2009) Expression and purification of soluble His(6)-tagged TEV protease. *Methods Mol. Biol. 498*, 297–307.
(121) Lundbäck, A.-K., van den Berg, S., Hebert, H., Berglund, H., and Eshaghi, S. (2008) Exploring the activity of tobacco etch virus protease in detergent solutions. *Anal. Biochem.*
(122) Taylor, J. R. (1997) An Introduction to Error Analysis. *J. Acoust. Soc. Am. 101*, 330.
(123) Gasteiger, E., Hoogland, C., Gattiker, A., Duvaud, S., Wilkins, M. R., Appel, R. D., and Bairoch, A. (2005) Protein Identification and Analysis Tools on the ExPASy Server. *Proteomics Protoc. Handb.* 571–607.